

AMERICAN UNIVERSITY OF BEIRUT

Tuning Surface Phonon Polaritons

by
Hrag Karakachian

A thesis
submitted in partial fulfillment of the requirements
for the degree of Master of Science
to the Department of Physics
of the Faculty of Arts and Sciences
at the American University of Beirut

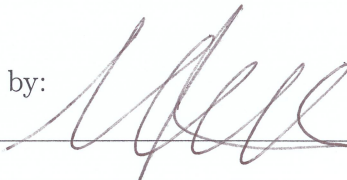
Beirut, Lebanon
June 2017

AMERICAN UNIVERSITY OF BEIRUT

Tuning Surface Phonon Polaritons

by
Hrag Karakachian

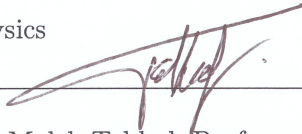
Approved by:



Dr. Michel Kazan, Associate Professor

Advisor

Physics



Dr. Malek Tabbal, Professor

Member of Committee

Physics



Dr. Jihad Touma, Professor

Member of Committee

Physics

Date of thesis defense: June 15, 2017

AMERICAN UNIVERSITY OF BEIRUT

THESIS, DISSERTATION, PROJECT RELEASE FORM

Student Name: Karakachian Hrag Rafi
Last First Middle

Master's Thesis Master's Project Doctoral Dissertation

I authorize the American University of Beirut to: (a) reproduce hard or electronic copies of my thesis, dissertation, or project; (b) include such copies in the archives and digital repositories of the University; and (c) make freely available such copies to third parties for research or educational purposes.

I authorize the American University of Beirut, to: (a) reproduce hard or electronic copies of it; (b) include such copies in the archives and digital repositories of the University; and (c) make freely available such copies to third parties for research or educational purposes after: **One ___ year from the date of submission of my thesis, dissertation or project.**
Two ___ years from the date of submission of my thesis, dissertation or project.
Three ___ years from the date of submission of my thesis, dissertation or project.

Hrag Rafi
Signature

31/08/2017
Date

This form is signed when submitting the thesis, dissertation, or project to the University Libraries

Acknowledgements

“I have no special talent, I am only passionately curious”. A quote by Albert Einstein that I can genuinely relate to. Six years ago I started my scientific journey as a sophomore physics student at the American University of Beirut (AUB). It was a difficult journey at first, but a fun experience overall. I embarked on my academic life with no set of special skills nor with a unique talent. It was my passion for knowing the unknown that kept me going through all those years and drove me to have my own contribution in the field of nanotechnology. My days at AUB will soon come to an end, and it is my duty to show gratitude to every person who helped me on this path.

First and foremost I would like to thank my advisor Dr. Michel Kazan. From day one, you believed in me more than I believed in myself. During my master studies you taught me how to conduct an independent scientific research. You taught me how to work patiently on scientific problems even when the results seemed to be out of reach. I don't know how you do it, but you always find the time to answer my questions; even late at night on whatsapp. That is the reason why you brought out the best in me and we achieved what I didn't think could be achieved. In one year we were able to send two papers for publication. Dear Dr. Kazan, you laid the foundations of my future.

I would like to thank professors Malek Tabbal and Jihad Touma for accepting to be part of my thesis committee. I look forward to the comments and questions you will raise regarding my work. I believe the discussions we are going to have will improve my understanding of the topic.

A special thanks goes to my high school physics teacher Raffi Tchakerian. You were the reason I decided to study physics at AUB. You were so humorous and passionate about the subject that you made me fall in love with it. I still remember you saying in class “you have to feel the physics”. As it turns out, that is what I will be doing for the most part of my life.

I would like to thank my dear friend Antranik Sefilian for being a great classmate. We always pushed our limits to the extreme to reach academic excellence. I wish you all the best my friend.

I want to thank all my friends and band members for making this journey fun and pleasurable. Being around you was my comfort zone during stressful times.

And last but not least, a big thanks goes to all my family members. Thank you for the unlimited support you gave me during my whole life. You shaped my character and made me the person I am today. Thank you for giving me the freedom in deciding and planning my own future. After all, as Lebanese parents, letting their son to study physics is a pretty courageous move.

Thank you!

Abstract

Hrag Karakachian for Master of Science
Major: Physics

Title: Tuning Surface Phonon Polaritons

The growing need for the development of nanophotonic devices has led to challenges in describing and manipulating energy transport in sub-diffraction length scales. Low-loss Surface Phonon Polariton (SPhP) modes supported at the surface of polar materials are promising candidates for realizing this task. These surface waves are evanescent electromagnetic waves localized at the surface of dielectric crystals. They result from the coupling between photons and optical phonons. In the present thesis, we provide a thorough explanation of SPhP modes, and then introduce various methods for tuning the different properties of such a near-field radiation. The effect of free carrier concentration on the temporal coherence of surface polaritons is investigated, showing a practical method for enhancing the temporal coherence of infrared light-emitting nano-sources. Changing the surface symmetry of a dielectric crystal is shown to be a pragmatic technique for tuning the region of existence of SPhP modes. Finally, it is observed that the shape of the nanosized crystal plays a major role in determining the dispersion relation of these surface modes. The results highlighted in the present thesis are obtained from a rigorous analysis of reflectivity measurements using the conventional Kramers–Kronig conversion technique corrected on the basis of Fresnel equations for reflectivity.

Contents

Acknowledgements	v
Abstract	vii
1 Surface Phonon Polariton: Principles And Applications	1
1.1 What Are Surface Phonon Polaritons	1
1.1.1 Constituents of SPhP Modes	1
1.1.2 Surface Phonon Polariton	9
1.1.3 Region of Existence of SPhP Modes	11
1.2 Application of Surface Phonon Polaritons	13
1.2.1 Monochromatic and Coherent Light- Emitting Thermal Sources	17
1.2.2 Cancer Treatment	20
1.3 Experimental Detection of SPhP Waves	24
1.3.1 Attenuated Total Reflection (ATR)	24
1.3.2 Scanning Near Field Optical Microscopy (SNOM)	26
2 Measurement Technique and Analysis	30
2.1 Fourier Transform Infrared Spectroscopy	31
2.1.1 Michelson Interferometer	31
2.1.2 Reflectivity Spectrum	32
2.2 Kramers- Kronig Conversion Technique	34
2.2.1 Relationship between the complex dielectric function and reflectivity	34
2.2.2 Kramers- Kronig Relations	35
2.2.3 Application of the Kramers- Kronig Relations to the Re- fectivity	36
3 Dependence of Surface Plasmon-Phonon-Polariton in 4H-SiC on Free Carrier Concentration	38
3.1 Experiments	41
3.2 Analysis of Reflectivity Spectra and Dielectric Spectra by a Cor- rected Kramers- Kronig Conversion Technique	43

3.2.1	Method for Correcting the Kramers–Kronig Conversion	44
3.2.2	Complex refractive indices of the samples investigated obtained from the corrected Kramers-Kronig technique.	50
3.3	Results and Discussion	52
3.3.1	The effect of plasmon electronic oscillation on the zone center optical phonons	52
3.3.2	Bulk Plasmon–Phonon–Polariton	55
3.3.3	Surface Plasmon–Phonon–Polariton	58
3.3.4	Comparison between bulk and surface plasmon-phonon-polariton modes	60
3.3.5	Temporal coherence of the surface plasmon-phonon polariton modes	62
3.4	Conclusion	63
4	AlN–Based Tunable Near–Field Infrared Sources	65
4.1	Experiments	68
4.2	Results and Discussion	69
4.2.1	A General Model for Infrared Reflectivity	70
4.2.2	Determination of the Harmonicity Parameters in the Expressions of the Dielectric Functions	74
4.2.3	Determination of the Anharmonicity Parameters in the Expressions of the Dielectric Functions	76
4.2.4	Determination of the dielectric functions for ' <i>p</i> ' and ' <i>s</i> ' polarizations by fitting the model for reflectivity to the measured reflectivity spectra	79
4.2.5	Dependence of SPhP on Surface Orientation	83
4.3	Conclusion	87
5	Surface Phonon Polaritons on cylindrical structures	88
6	Conclusion	94
A	Fresnel Equations for Reflectivity	98

List of Figures

1.1	Monatomic linear chain connected by springs of force constant α . Neighboring atoms are separated by a distance ‘a’.	2
1.2	Dispersion relation of a monatomic linear chain considering only nearest neighbor interactions.	3
1.3	Diatomic linear chain with two different masses M_1 and M_2 in a single unit cell, connected by springs of alternating strengths α and β . The unit cells are separated by a distance ‘a’. The interatomic distance in a single unit cell is ‘d’. The equilibrium positions of the atoms are ‘na’ and ‘na + d’.	4
1.4	Dispersion relation of the diatomic linear chain. The lower branch is the same acoustic branch observed in a monatomic linear chain. The upper branch is the optical branch.	5
1.5	Surface diagram: region 1 represents the dielectric, region 2 represents the air	9
1.6	Two semi- infinite planes at two different temperatures T_1 and T_2 separated by a distance z.	14
1.7	Planck’s blackbody radiation presented at different temperatures.	15
1.8	Energy density of SiO_2 calculated at 3 different heights at a temperature of 300 K. The energy density increases due to contributions from the near field radiation. [1]	16
1.9	Grating introduced on the surface a polar material having a periodicity 2d and height h.	18
1.10	Dispersion relation of SPhP in AlN crystal (blue curve). Cone of light (red curve).	19
1.11	Dispersion relation of SPhP on a grating. Blue curve represents the folded dispersion relation due to the interaction of SPhP waves with the periodicity of the grating. The period of the grating is 23 μm . The red curve represents the cone of light. The portion of the dispersion relation that lies in the cone of light can be radiated in the far- field.	19
1.12	Fixing nanoparticles on cancerous cells with the help of specific antibodies.	22

1.13	A diagram showing the ATR setup. Region 3 is the prism, region 2 is air and region 1 is the polar material where SPhP waves are excited.	25
1.14	A dip in the reflected intensity is observed due to coupling of surface waves at the prism with SPhP modes. Reflectivity curves of arbitrary units are shown for two different dielectric materials. Each sample shows a dip in reflectivity at different incident angles. This means that SPhP modes of different energies are excited at the surface of the two different dielectric materials.	26
1.15	The concept of SNOM: Diffraction of near field radiation into the far field, making use of a dipole excitation.	27
1.16	Experimental setup of SNOM: the tip diffracts the near field and reflects the incident field. The interference of the two waves is used to measure the SPhP. The near field is excited by the diffraction of the incident radiation at the border of the metallic thin film.	28
2.1	Michelson interferometer having a monochromatic source S, a translating mirror M_1 , a fixed mirror M_2 , a beam splitter and a detector.	32
3.1	Experimental configuration for recording reflectivity spectra averaged over a wide range of incidence angles.	43
3.2	Reflectivity spectra and real and imaginary parts of the complex refractive indices of the samples investigated. Solid lines: Real and imaginary parts of the refractive indices obtained by using the Kramers-Kronig technique corrected with reference to Fresnel equations for reflectivity. Dashed lines: Real and imaginary parts of the refractive index of the lowest doped sample obtained by using the conventional Kramers-Kronig conversion technique. The reflectivity spectra are back calculated using the real and imaginary parts of the refractive indices obtained from the corrected Kramers-Kronig technique. The measured reflectivity spectra are plotted with symbols. The back calculated reflectivity spectra are plotted with solid lines.	51
3.3	The dielectric properties of the samples investigated obtained from the corrected the Kramers-Kronig technique.	53
3.4	Dispersion relations, lifetime, and mean-propagation length of the bulk plasmon-phonon-polariton in the samples investigated.	56
3.5	Dispersion relations, lifetime, and mean-propagation length of the surface plasmon-phonon-polariton in the samples investigated. Inset: zoom in the region of existence of the surface plasmon-phonon-polariton.	59

3.6	Comparison between the surface plasmon-phonon-polariton (blue line) and bulk plasmon-phonon-polariton (red line) in the lowest doped 4H-SiC epilayer. The light lines in air (black) and in 4H-SiC (green) are also plotted.	61
4.1	Reflectivity spectra from the measured facets. Symbols: Experimental measurements. Solid lines: Model.	69
4.2	The real and imaginary parts of the normal incidence dielectric functions of the measured facets for a p-polarized light.	82
4.3	The dispersions of the SPhP waves on the measured facets.	84
4.4	The lifetimes of the SPhP modes on the measured facets	85
4.5	On the left: The spectral regions of existence of the SPhP modes on the measured facets. On the right: the lifetimes of the SPhP modes in their spectral regions of existence.	86
5.1	Geometry of the cylindrical structure.	89
5.2	Comparing the dispersion relation of SPhP modes supported by SiC samples of different shapes. Blue color is used to represent the nanowire and red curve is used to represent the flat surface	92
A.1	Reflection and transmission occur when light moves from a medium of a given refractive index to another.	99
A.2	The transfer matrix method: All reflected and transmitted waves in each medium are presented by a single wave. The amplitudes of the electric and magnetic fields at different points are related by an interference matrix M	100

List of Tables

4.1	Calculated phonon group velocities and Grüneisen parameters in ΓK and ΓM directions.	79
4.2	Model parameters. Only α and φ were used as independent adjustable parameters to fit the reflectivity model to the measured reflectivity spectra.	81

Chapter 1

Surface Phonon Polariton: Principles And Applications

1.1 What Are Surface Phonon Polaritons

Surface Phonon Polariton (SPhP) is a result of the coupling between electromagnetic modes (photons) and lattice vibrational modes (optical phonons) at the surface of polar materials. The nature of this pseudo-particle can be better understood if we spend some time investigating its core constituents: the photon and the optical phonon. The light-matter interaction being discussed also exists in the bulk of the material, therefore a clear distinction between bulk and surface phonon polaritons will be made.

1.1.1 Constituents of SPhP Modes

a. Phonons

In lattice dynamics problems, crystalline solids are defined as periodic arrays in which the repeated units of the crystal are symmetrically arranged, known as unit cells. The units themselves can be single atoms, groups of atoms, ions, molecules, etc. The periodicity of the crystal provides the lattice with a transla-

tional symmetry, highlighting the fact that the equations of motion of all units are identical. This essentially reduces the problem of the dynamics of all the atoms in the crystal, to the dynamics of the atoms in a single unit cell, where the equations of motion are solved within the harmonic approximation.

The harmonic approximation takes into account two-body interactions where the interacting entities are weakly displaced. Most often, nearest neighbor interactions are considered within the atoms, which can be visualized as atoms joined by harmonic springs vibrating about their equilibrium point. In this assumption the lattice dynamics can be analyzed in terms of linear combinations of $3N$ (N being the number of atoms) normal modes of vibration. A normal mode of vibration can be described as a travelling wave having the form $Ae^{i\mathbf{q}\cdot\mathbf{r}-\omega t}$ where \mathbf{q} is the wavevector specifying the direction of propagation, ω is the angular frequency of the travelling wave and A is the amplitude of the vibration. The quantum mechanical treatment of the harmonic oscillators allows us to write the energies of the modes in the form $(n + 1/2)\hbar\omega(q)$ with $n = 0, 1, 2, \dots$. Hence, the quantum of energy $\hbar\omega(q)$ represents an elementary excitation of crystal vibration known as phonon. [2]

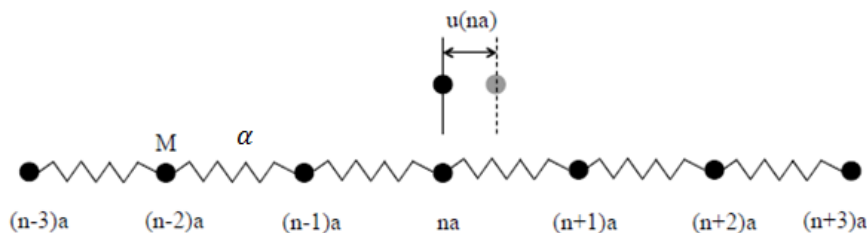


Figure 1.1: Monatomic linear chain connected by springs of force constant α . Neighboring atoms are separated by a distance 'a'.

The simplest method for solving the dynamical problem is to consider a

monatomic linear chain (Figure 1.1) of an infinitely large number, N , of atoms separated by a distance a . Considering nearest neighbor interaction and applying periodic boundary conditions, the equation of motion of each atom will be

$$M\ddot{u} = -\alpha[2u(na) - u([n+1]a) - u([n-1]a)], \quad (1.1)$$

where α is the spring constant between two ions and u is the displacement of each ion about its equilibrium position. We seek a solution to the equation of motion having the form of a travelling wave $u(na, t) \propto e^{qna - \omega t}$. Substituting the solution back into the equation of motion, the dispersion relation $\omega(q)$ can be found

$$\omega(q) = 2\sqrt{\frac{\alpha}{M}} \left| \sin \frac{qa}{2} \right|. \quad (1.2)$$

As can be seen, in the case of monatomic linear chain (Figure 1.2), the phonon

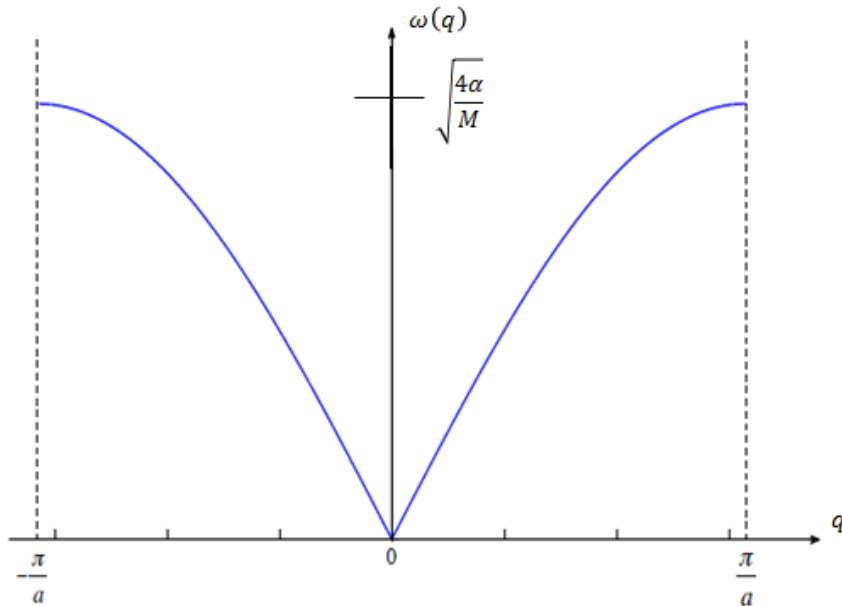


Figure 1.2: Dispersion relation of a monatomic linear chain considering only nearest neighbor interactions.

dispersion curves show only one branch defined as the acoustic phonon branch. Acoustic phonons are the sound carriers inside a material, hence the word "acoustic". They play a major role in determining the thermal conductivity of the material, however they are unable to interact with an incident electromagnetic field.

A light-matter interaction is observed when a polyatomic crystal is exposed to radiation. To evaluate the phonon dispersion relation of such crystals, we consider a diatomic linear chain with two different ions (having masses M_1 and M_2) inside a unit cell (Figure 1.3). Let a be the distance between two unit cells

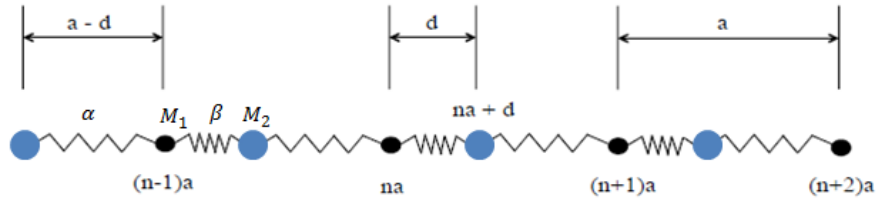


Figure 1.3: Diatomic linear chain with two different masses M_1 and M_2 in a single unit cell, connected by springs of alternating strengths α and β . The unit cells are separated by a distance 'a'. The interatomic distance in a single unit cell is 'd'. The equilibrium positions of the atoms are 'na' and 'na + d'.

and d the distance between ions of the same unit cell. We also define α as the spring constant between ions in different unit cells, and β the force constant between ions of the same unit cell. Therefore the equations of motion in this approximation will be given by

$$M_1 \ddot{u}_1(na) = -\alpha [u_1(na) - u_2(na)] - \beta [u_1(na) - u_2((n-1)a)], \quad (1.3)$$

and

$$M_2 \ddot{u}_2(na) = -\alpha [u_2(na) - u_1(na)] - \beta [u_2(na) - u_1((n+1)a)]. \quad (1.4)$$

Seeking solutions of the form $u_1(na) = A_1 e^{i(qna - \omega t)}$ and $u_2(na) = A_2 e^{i(qna - \omega t)}$ we find the dispersion relations of the diatomic chain model to be

$$\omega^2 = \frac{\alpha + \beta}{2\mu} \pm \frac{1}{2} \left[\frac{(\alpha + \beta)^2}{\mu^2} - \frac{8\alpha\beta}{M_1 M_2} (1 - \cos qa) \right]^{1/2}, \quad (1.5)$$

where $\mu = \frac{M_1 M_2}{M_1 + M_2}$ is defined as the reduced mass. Unlike the monatomic case, the dispersion relations of the diatomic chain display two phonon branches (Figure

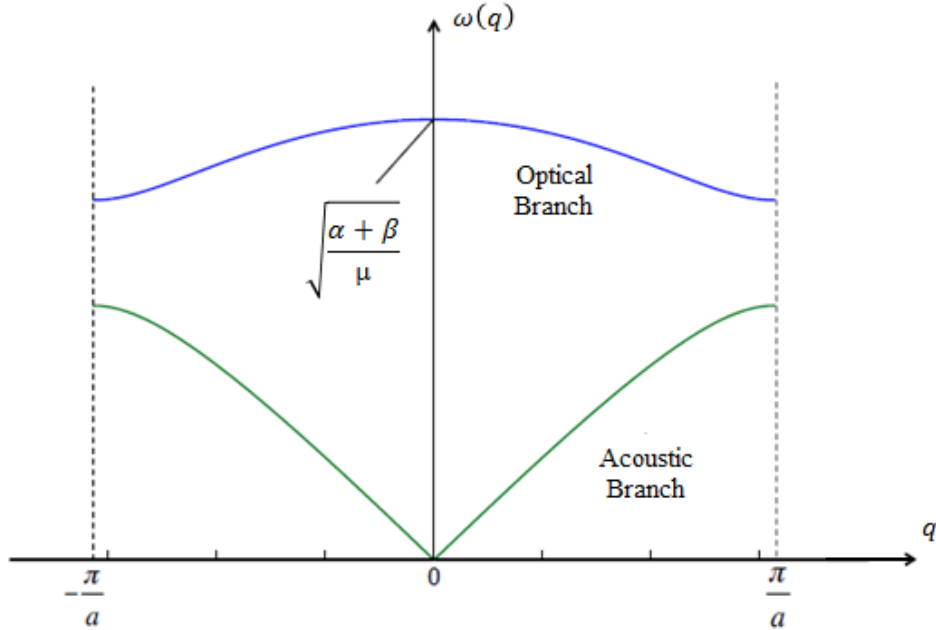


Figure 1.4: Dispersion relation of the diatomic linear chain. The lower branch is the same acoustic branch observed in a monatomic linear chain. The upper branch is the optical branch.

1.4): the optical phonon branch is obtained when ions are vibrating out of phase (determined by the plus sign in equation 1.5) and the acoustic phonon branch

is obtained when ions are vibrating in phase (determined by the minus sign in equation 1.5). The optical branch, as the name suggest, describes the phonons that interact with incident electric fields and determine the optical properties of the material. They stand as the core constituents of the SPhP modes.

b. Photons

Let us now investigate the behavior of the second constituent of SPhP modes (i.e. photons) inside a polar material. Our development here will show how the electromagnetic behavior can be related to the dielectric function $\epsilon(\omega)$ which describes the response of optical phonons to an incident electromagnetic field. We start by solving Maxwells equations in a dielectric medium (in SI units) [3]

$$\nabla \times \mathbf{H} = \mathbf{j} + \frac{\partial \mathbf{D}}{\partial t} \quad (1.6)$$

$$\nabla \times \mathbf{E} = -\frac{\partial \mathbf{B}}{\partial t} \quad (1.7)$$

$$\nabla \cdot \mathbf{D} = \rho \quad (1.8)$$

$$\nabla \cdot \mathbf{B} = 0 \quad (1.9)$$

where \mathbf{H} is the magnetic field strength, \mathbf{j} is the current density, \mathbf{D} is the displacement vector, \mathbf{E} is the electric field, and ρ is the free carrier charge density. Unlike free space, a solid contains both free and bound charges. The bound charges produce a dipole moment per unit volume, giving rise to a polarization \mathbf{P} . The polarization vector can be related to the electric field in the following way $\mathbf{P} = \chi\epsilon_0\mathbf{E}$, where $\chi(\omega)$ is called the susceptibility indicating the degree of polarizability of a dielectric material in response to an applied electric field. Having the polarization as a function of the electric field we can express the displacement

vector in terms of the electric field only

$$\mathbf{D} = \epsilon_0 \mathbf{E} + \mathbf{P} = \epsilon_0(1 + \chi) \mathbf{E} = \epsilon_{lat}(\omega) \epsilon_0 \mathbf{E} \quad (1.10)$$

where $\epsilon_{lat}(\omega)$ is the dielectric function describing the polarization.

On the other hand, the mobile free charges determine the electrical conductivity of the sample. They give rise to a current density \mathbf{j} inside the material which can be related to the electric field using Ohms law

$$\mathbf{j} = \sigma(\omega) \mathbf{E} \quad (1.11)$$

where $\sigma(\omega)$ is the frequency dependent electrical conductivity. Substituting equations (1.10) and (1.11) in Maxwells equations and taking the curl of equation (1.7) we find

$$\nabla \times \nabla \times \mathbf{E} = \nabla^2 \mathbf{E} - \nabla(\nabla \cdot \mathbf{E}) = \epsilon_{lat}(\omega) \epsilon_0 \mu_0 \frac{\partial^2 \mathbf{E}}{\partial t^2} + \sigma(\omega) \mu_0 \frac{\partial \mathbf{E}}{\partial t} \quad (1.12)$$

where μ_0 is the magnetic permeability of the material. Assuming a plane wave solution propagating in the z -direction $\mathbf{E} = \mathbf{E}_0 e^{i(qz - \omega t)}$ and substituting it back in equation (1.12) we find

$$q^2 \mathbf{E} - \mathbf{q}(\mathbf{q} \cdot \mathbf{E}) = \omega^2 \epsilon(\omega) \epsilon_0 \mu_0 \mathbf{E} \quad (1.13)$$

with $\epsilon(\omega)$ being the total dielectric function defined as $\epsilon(\omega) = \epsilon_{lat}(\omega) + \frac{i\sigma(\omega)}{\epsilon_0 \omega}$. Unlike free space where the electric field is always transverse, the presence of the charge density in equation (1.8) forces the electric field to acquire a longitudinal character in addition to its transverse component. Therefore the electric field can

be written as a sum of transverse and longitudinal components,

$$\mathbf{E} = E_t \hat{t} + E_q \hat{q}. \quad (1.14)$$

Finally, the dispersion relation of photons inside a dielectric material can be found by substituting equation (1.14) in equation (1.13) and defining the constant speed of light c as the inverse of $\epsilon_0 \mu_0$,

$$\left[\left(\frac{\omega}{c} \right)^2 \epsilon(\omega) - q^2 \right] E_t \hat{t} + \left(\frac{\omega}{c} \right)^2 \epsilon(\omega) E_q \hat{q} = 0. \quad (1.15)$$

Equation (1.15) is satisfied only if the coefficients of both the transverse and longitudinal components are zero.

$$q^2 = \left(\frac{\omega}{c} \right)^2 \epsilon(\omega) \quad (1.16)$$

is the dispersion relation of transverse waves in a solid of total dielectric function $\epsilon(\omega)$ and

$$\epsilon(\omega) = 0 \quad (1.17)$$

is the condition for longitudinal modes to exist. As we can see in equations (1.16) and (1.17) the behavior of electromagnetic waves is influenced by the response function $\epsilon(\omega)$. In the terahertz (THz) regime, the response function will be described by the interaction of zone center optical phonons with the incident infrared (IR) radiation. This means that in the IR region of the spectrum, the presence of $\epsilon(\omega)$ in the dispersion relation will highlight the coupling of photon-phonon modes. Hence the presence of IR electromagnetic waves inside a material will be affected by the vibrational modes giving rise to a single wave whose

quantum of energy is called *phonon-polariton*.

1.1.2 Surface Phonon Polariton

As described earlier, polaritons are electromagnetic modes; hence their dispersion relation at the surface of a material can be calculated by solving Maxwell's equations and applying the necessary boundary conditions at the interface between two different media. These surface electromagnetic waves are TM (transverse magnetic) waves having transverse and longitudinal electric fields and a transverse magnetic field. The equations describing such waves are thoroughly explained in Ref. [4]. Assuming an interface between two different dielectric media with ϵ_1 and ϵ_2 , we can write the expressions of the electromagnetic waves in the following way,

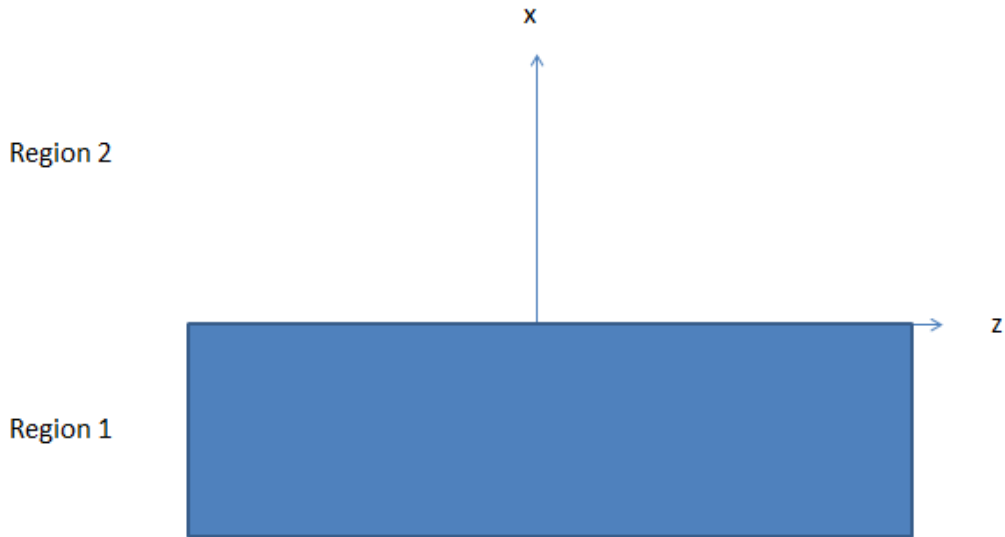


Figure 1.5: Surface diagram: region 1 represents the dielectric, region 2 represents the air

Region 1:

$$E_z^1 = A_1 e^{p_1 x} \quad (1.18)$$

$$E_x^1 = \frac{i q}{p_1} A_1 e^{p_1 x} \quad (1.19)$$

$$H_y^1 = \frac{i \omega \epsilon_1}{p_1} A_1 e^{p_1 x} \quad (1.20)$$

where A_1 is an arbitrary constant that determines the amplitude of these waves, $p_1^2 = q^2 - k_1^2$ with $k_1^2 = \omega^2 \mu_0 \epsilon_1$.

Region 2:

$$E_z^2 = A_2 e^{p_2 x} \quad (1.21)$$

$$E_x^2 = -\frac{i q}{p_2} A_2 e^{p_2 x} \quad (1.22)$$

$$H_y^2 = -\frac{i \omega \epsilon_2}{p_2} A_2 e^{p_2 x} \quad (1.23)$$

with A_2 an arbitrary constant that determines the amplitude of the waves, $p_2^2 = q^2 - k_2^2$ and $k_2^2 = \omega^2 \mu_0 \epsilon_2$. Matching the tangential fields at the surface ($x = 0$) yields,

$$A_1 = A_2 \quad (1.24)$$

and

$$\frac{i \omega \epsilon_1}{p_1} A_1 = -\frac{i \omega \epsilon_2}{p_2} A_2 \quad (1.25)$$

Replacing p_1 and p_2 by their appropriate expressions in equation (1.25) the dispersion relation of the surface waves can be found

$$(c q)^2 = \frac{\epsilon_1 \epsilon_2}{\epsilon_1 + \epsilon_2} \omega^2. \quad (1.26)$$

Usually one of the media in equation (1.26) is assumed to be non-dispersive with a constant dielectric function ϵ_2 . Similarly to bulk polaritons, the properties of the surface modes are mainly dependent on the response function ϵ_1 determined by the zone center optical phonons. Therefore the dispersion relation (1.26) describes the coupling between photons and zone center optical phonons at the surface of a polar material. In other words, it describes the behavior of surface phonon polariton (SPhP) modes.

1.1.3 Region of Existence of SPhP Modes

As mentioned earlier, the dielectric function is described by the response of zone center optical phonons to an incident radiation in the IR regime. At finite temperatures, all phonon modes are subject to decay and can be visualized as damped harmonic oscillators. Due to optical phonon decay, the dielectric function becomes a complex function. To find the region of existence of the SPhP modes, we go back and express the parameters p_1 and p_2 in terms of complex dielectric functions

$$p_1 = \frac{\omega}{c} \sqrt{\frac{-\epsilon_1^2}{\epsilon_0(\epsilon_1 + \epsilon_2)}} \quad (1.27)$$

and

$$p_2 = \frac{\omega}{c} \sqrt{\frac{-\epsilon_2^2}{\epsilon_0(\epsilon_1 + \epsilon_2)}} \quad (1.28)$$

We consider having a polar material with complex dielectric function ϵ_1 in contact with a medium having a real and positive response function ϵ_2 such as air. Writing the dielectric function in a complex form

$$\frac{\epsilon_1}{\epsilon_0} = \epsilon_{r1} - i\epsilon_{i1} \quad (1.29)$$

we can express the dispersion relation (equation 1.26) in terms of the real ϵ_{r1} and imaginary ϵ_{i1} parts of the complex dielectric function [4]

$$q = \frac{\omega}{c} \left[\frac{(\epsilon_{r1} - i\epsilon_{i1})\epsilon_2}{(\epsilon_2 + \epsilon_{r1}) - i\epsilon_{i1}} \right]^{1/2} = \frac{\omega}{c} a(1 - ib), \quad (1.30)$$

where

$$a = \left[\epsilon_2 \frac{\epsilon_{r1}(\epsilon_2 + \epsilon_{r1}) + \epsilon_{i1}^2}{(\epsilon_2 + \epsilon_{r1})^2 + \epsilon_{i1}^2} \right]^{1/2} \quad (1.31)$$

and

$$b = \frac{\epsilon_2 \epsilon_{i1}}{\epsilon_{r1}(\epsilon_2 + \epsilon_{r1}) + \epsilon_{i1}^2} \quad (1.32)$$

Equation (1.30) simplifies if we consider the following cases:

- If $|b| \ll 1$

$$q \approx \frac{\omega}{c} a \left(1 - \frac{ib}{2} \right) \quad (1.33)$$

- If $|b| \gg 1$

$$q \approx \frac{\omega}{c} a \left(\frac{b}{2} \right)^{1/2} (1 - i) \quad (1.34)$$

- If $|b| \approx 1$

$$q \approx \frac{\omega}{c} a (1 + b^2)^{1/2} \left[\cos \left(\frac{\tan^{-1} b}{2} \right) - i \sin \left(\frac{\tan^{-1} b}{2} \right) \right]. \quad (1.35)$$

Making use of equations (1.30) to (1.35) we notice in equations (1.26) and (1.28) that when $|\epsilon_{i1}| < |\epsilon_{r1}|$ and $\epsilon_{r1} < 0$, then $Re(q) \neq 0$ indicating a propagating wave, moreover $Re(p_1)$ and $Re(p_2)$ will be > 0 indicating decaying fields away from the interface. When these conditions are satisfied, localized SPhP modes can propagate at the surface of materials.

1.2 Application of Surface Phonon Polaritons

“There’s plenty of room at the bottom” was an invitation by the famous physicist Richard Feynman, back in 1959, to enter a new field of science: the field of nanotechnology. Nanotechnology is considered to be the manipulation of matter with at least one dimension sized from 1 to 100 nanometers. Since then, we started living in an age of “nano-mania”. Everything nano is considered to be exciting and worthwhile. In the last few decades many countries have initiated research in the field of nanotechnology and its practical applications are seen today in different areas of the industrialized world. For example, our communication system has been advanced over the years because having a large number of transistors in smaller and denser integrated circuits was made possible by nanotechnology. The manipulation of matter in low dimensions has also provided the possibility of delivering drugs to specific cells using nanoparticles, improving the techniques used for curing different diseases. As a result, the sub-branches of nanotechnology such as nanomedicine, nanobiotechnology, nanoelectronics, nanoart, etc. have now become independent areas for active scientific research.

A sub-field of nanotechnology that has attracted wide scientific interest over the last couple of decades is the field of nanophotonics. Nanophotonics deals with the interaction of light with matter on a nanometer size scale, which conceptually can be divided into three different parts. One way of generating light-matter interaction is to confine light in dimensions much smaller than the wavelength of the radiation itself. This happens by coupling light with elementary excitations of the material such as phonons explained in section 1.1, and it will be the focus of our work in the coming chapters. Another approach of inducing light-matter interaction is to confine matter in nanometer size hence limiting interactions in

nanoscopic dimensions. This paves the way for the development of nanomaterials. The last way is to induce photochemistry or a light induced phase change in the nanoscale, which provides methods for manufacturing photonic structures and functional units. Nanophotonics is considered to be a relatively new field that has great potential of creating opportunities for the development of new technologies.

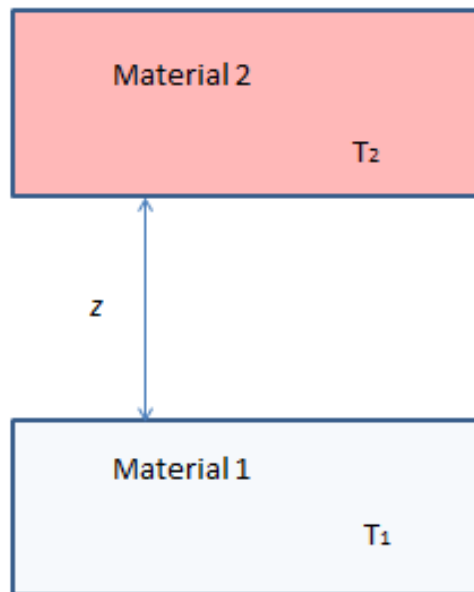


Figure 1.6: Two semi- infinite planes at two different temperatures T_1 and T_2 separated by a distance z .

As mentioned earlier the primary focus of our work is to study the confinement of light in sub diffraction limits in the form of SPhP waves. It has been demonstrated that localized radiation such as surface polaritons play a major role in describing the transfer of heat in low dimensions. A classical description of heat transfer in the form of radiation was introduced by Planck in 1900. Every

object at a given temperature emits thermal energy in the form of electromagnetic radiation whose intensity is determined by the temperature of the object. Considering two different materials at two different temperatures (figure 1.6), the exchange in radiation energy contributes to the transfer of heat between them. In an ideal case, this radiation will be described by Planck's blackbody radiation

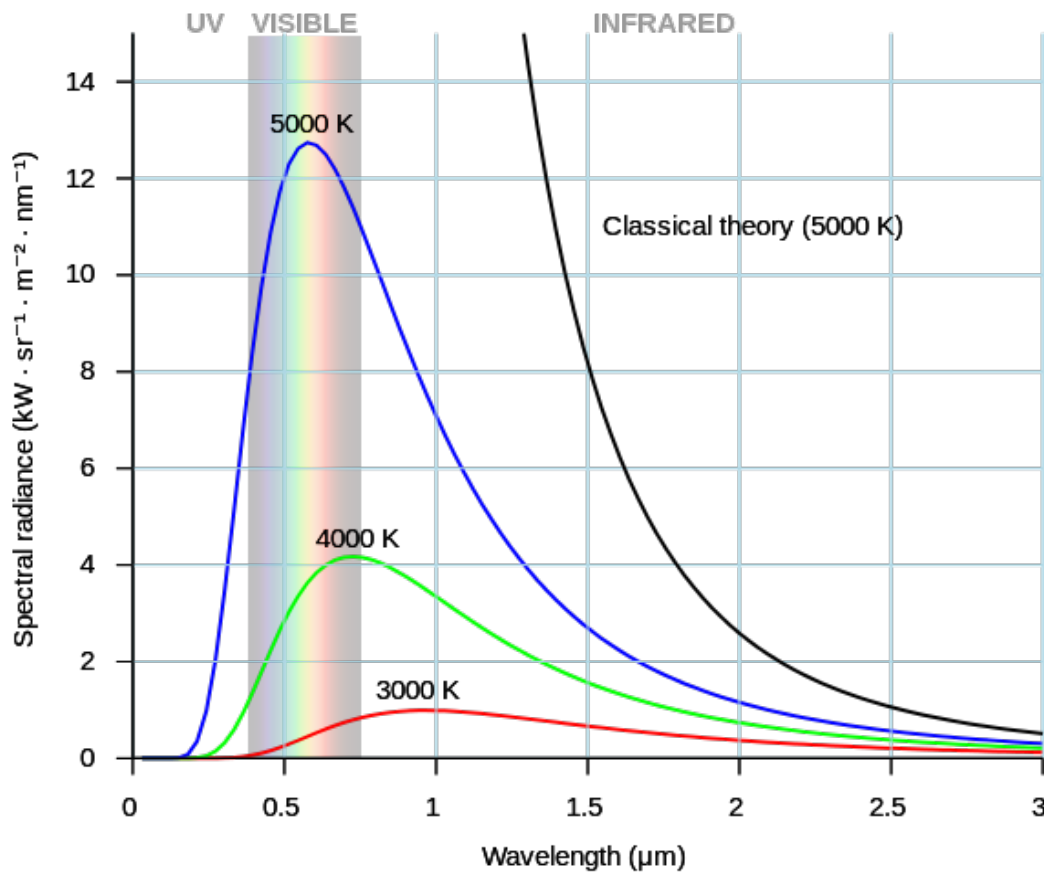


Figure 1.7: Planck's blackbody radiation presented at different temperatures.

tion (Figure 1.7). The wavelength at which the highest intensity is observed is called the peak wavelength. However, what happens if the distance between the two materials becomes smaller than the peak wavelength of the radiated energy? Does Planck's blackbody radiation still hold as an accurate description?

As is the case in many systems, different behaviors emerge in microscopic

scales. Recently, Sebastian Volz [1] calculated the energy density emitted by a silicon oxide (SiO_2) sample as a function of distance away from its surface at room temperature (300K). (Figure 1.8). The peak wavelength of SiO_2 at 300K

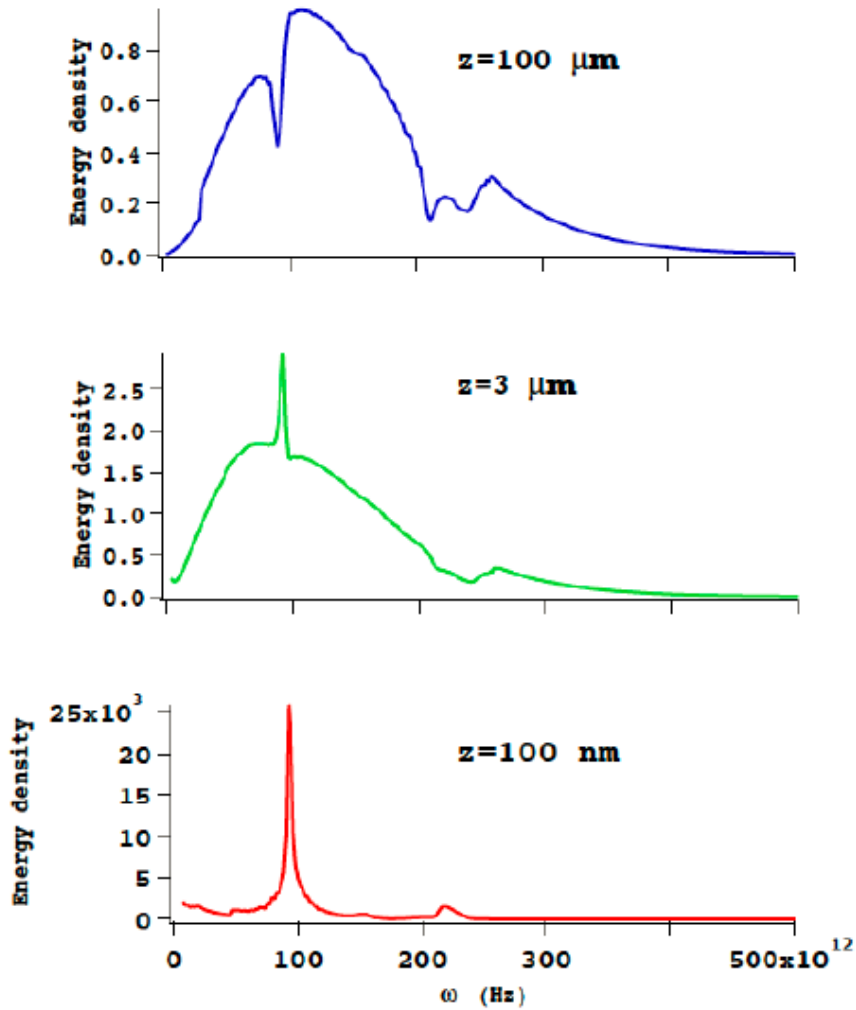


Figure 1.8: Energy density of SiO_2 calculated at 3 different heights at a temperature of 300 K. The energy density increases due to contributions from the near field radiation. [1]

is about 3μ . At distances larger than $3 \mu\text{m}$, Planck's distribution is still valid. This is because the distance at which the energy density is evaluated is larger than

the peak wavelength being emitted. The system is considered to be in the far-field. The measured distribution is not exactly the same as Planck's distribution since the sample used is SiO_2 which is not a perfect blackbody. At distances comparable to $3 \mu m$, the emitted energy density exceeds that of the blackbody radiation. This is due to the presence of localized electromagnetic fields such as SPhP that start having their own contribution to the radiated energy density. Being localized waves, they acquire an evanescent character as they move away from the surface and cannot be detected in the far field. However at distances smaller than the peak wavelength, they can transfer energy from one sample to another by tunneling effects. This is known as near field radiation. Finally as we can see in (Figure 1.8), in the nanoscale regime the energy transfer due to surface waves is orders of magnitude larger than that of Planck's radiation. Therefore, the heat transfer can be significantly enhanced by bringing close two samples at distances much smaller than the wavelength, where the contribution due to localized surface waves is dominant.

1.2.1 Monochromatic and Coherent Light– Emitting Thermal Sources

Unlike lasers that are highly monochromatic and coherent light sources, thermal sources such as black bodies, are often presented as incoherent sources emitting light over a wide range of frequencies. The frequency spectrum emitted by a thermal source is described by Planck's radiation explained earlier. However in the near- field regime, the electromagnetic radiation emitted by a polar material becomes almost monochromatic. As we can see in (figure 1.8) the energy density emitted at a distance of 100 nm presents a narrow peak around 95 THz . This

is due to the fact that surface waves exist within a narrow range of frequencies (where the real part of dielectric function is negative, as explained in section 1.1.3) giving them a monochromatic character.

Surface polaritons are nonradiative localized surface waves by nature. They cannot be detected over distances larger than the wavelength. However it was

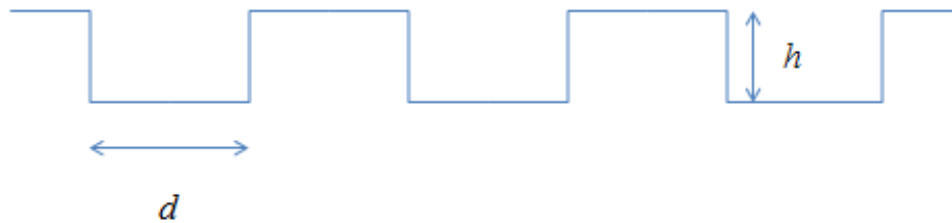


Figure 1.9: Grating introduced on the surface a polar material having a periodicity $2d$ and height h .

demonstrated [5] that by introducing a periodic structure (Figure 1.9) on the surface of polar materials, surface polaritons can be emitted into the far-field. In the presence of a grating, SPhP modes become radiative upon interaction with the periodic profile of the surface. In order to understand the physical mechanism governing the emission of the surface waves we have to study the effect of the grating on the dispersion relations of these waves. In (Figure 1.10) we show the dispersion relations of SPhP waves in aluminum nitride (AlN) crystals. The region of existence of the SPhP modes is within the frequency range of 612 cm^{-1} to 840 cm^{-1} (this will be explained in more detail in chapter 4). As we can see, the dispersion relation of the SPhP modes (blue curve, Figure 1.10) lies outside the cone of light (red curve, Figure 1.10) and therefore cannot be radiated. However when a grating is introduced on the surface of the crystal, the wavevector of the SPhP wave will interact with the periodicity of the grating which results in folding the dispersion relation into the cone of light (Figure 1.11). The portion of

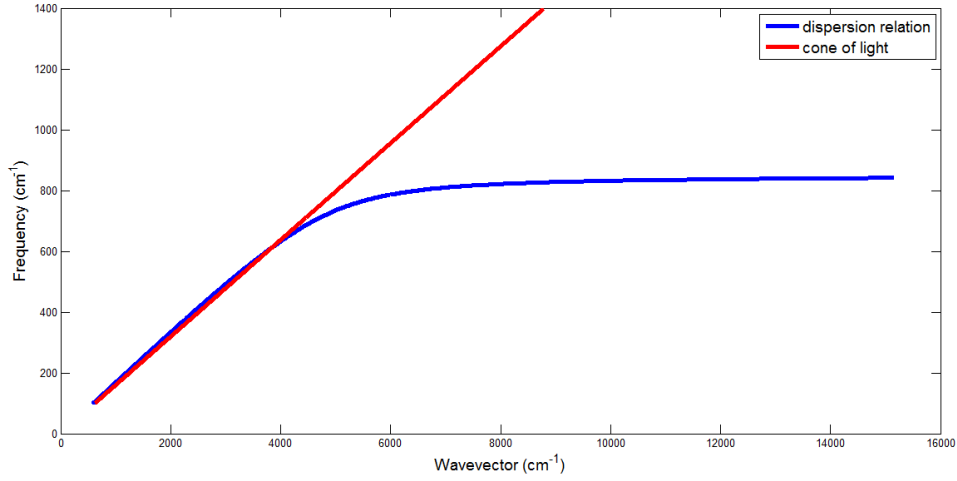


Figure 1.10: Dispersion relation of SPhP in AlN crystal (blue curve). Cone of light (red curve).

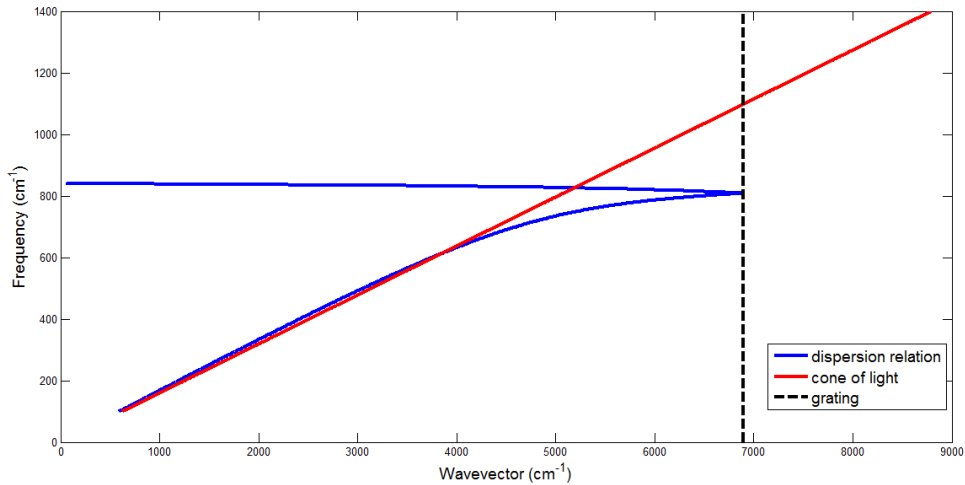


Figure 1.11: Dispersion relation of SPhP on a grating. Blue curve represents the folded dispersion relation due to the interaction of SPhP waves with the periodicity of the grating. The period of the grating is $23 \mu m$. The red curve represents the cone of light. The portion of the dispersion relation that lies in the cone of light can be radiated in the far-field.

the dispersion relation that lies in the cone of light (Figure 1.11) represents the SPhP modes that can be radiated into the far-field. We also notice that these modes span over a narrow range of frequencies (around 810 cm^{-1} to 840 cm^{-1}) in the cone of light. Therefore a monochromatic light can be emitted by thermally

exciting the SPhP modes upon coupling to a periodic grating.

In addition, it has been demonstrated (Greffet) that the SPhP modes present a certain degree of temporal coherence when radiated into the far- field. Temporal coherence is a measure of the average correlation of an electromagnetic wave with itself after a certain time delay. In other words, it tells us how monochromatic a source is. It is known that the width of the emission spectrum is inversely proportional to coherence time. Comparing the width of the energy density emitted by the SPhP modes to that of Planck's radiation in (Figure 1.8) we can clearly see that SPhP modes present a much longer temporal coherence when radiated as compared to the black body radiation. In a black body radiation, atoms are randomly excited by thermal energy and an incoherent light is emitted due to that randomness. However in a polar material, thermal energy leads to the collective coherent excitation of the atoms giving rise to optical phonons. Since SPhP modes are the result of the coupling between optical phonons and electromagnetic waves, the electromagnetic energy emitted by the SPhP modes will receive the coherence of the phonons to some extent. Therefore thermal nanosources can be developed to emit monochromatic and coherent infrared radiation in the far-field.

1.2.2 Cancer Treatment

In parallel to the emission of SPhP waves and its potential applications in the field of nanophotonics, the absorption of incident radiation by surface excitations can also play a significant role in various technological applications. A form of surface excitation that has attracted wide scientific interest over the last few decades is the surface plasmon polariton (SPP). Similarly to SPhP modes, SPP modes result from the coupling of collective electronic oscillations (plasmons)

with electromagnetic modes (photons) at the surface of metals. SPP modes can absorb radiation in the visible and infrared regions of the light spectrum which shows great potential for the development of useful medical devices. In this section we will first discuss the role that SPP modes play in cancer treatment nowadays, and then introduce a SPP based model promising a more efficient way of targeting harmful cells.

Hyperthermia, which is the localized elevation of temperature, is a very old method for treating different types of diseases. This approach was used for centuries for the treatment of breast cancer.[6] One of the methods employed was to put the tumor in contact with a piece of metal heated at high temperatures in order to kill the cancerous cells. Another approach was to immerse the whole body in hot water and elevate the body temperature. All of these techniques seem to be primitive. However due to the presence of nanoparticles nowadays; hyperthermia is one of the most promising methods for cancer treatment alongside radiotherapy, chemotherapy and surgery. In fact, hyperthermia using nanoparticles can be made very selective in targeting only malignant cells, and leaving the healthy cells unaffected which is not the case for radiotherapy and chemotherapy. Cancerous cells are more sensitive to temperature changes and there are essentially two ways for applying hyperthermia: heating the tumor up to 42-45 °C for few hours which leads to apoptosis (cell suicide) or heating up to 50 °C (thermoablation) for few minutes and directly killing the cells under consideration.

Thermoablation poses many problems because high temperatures close to 50 °C can damage healthy cells and lead to negative side effects.[7] Hyperthermia at moderate temperatures is preferable even if it requires the coupling of nanoparticles to external radiations.[6, 7] The use of nanoparticles has two main objectives: one is to target only malignant cells and second to precisely control the temper-

ature in the vicinity of the cancerous cells. By attaching specific antibodies or

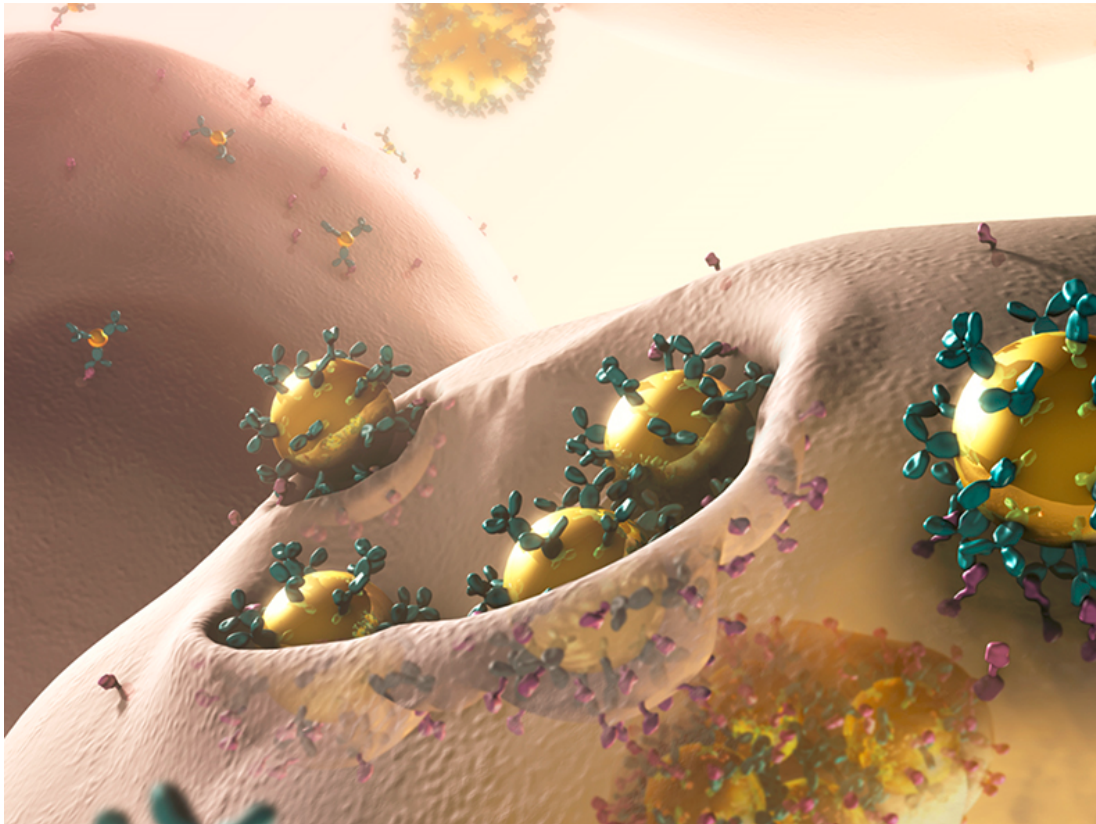


Figure 1.12: Fixing nanoparticles on cancerous cells with the help of specific antibodies.

other biological molecules to the nanoparticle, the latter can be fixed on the malignant cells (Figure 1.12).[8] These nanoparticles having sizes of tens or hundreds of nanometers in diameter are made out of gold. They show a high absorption in the IR regime due to coupling of incident light with surface plasmon oscillations as mentioned earlier.[8, 9] Once the body of the patient is radiated by infrared light, the radiation will be absorbed by the nanoparticles and will be dissipated in the form of heat. This results in highly localized temperature elevation surrounding the nanoparticles, and consequently the destruction of the cancerous cells. However, infrared radiation penetrates the skin not more than a few millimeters. This poses limitations on the use of gold nanoparticles that can

be effective only if the tumor is very close to the skin (at a distance that can be reached by the incident IR radiation). Therefore an alternative method is needed for treating cancer tumors deep inside the body.

A more promising technique for curing cancerous cells follows the same methodology of hyperthermia with two major modifications. The first modification is the replacement of the incident infrared radiation with an alternating magnetic field. Unlike infrared radiation, the incident magnetic field is not bounded by any penetration depth. The second modification is the replacement of gold nanoparticles with polar nano-materials doped with free charge carriers such as electrons. When exposed to an incident alternating magnetic field, the charge carriers start to rotate and as a result generate heat inside the polar samples. This will excite coherent and monochromatic SPhP modes at the surface of the nanoparticles. Thus, by accurately matching the frequency of the near field radiation (i.e. the SPhP modes) to the natural vibrational frequency of the cancer tumor, the latter can absorb the energy density radiated in the near field and can be destroyed by resonance.

The challenging part of this technique is to find the right material that can support a SPhP mode with the desired frequency that resonates with the tumor. Moreover, a healthy cell in the vicinity of the tumor having a natural frequency close to that of the tumor, can be damaged if the frequency of the near field radiation is not finely tuned. Therefore a precise tuning of the SPhP modes is crucial for accurately targeting only malignant cells while keeping healthy cells unaffected. In this thesis work we will provide three different methods for tuning various properties of SPhP modes.

1.3 Experimental Detection of SPhP Waves

The coupling of SPhP modes with the periodicity of a grating introduced on the surface of a material allows the surface polaritons to be emitted in the far-field as described earlier. Apart from this particular case, SPhP modes are localized electromagnetic modes at the surface of a material that acquire an evanescent character away from the surface. Due to the non-radiative nature of those surface waves it is challenging to observe them experimentally. We will present in this section some of the techniques developed for detecting the SPhP modes.

1.3.1 Attenuated Total Reflection (ATR)

The ATR technique is widely used for detecting surface waves such as SPhP modes, surface plasmon polaritons and others.[10, 11, 12] The ATR configuration consists of a dielectric material (supporting SPhP waves) and a prism separated by a certain distance d (Figure 1.13). Considering an incident beam in the prism with an angle of incidence ϕ , such that $\sin^{-1}\left(\frac{n_2}{n_1}\right) < \phi < \frac{\pi}{2}$, a total internal reflection will be observed. An important side effect of the internal reflection is the appearance of an evanescent wave at the prism/ air boundary having a wavevector $q_{prism} = \frac{\omega\sqrt{\epsilon_3}}{c} \sin(\phi)$. Upon coupling these surface waves with SPhP modes at the air/ dielectric boundary, energy will be transferred from the prism to the polar sample and a dip in the reflected intensity will be observed (Figure 1.14). This will indicate the existence of SPhP modes at the air/ dielectric interface.

Evidently the dispersion curves of the SPhP waves can be obtained by varying the angle of incidence (i.e. the wavevector) and the frequency and detecting the

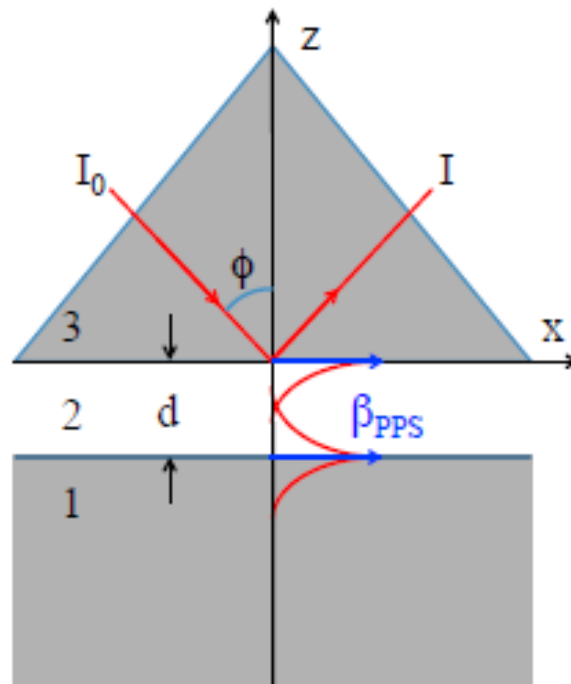


Figure 1.13: A diagram showing the ATR setup. Region 3 is the prism, region 2 is air and region 1 is the polar material where SPhP waves are excited.

dip in the reflected intensity. The complex dielectric function of the polar sample requires the wavevector or the frequency to be complex. When the angle of incidence is fixed and the frequency is varied, the minimum of the reflectance is measured at a real wavevector and a complex frequency. The position of the dip determines the real frequency and the width of the dip determines the imaginary part of the complex frequency. Similarly, when the frequency is fixed and the angle of incidence is varied, the minimum will be measured at a real frequency and a complex wavevector. In this case the width of the minimum will determine the imaginary part of the complex wavevector.

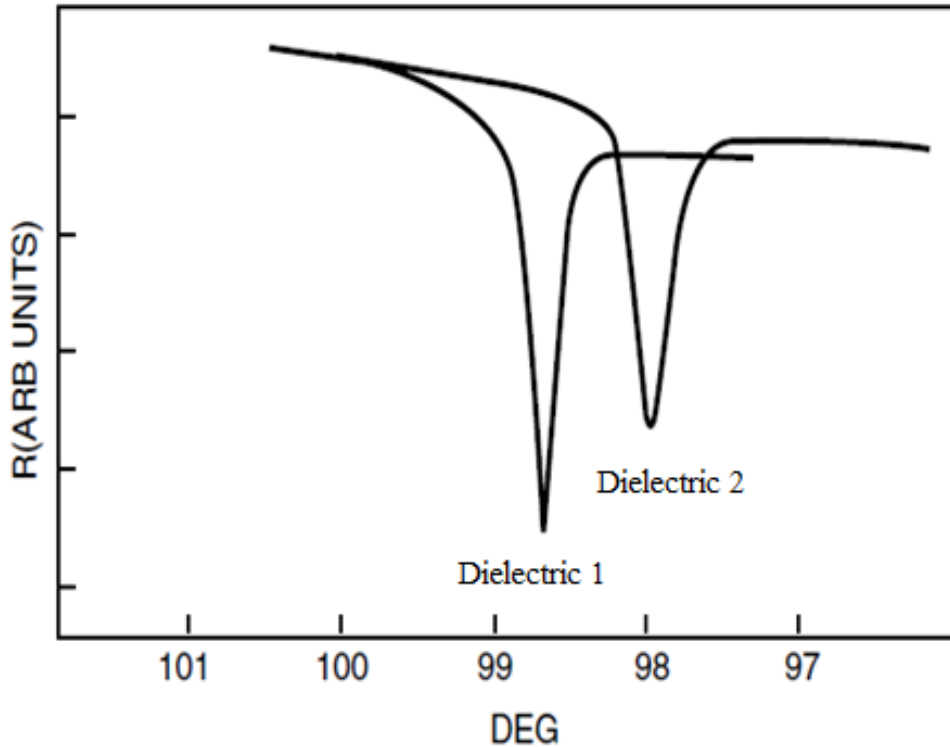


Figure 1.14: A dip in the reflected intensity is observed due to coupling of surface waves at the prism with SPhP modes. Reflectivity curves of arbitrary units are shown for two different dielectric materials. Each sample shows a dip in reflectivity at different incident angles. This means that SPhP modes of different energies are excited at the surface of the two different dielectric materials.

1.3.2 Scanning Near Field Optical Microscopy (SNOM)

A second method for detecting SPhP modes consists of an atomic force microscope (AFM) with a small modification in its use. This technique relies on the diffraction of near field radiation by bringing a dipole moment very close to the dielectric surface where SPhP modes exist. The surface wave excites the dipole moment which in turn radiates electromagnetic energy proportional to that of the surface wave (Figure 1.15). The tip of the atomic force microscope plays the role of the dipole moment in the experiment, which is made of a metallic

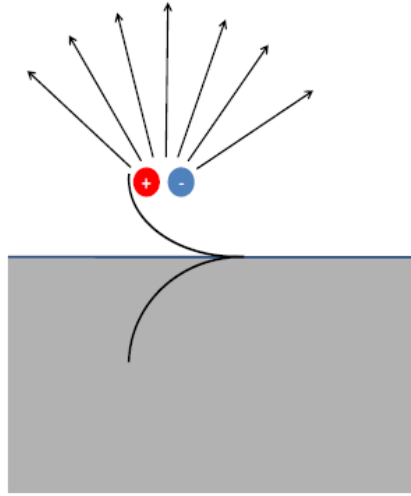


Figure 1.15: The concept of SNOM: Diffraction of near field radiation into the far field, making use of a dipole excitation.

material having a radius in the order of 20 to 30 *nm*. The AFM is set at tapping mode meaning that the tip oscillates on top of the sample (with a frequency *F*), periodically being in contact with the surface. [13, 14, 15, 16]

Huber et al. demonstrated a method for optically exciting SPhP waves. A metallic thin film is deposited on the Dielectric substrate as shown in (Figure 1.16). SPhP waves are excited by diffracting the radiation incident from a laser at the border of the metallic film. The longitudinal component of the incident field at the border of the thin film can be written as

$$E_0 = E_i e^{-ik \cos(\alpha)x}, \quad (1.36)$$

where E_i is the amplitude of the incident field, k is the wavevector of the incident field and α is the angle between the surface and the incident wave. The electric

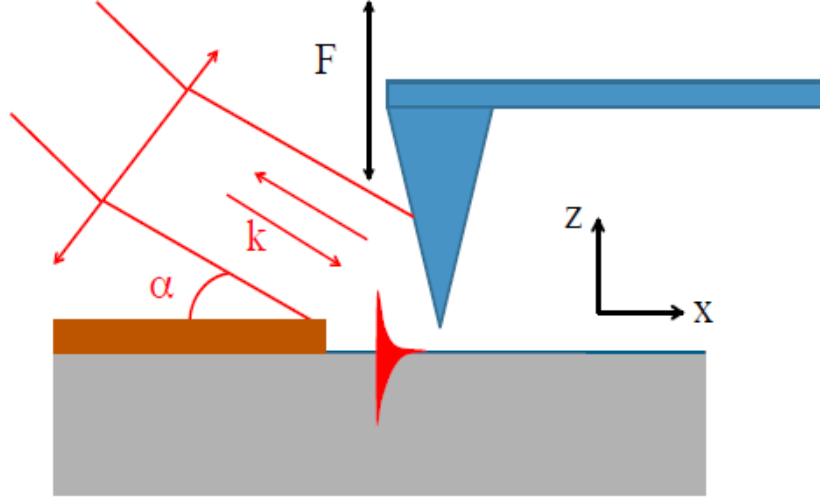


Figure 1.16: Experimental setup of SNOM: the tip diffracts the near field and reflects the incident field. The interference of the two waves is used to measure the SPhP. The near field is excited by the diffraction of the incident radiation at the border of the metallic thin film.

field of the SPhP can be related to E_0 in the following way:

$$E_{SPhP} = f_0 e^{i(qx + \phi_0) - p|z|} E_0, \quad (1.37)$$

with f_0 being the ratio of the SPhP and incident field amplitudes $\left(f_0 = \frac{E_{SPhP}(x=0, z=0)}{E_i}\right)$, ϕ_0 is the excitation phase at the origin, q and p are the longitudinal and transverse components of the near field wave. The incident wave illuminates both the metallic surface and the tip of the AFM, therefore the electric field at the tip can be written as the sum of the incident field and the near field

$$E_{tip}(x, z) = [1 + f_0 e^{-ik \cos(\alpha)x e^{i(qx + \phi_0) - p|z|}}] E_i. \quad (1.38)$$

The electric field re-emitted by the tip will be expressed as

$$E = \alpha_{eff} E_{tip}, \quad (1.39)$$

where α_{eff} is the effective polarizability describing the coupling between the near field and the dipole at the tip. The problem is that the detector measures the field radiated by the tip but also the reflected laser beam whose amplitude is much larger as compared to that coming from the tip. Since the AFM is set at tapping mode with some frequency F , the amplitude of the field diffracted by the tip will generate an alternating signal having a frequency F , while the reflected laser beam will be unaffected by the oscillation of the tip (generating a dc signal). A modulating detector set at a frequency nF (n being an integer) can be used to amplify the alternating signal. This allows the measurement of the field emitted only by the tip, and as a result detecting the SPhP modes. Therefore SNOM presents an alternative method to ATR for experimentally determining the dispersion curves of SPhP modes.

Chapter 2

Measurement Technique and Analysis

It was demonstrated in chapter 1 that the dispersion relations of SPhP waves depend on the complex dielectric function of the polar material. The dielectric function is the response describing the degree of polarization of the material when exposed to an incident electromagnetic radiation. Thus, the knowledge of the response function is crucial for investigating the properties of the SPhP modes. The quantity that is accessible experimentally is the reflectivity spectrum which is completely determined by the response function. In this chapter we will describe the technique used for measuring the reflectivity spectra (FTIR) and explain the mathematical method for deducing the complex dielectric function (Kramers- Kronig).

2.1 Fourier Transform Infrared Spectroscopy

Surface polaritons result from the coupling of infrared radiation with zone center optical phonon modes. In the infrared regime the complex dielectric function is highly due to the response of optical phonons to the incident radiation. Therefore measuring the reflectivity spectrum will give us enough information to study the behavior of optical phonons and accordingly deduce the properties of SPhP modes. The most common way of measuring an infrared spectrum is known as the Fourier Transform Infrared Spectroscopy (FTIR). The main component of an FTIR spectrometer is an interferometer based on the original design by Michelson in 1891.[17] Thus, we will explain briefly the concept behind the Michelson interferometer when a monochromatic light is used, then we will demonstrate how a reflectivity spectrum can be obtained over a certain range of frequencies.

2.1.1 Michelson Interferometer

For simplicity we consider a source S of monochromatic radiation (having some wavelength λ) entering the interferometer (Figure 2.1). The incident ray strikes a beam splitter which is coated with a material that makes it half reflecting (ray 1) and half transmitting (ray 2). Ray 1 gets reflected back into the beam splitter and eventually into the detector by a movable mirror M_1 . Ray 2 on the other hand will be reflected by a fixed mirror M_2 , and guided back into the detector upon reflection at the beam splitter. The two rays will travel different paths before reaching the detector with a certain path difference δ . The path difference between the two rays can be varied by changing the position of the movable mirror M_1 . If $\delta = 0, \lambda, 2\lambda, \dots$ then the two rays will interfere constructively at the detector. However when $\delta = \lambda/2, 3\lambda/2, 5\lambda/2, \dots$ then a destructive

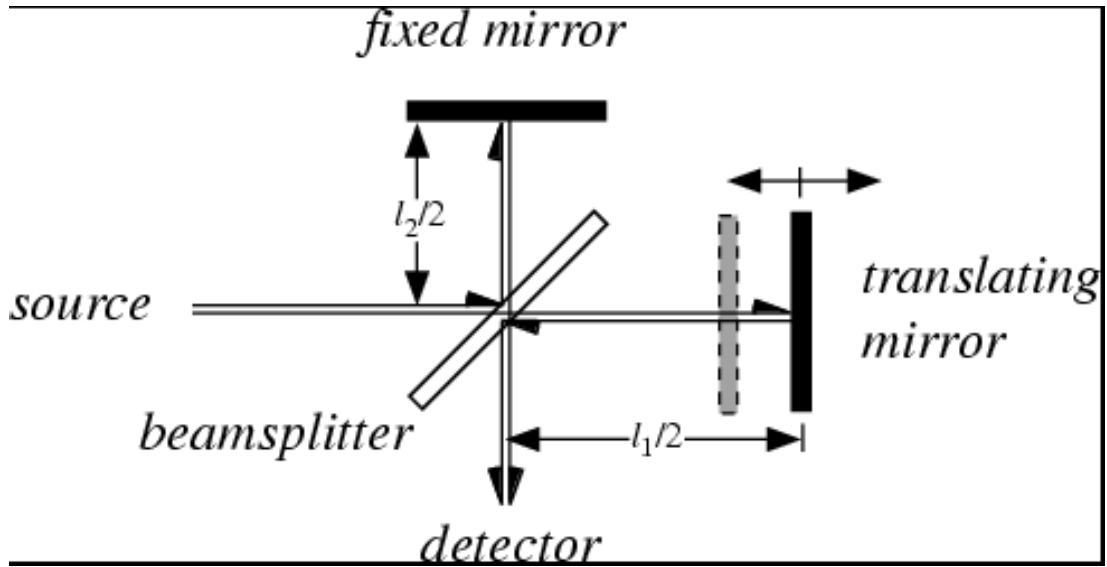


Figure 2.1: Michelson interferometer having a monochromatic source S, a translating mirror M_1 , a fixed mirror M_2 , a beam splitter and a detector.

interference will be measured. Therefore by smoothly varying the path difference δ the intensity $I(\delta)$ detected will change like a cosine function given by

$$I(\delta) = B(\sigma) \cos(2\pi\sigma\delta), \quad (2.1)$$

where σ is the inverse of the wavelength also known as the wavenumber, and $B(\sigma)$ is the intensity of the source at a given wavenumber σ .

2.1.2 Reflectivity Spectrum

In a more usual setting, the source will contain a white light in order to obtain a spectrum of light within a wide range of wavenumbers. The reflectivity of a material is measured by exposing the sample to a polychromatic infrared radiation, and the light reflected by the sample will be used as the source in the FTIR spectroscopy. Unlike the monochromatic source, the intensity detected in this case will be a combination of many cosine functions as described in equation

(2.1). Therefore the total detected intensity $I(\delta)$ can be written as an integral over all wavenumbers

$$I(\delta) = \int_{-\infty}^{+\infty} B(\sigma) \cos(2\pi\sigma\delta) d\sigma. \quad (2.2)$$

Using a Fourier transform technique, which is a mathematical transformation, the intensity of the source for each wavenumber can be evaluated

$$B(\sigma) = 2 \int_0^{+\infty} I(\delta) \cos(2\pi\sigma\delta) d\delta. \quad (2.3)$$

As mentioned earlier, the source used is an infrared light reflected by the sample under consideration. Therefore a plot of $B(\sigma)$ against σ will describe the reflectivity spectrum of the sample. It is assumed in equation (2.3) that the movable mirror can be displaced over an infinite distance, which is surely not the case. In reality, the path difference will be bounded by a maximum value δ_{max} , which implies that the integral in equation (2.3) will be taken over a finite range of path differences. This determines the resolution of the measured spectrum defined as $\Delta\sigma_{max} = 1/\delta_{max}$. Once the reflectivity spectrum is obtained, the response function of the material can be calculated using the Kramers- Kronig conversion technique.

2.2 Kramers–Kronig Conversion Technique

2.2.1 Relationship between the complex dielectric function and reflectivity

The reflectivity spectra obtained by FTIR measurement can be described by Fresnel equations of reflectivity. The Fresnel coefficient of reflectivity is defined as the ratio of reflected electric field (E_r) to incident electric field (E_i) and is related to the complex response function in the following way

$$r(\omega) = \frac{E_r}{E_i} = \frac{\sqrt{\epsilon(\omega)} - 1}{\sqrt{\epsilon(\omega)} + 1}. \quad (2.4)$$

The Fresnel coefficient of reflectivity is a complex function itself which can be written as

$$r(\omega) = \rho(\omega)e^{i\theta(\omega)} \quad (2.5)$$

where $\rho(\omega)$ is the amplitude and $\theta(\omega)$ is the phase. The quantity being measured is the reflectivity which is defined as the complex conjugate of the Fresnel coefficient of reflectivity

$$R(\omega) = rr^* = \rho(\omega)^2. \quad (2.6)$$

Unlike the amplitude $\rho(\omega)$ which is a real quantity, the phase $\theta(\omega)$ cannot be directly measured because it is an imaginary quantity. However it is possible to determine $\theta(\omega)$ using a Kramers–Kronig conversion technique if the reflectivity $R(\omega)$ is known for all frequencies.

2.2.2 Kramers–Kronig Relations

The Kramers–Kronig conversion technique is a mathematical tool that allows the evaluation of the real part of the dielectric function if the imaginary part is known for all frequencies and vice versa. The complex response function of a system of damped harmonic oscillators can be written as

$$\epsilon(\omega) = \epsilon_1(\omega) + i\epsilon_2(\omega) = \sum_j \frac{f_j}{\omega_j^2 - \omega^2 - i\Gamma_j\omega} = \sum_j f_j \frac{\omega_j^2 - \omega^2 + i\Gamma_j\omega}{(\omega_j^2 - \omega^2)^2 + \omega^2\Gamma_j^2} \quad (2.7)$$

where the constants f_j and the dampings Γ_j are positive. A more detailed derivation of the complex dielectric function will be presented in the following chapters. In order to apply the Kramers–Kronig relations, a function must satisfy the following conditions:

1. The poles of $\epsilon(\omega)$ must be below the real axis.
2. The integral of $\epsilon(\omega)/\omega$ taken over an infinite semi-circle in the upper region of the complex plane must tend to zero. In other words, $\epsilon(\omega) \rightarrow 0$ as $|\omega| \rightarrow \infty$.
3. The real part $\epsilon_1(\omega)$ should be an even function while the imaginary part $\epsilon_2(\omega)$ an odd function with respect to the real variable ω .

We consider now the following Cauchy integral:

$$\epsilon(\omega) = \frac{1}{i\pi} P \int_{-\infty}^{+\infty} \frac{\epsilon(\Omega)}{\Omega - \omega} d\Omega = \epsilon_1(\omega) + i\epsilon_2(\omega) \quad (2.8)$$

where P is the main part of the integral. As we saw in condition (2) this integral equals to zero when taken over an infinite semi-circle in the upper region of the

complex plane. Therefore by equating the real parts in equation (2.8) we find

$$\epsilon_1(\omega) = \frac{1}{\pi} P \int_{-\infty}^{+\infty} \frac{\epsilon_2(\Omega)}{\Omega - \omega} d\Omega = \frac{1}{\pi} P \left[\int_0^{+\infty} \frac{\epsilon_2(\Omega)}{\Omega - \omega} d\Omega + \int_{-\infty}^0 \frac{\epsilon_2(\lambda)}{\lambda - \omega} d\lambda \right] \quad (2.9)$$

Replacing λ by $-\Omega$ and using the fact that $\epsilon_2(-\Omega) = -\epsilon_2(\Omega)$ we arrive at

$$\epsilon_1(\omega) = \frac{2}{\pi} P \int_0^{+\infty} \frac{\Omega \epsilon_2(\Omega)}{\Omega^2 - \omega^2} d\Omega \quad (2.10)$$

Therefore by knowing the imaginary part for all frequencies, the real part of the dielectric function can be evaluated. Equating the imaginary parts in equation (2.8) and using the fact that the real part is an even function, an expression for the imaginary part of the response function can be found,

$$\epsilon_2(\omega) = -\frac{2\omega}{\pi} P \int_0^{+\infty} \frac{\epsilon_1(\Omega)}{\Omega^2 - \omega^2} d\Omega \quad (2.11)$$

Similarly, the imaginary part of the dielectric function can be calculated if the real part is known for all frequencies.

2.2.3 Application of the Kramers–Kronig Relations to the Reflectivity

In order to apply the Kramers–Kronig relations to the reflectivity, we take the logarithm of the Fresnel coefficient of reflectivity

$$\ln r(\omega) = \ln R(\omega)^{1/2} + i\theta(\omega). \quad (2.12)$$

From FTIR reflectivity measurements $R(\omega)$ will be determined for a certain range of frequencies. Consequently the phase $\theta(\omega)$ can be evaluated using the Kramers–

Kronig relations

$$\theta(\omega) = -\frac{\omega}{\pi} P \int_0^{+\infty} \frac{\ln R(\Omega)}{\Omega^2 - \omega^2} d\Omega \quad (2.13)$$

Integrating equation (2.13) by parts we express the phase in the following way

$$\theta(\omega) = -\frac{1}{2\pi} \int_0^{+\infty} \ln \left| \frac{\Omega + \omega}{\Omega - \omega} \right| \frac{d \ln R(\Omega)}{d\Omega} d\Omega \quad (2.14)$$

Once the amplitude $\rho(\omega)$ and the phase $\theta(\omega)$ are known, we can go back to equations (2.4) and (2.5) to evaluate the real and imaginary parts of the complex dielectric function. The Kramers–Kronig relations require an integration of the reflectivity spectrum from zero to infinity. However, the experimental measurement of the reflectivity is always within a finite range of frequencies. This appears to be a source of error when evaluating the complex dielectric function. A method for correcting the results obtained from the Kramers–Kronig conversion will be introduced in chapter 3.

Chapter 3

Dependence of Surface

Plasmon-Phonon-Polariton in

4H-SiC on Free Carrier

Concentration

In the last few decades, nanophotonics emerged as a frontier research to exploit the interaction of nanoscale phenomena with electromagnetic waves and the nanoscale confinement and guidance of these waves.[18, 19, 20, 21, 22] Extensive research has been conducted to exploit in particular, the confinement and guidance of electromagnetic energy at the surface of a material. [23, 24, 25] The confinement and guidance of electromagnetic energy on the surface of metals in the form of surface plasmon waves have attracted wide interest, but unfortunately, losses due to plasmon waves scattering are significant, making light confinement and guidance at the surface somehow problematic. [26, 27, 28]

In a polar material, the frequencies of the zone center optical phonon modes

are split into longitudinal optical and transverse optical components by the internal macroscopic electric field. This macroscopic electric field serves to stiffen the force constant of the phonon and thereby raise the frequency of the longitudinal optical phonon (ω_{LO}) over that of the transverse optical phonon (ω_{TO}). The frequency range bounded by ω_{TO} and ω_{LO} is known as the Reststrahlen band. Within the Reststrahlen band, the real part of the material response to an electromagnetic excitation $\text{Re}\epsilon$ is negative. This has the consequence that within the Reststrahlen band, electromagnetic plane waves acquire an evanescent character giving rise to modes confined at the surface. These surface modes are known as the surface phonon-polariton (SPhP) modes. Hence, the SPhP can be regarded as surface electromagnetic waves arising from the coupling of electromagnetic modes (photons) with lattice vibration modes (optical phonons) in polar dielectric materials. [26, 29, 30] Relevant research works suggested that the lifetime of SPhP is orders of magnitude larger than that of surface plasmon. [31] This makes SPhP a potential candidate for enhancing the lifetime of electromagnetic energy confined at the surface, contributing to many technological applications in the field of nanophotonics. As such, it has been demonstrated that the SPhP modes are the dominant energy carriers in the near-field and their diffraction by gratings introduced on the material surface produces coherent infrared emission in the far-field.[32, 33, 34, 35, 36]

In an n -doped polar material, the presence of free carriers in the volume of the material results in plasmon electronic longitudinal oscillation modes. Due to their longitudinal nature, these plasmon electronic oscillation modes can couple to only longitudinal optical phonon modes to give rise to a mixed character longitudinal modes of frequencies higher than those of the original longitudinal optical phonon modes.[37, 38] These modes are known as the LOPC modes. On

the surface, however, the plasmon electronic oscillation modes acquire transverse components and hence can couple to transverse surface optical modes.

Indeed, it is highly desirable to examine the interaction and coupling of incident electromagnetic modes with phonon-plasmon mixed character modes both on the surface and in the volume because understanding the underlying mechanisms governing the characteristics of the resultant waves, which will be referred to as the plasmon-phononpolariton (PPhP) modes, can help to rationally design systems for numerous technological applications in nanophotonics.

Phonon-plasmon interactions have been observed by infrared (IR) spectroscopic ellipsometry upon understanding the physical origins of the Berreman-effect. [37, 38] The mechanisms involved in coupling these two different modes have also been explained in the literature. [39, 40] In this chapter, we tackle the particular issue of the coupling between incident electromagnetic modes with phonon-plasmon mixed character modes and present a detailed description on how the free carrier concentration in the crystal affects the characteristics (lifetime, mean-propagation-length, and, most importantly, temporal coherence) of the resultant plasmon-phonon-polariton (PPhP) modes both in the volume and on the surface of the crystal. One of the key developments presented in this paper is that the response functions of the samples investigated are obtained without the use of any physical models or assumptions. They are obtained by correcting the values found from the Kramers-Kronig conversion technique with reference to Fresnel equations for reflectivity.[41]

The material being used to investigate the characteristics of the volume and surface PPhP modes is 4H-SiC. The choice of 4H-SiC is beneficial due to the availability of large area highly crystalline 4H-SiC epilayers, the availability of techniques for doping and controlling the free carrier concentration in SiC, and

due to the fact that the Reststrahlen band of 4H-SiC lies in the spectral range where the response of the commonly used infrared detectors is linear. [26] However, we believe that the fundamental physics outlined in this chapter is applicable in all n-type polar semiconductors.

3.1 Experiments

The experiments were carried out on three *c*-oriented 4H-SiC epilayers (8° off-axis) deposited on unintentionally n-doped 500 μm thick 4H-SiC substrates. The epilayers were 3 μm thick and of $2 \times 10^{15} \text{cm}^{-3}$ initial free carrier concentration. Two of the investigated samples were implanted with different doses of N-ions. [42] The energy of the implantation of the N-ions was decreased from 5.5 MeV to zero systematically in 60 steps in order to ensure uniform distribution of N-ions over the thickness of the implanted epilayer. The implanted samples were then encapsulated with a C cap. The C capping layer was formed by thermal conversion during annealing at 750 °C for 30 min of a spin-coated AZ5214E photoresist layer deposited on the SiC implanted epilayers in a conventional quartz tube furnace under N flux. Then, in order to remedy, as much as possible, the defects formed by ion implantation and activate the N dopants, the implanted samples were annealed at 1650 °C in an RF-induction furnace under Ar atmosphere during 45 minutes with a heating ramp-up at 40 °C/s. Lastly, the capping layer was removed by O_2 plasma in an Alcatel Nextral NE110 RIE reactor. These annealing conditions have been optimized to preserve the root-mean-square surface roughness and lead to a good activation of the N dopants. Hall effect (in standard Van der Pauw geometry) measurements were employed to measure the carrier concentration and mobility in the implanted epilayers. The free carrier

concentration and mobility were measured to be $10^{17}cm^{-3}$ and $620cm^2V^{-1}s^{-1}$ in the slightly implanted epilayer, and $10^{19}cm^{-3}$ and $105cm^2V^{-1}s^{-1}$ in the heavily implanted epilayer. The low carrier mobility in the heavily implanted sample suggests that the adopted annealing process does not remedy all the defects generated by the ion implantation. However, as will be shown below, the ion implantation does not alter the frequency of the transverse phonons. This clearly demonstrates that the ion implantation did not cause extended defects or polymorphism change, and the defects formed are most likely point-like defects that do not alter macroscopic properties such as the dielectric function. Hence, the carrier concentration, which determines the plasmon electronic oscillation frequency, is taken as the only parameter in our work.

Far-field infrared reflectivity measurements were performed on the samples described above. The irradiation of the sample with infrared light and the collection of the reflected infrared light are schematically depicted in Figure 3.1. The incident beam was p-polarized and at 45° from the normal to the sample surface. The incident beam was first expanded and then focused on the surface of the sample, and the reflected light was collected using an integrating sphere in order to record reflectivity spectra averaged over a wide range of incidence angles. The collected light was then collimated and the reflectivity spectrum was obtained using the standard Michelson interferometry technique. A DTGS detector and a KBr beamsplitter were used, and spectra were recorded in the $400 - 3500cm^{-1}$ frequency range. The reflectivity of each sample was compared to that of a gold coated mirror, and the reproducibility of the measurements was checked by measuring each spectrum twice. The two recorded data from each sample were identical within the experimental error, i.e. within 1% reflectivity.

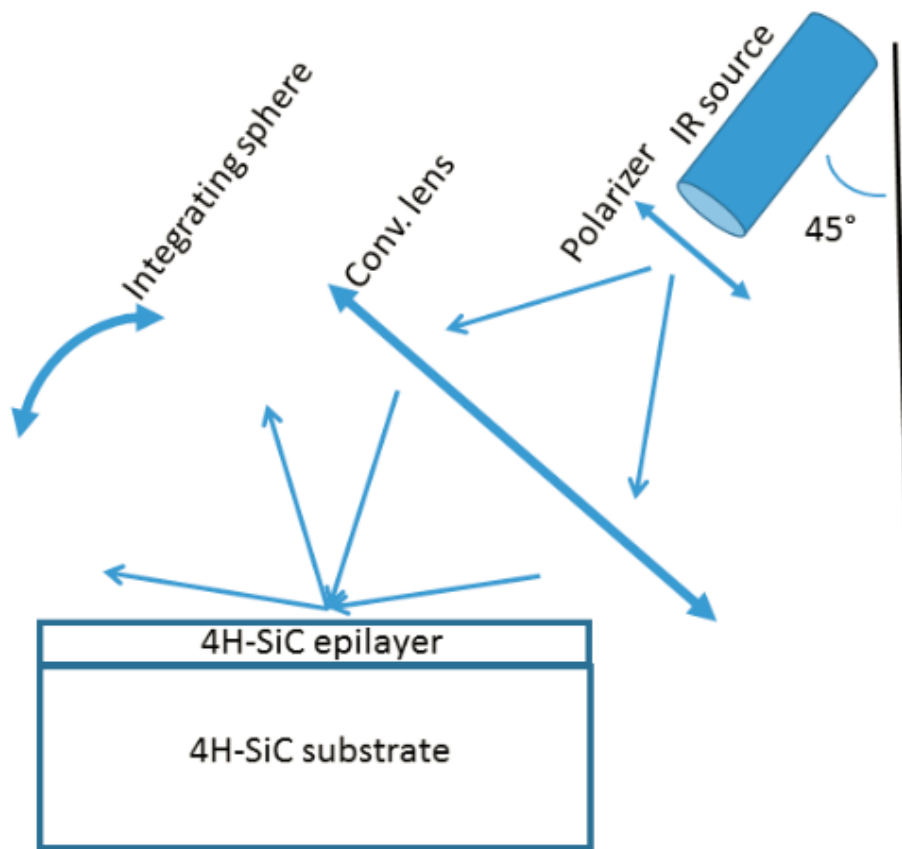


Figure 3.1: Experimental configuration for recording reflectivity spectra averaged over a wide range of incidence angles.

3.2 Analysis of Reflectivity Spectra and Dielectric Spectra by a Corrected Kramers–Kronig Conversion Technique

Reflectivity measurements were carried out in order to deduce from measurements the effective complex dielectric functions of the samples investigated for p-polarized incident light. The usual way of deducing the complex dielectric function from a reflectivity spectrum is to determine the frequency-dependent ampli-

tude $\rho(\omega)$ and phase $\theta(\omega)$ separately using Kramers-Kronig conversion technique, and then the complex dielectric function, or alternatively, the real and imaginary parts of the complex refractive index $N(\omega) = n(\omega) + ik(\omega)$. This conversion technique requires an integration of the reflectivity spectrum from zero to infinity. The experimental data, however, is always obtained within a finite range of frequency (in our case between 400 cm^{-1} and 3500 cm^{-1}). The common way out of this problem is to artificially extrapolate the values at hand to zero and infinity despite the fact that this leads to high margin of error in the results especially at the boundaries of the measured frequency range. [36, 43] Therefore, we proceed by correcting the solutions for $n(\omega)$ and $k(\omega)$ obtained from Kramers-Kronig integral.

3.2.1 Method for Correcting the Kramers–Kronig Conversion

To determine the dielectric properties of the epilayers investigated, we need to determine the dielectric properties of the substrate on which they are deposited. To determine the dielectric properties of the substrate, we first measure the reflectivity spectrum of the substrate (the reflectivity spectrum from the back side of the sample) and deduce its complex refractive index by using the Kramers-Kronig integral.

According to the Kramers-Kronig theorem, the phase equation can be written as

$$\theta(\omega) = -\frac{1}{2} \int_0^{+\infty} \ln \left| \frac{\Omega + \omega}{\Omega - \omega} \right| \frac{d \ln R(\Omega)}{d\Omega} d\Omega \quad (3.1)$$

where ω is the measured frequency and Ω is the integration variable. In order to

implement equation (3.1), we write it in the form

$$\theta(\omega) = -\frac{1}{2} \left[\begin{aligned} & \int_0^{\Omega_0} \ln \left| \frac{\Omega+\omega}{\Omega-\omega} \right| \frac{d \ln R(\Omega)}{d\Omega} d\Omega \\ & + \int_{\Omega_0}^{+\Omega_f} \ln \left| \frac{\Omega+\omega}{\Omega-\omega} \right| \frac{d \ln R(\Omega)}{d\Omega} d\Omega \\ & + \int_{\Omega_f}^{+\infty} \ln \left| \frac{\Omega+\omega}{\Omega-\omega} \right| \frac{d \ln R(\Omega)}{d\Omega} d\Omega \end{aligned} \right], \quad (3.2)$$

where Ω_0 and Ω_f determine the low and high frequency ends of the measured spectrum. We determine $R(\Omega)$ in the first integral of equation (3.2) by extrapolating the measured reflectivity spectrum to zero using the Lorentz-Drude model. Then, the first integral in the phase equation can be readily solved. To solve the second integral, we write it in the form

$$\int_{\Omega_0}^{\Omega_1} d\Omega + \int_{\Omega_1}^{\Omega_2} d\Omega + \int_{\Omega_{i-1}}^{\Omega_i} d\Omega + \int_{\Omega_{f-1}}^{\Omega_f} d\Omega \quad (3.3)$$

and in each interval $[\Omega_{i-1}, \Omega_i]$ (which determines the experimental spectral resolution), we approximate the reflectivity with a linear fit. Then, we obtain the value of the second integral by solving each elementary integral numerically and summing over all the individual integrals. We determine the analytical expression of $R(\omega)$ in the third integral by extrapolating the reflectivity spectrum to infinity using pure mathematical functions and then we solve the third integral numerically. We believe that the arbitrary extrapolation of the reflectivity in the third integral can be a source of error in the determination of the phase. The error on the overall phase depends on the variation of the reflectivity spectrum beyond the measured frequency range. If the reflectivity spectrum saturates beyond the measured frequency range, the contribution of the third integral to the overall phase is nil, and the phase obtained by the Kramers-Kronig conversion technique

is highly accurate. However, if the reflectivity spectrum beyond the measured frequency range varies, the contribution of the third integral to the overall phase in the measured frequency range is an angle that slowly increases as we move towards the high frequency end of the measured spectrum. We present below the procedure we follow for correcting the dielectric properties obtained from the Kramers-Kronig integral.

Let us denote the substrate complex refractive index obtained from Kramers-Kronig by $N'_s(\omega) = n'_s(\omega) + ik'_s(\omega)$. Since the thickness of the substrate is much greater than its skin depth, we can consider the substrate as a semi-infinite medium. In that limit, the Fresnel coefficient of reflectivity can be written as [44]

$$r_{\parallel s} = \frac{E_{\parallel r}}{E_{\parallel i}} = \frac{-N_s \cos \theta_i + \cos \theta_t}{N_s \cos \theta_i + \cos \theta_t}, \quad (3.4)$$

for an incident and reflected electric field in the plane of incidence, and

$$r_{\perp s} = \frac{E_{\perp r}}{E_{\perp i}} = \frac{\cos \theta_i - N_s \cos \theta_t}{\cos \theta_i + N_s \cos \theta_t} \quad (3.5)$$

for an incident and reflected electric field perpendicular to the plane of incidence. Here, $E_{\parallel i}$ and $E_{\parallel r}$ are the incident and reflected electric fields in the plane of incidence, $E_{\perp i}$ and $E_{\perp r}$ are the incident and reflected electric fields perpendicular to the plane of incidence, θ_i and θ_t are the angle of incidence and the angle of refraction, and $N_s = N_s(\omega) = n_s(\omega) + ik_s(\omega)$ is the exact complex refractive index of the substrate. The angles θ_i and θ_t are related according to Snell's law $\theta_t = \sin^{-1}(\sin \theta_i / N_s)$. In the case where both the incident electric field E_i and reflected electric field E_r are unpolarized, the Fresnel coefficient of reflectivity takes the general form

$$r_s = \frac{E_r}{E_i}. \quad (3.6)$$

Now, if we consider that φ is the angle between the incident electric field and the plane of incidence, and χ the angle between the reflected electric field and the plane of incidence equation 3.6 can be written as

$$r_s = \frac{E_r}{E_i} = \frac{E_{\parallel r}}{E_{\parallel i}} \times \frac{\cos \varphi}{\cos \chi} = \frac{E_{\perp r}}{E_{\perp i}} \times \frac{\sin \varphi}{\sin \chi} \quad (3.7)$$

Upon substituting Eq. 3.4 and Eq. 3.5 in Eq. 3.7 we can write

$$\chi = \tan^{-1} \left(\tan \varphi \frac{r_{\perp s}}{r_{\parallel s}} \right) \quad (3.8)$$

Thus, according to Eq. 3.8, if the incident light is p-polarized (i.e., the incident electric field is polarized in the plane of incidence), the reflected light is also p-polarized, and the measured reflectivity should satisfy the condition $R - r_{\parallel s} r_{\parallel s}^* = 0$. Since the measurements in the present work were carried out with p-polarized incident light and the recorded spectra represent average reflectivity spectra over all angles of incidence, the measured reflectivity of the substrate should satisfy the equation

$$R(\omega) - \frac{2}{\pi} \int_0^{\pi/2} r_{\parallel s}(\theta_i, \omega) r_{\parallel s}^*(\theta_i, \omega) d\theta_i = 0. \quad (3.9)$$

In order to determine the exact complex refractive index of the substrate $N_s(\omega) = n_s(\omega) + ik_s(\omega)$, we give a range of possible values for $n_s(\omega)$ and $k_s(\omega)$ in the vicinity of $n'_s(\omega)$ and $k'_s(\omega)$ (which are previously obtained from Kramers-Kronig integral). For instance, we take a range of values for $n_s(\omega)$ where the maximum is 50% greater than $n'_s(\omega)$ and the minimum is 50% smaller than $n'_s(\omega)$ with small steps of 0.001. We also define a range for $k_s(\omega)$ using the same approach. Then, we take $n_s(\omega)$ as a row vector and $k_s(\omega)$ as a column vector to form a mesh with cells corresponding to all possible combinations of $n_s(\omega)$ and

$k_s(\omega)$ in the vicinity of the values obtained from Kramers-Kronig integral. We solve Eq. 3.9 for each cell of the mesh. The combination of $n_s(\omega)$ and $k_s(\omega)$ that gives the best solution to Eq. 3.9 will serve as the actual value of the substrate complex refractive index $N_s(\omega)$. We repeat this procedure at each measured frequency to obtain $n_s(\omega)$ and $k_s(\omega)$ spectra.

Once the exact refractive index of the substrate $N_s(\omega)$ is obtained, we deduce the exact complex refractive index of the epilayer $N(\omega) = n(\omega) + ik(\omega)$ by using the following method. We measure the reflectivity spectrum from the surface of the epilayer. In our case, this reflectivity spectrum is largely determined by the epilayer. This is because the refractive index of the 4H-SiC substrate is very close to that of the lowest doped 4H-SiC epilayer (which drastically decreases the probability of light reflection at the interface between the epilayer and the substrate) and the plasmon electron oscillation in the doped epilayers damps the light rapidly and reduces significantly the skin depth in the epilayers (which make the contribution of the substrate to the overall reflectivity spectrum unlikely). Hence, the Kramers-Kronig conversion of the reflectivity spectrum from the epilayer surface provides an approximated complex refractive index of the epilayer. We denote this approximated epilayer complex refractive index by $N'(\omega) = n'(\omega) + ik'(\omega)$. On the other hand, upon using the transfer matrix method, it can be shown that the Fresnel coefficient of reflectivity from the epilayer-substrate system for an p-polarized incident light can be written as [44]

$$r_{\parallel} = \frac{(m_{11} + \frac{1}{p_3}m_{12}) - (m_{21} + \frac{1}{p_3}m_{22})p_1}{(m_{11} + \frac{1}{p_3}m_{12}) + (m_{21} + \frac{1}{p_3}m_{22})p_1}, \quad (3.10)$$

where $p_i = \cos \theta_i / (N_i / \mu c)$ is the impedance of the i th surface in the air/epilayer/substrate system with N_i being the complex index of refraction of the i th medium, μ

the magnetic permeability, c the speed of light in vacuum, and θ_i the angle of incidence in the i th medium. The angles of incidence in the three media (air/epilayer/substrate) are related to each other according to Snells law. The m_{ij} in Eq. 3.10 are the elements of the interference matrix

$$M = \begin{bmatrix} \cos \phi_2 & -ip_2 \sin \phi_2 \\ -ip_2 \sin \phi_2 & \cos \phi_2 \end{bmatrix} \quad (3.11)$$

where $\phi_2 = \omega N d \cos \theta_2 / c$, with ω being the angular frequency, N the complex index of refraction of the epilayer, and d the epilayer thickness. The measured reflectivity from the epilayer-substrate system should satisfy the equation

$$R(\omega) - \frac{2}{\pi} \int_0^{\pi/2} r_{\parallel}(\theta_i, \omega) r_{\parallel}^*(\theta_i, \omega) d\theta_i = 0. \quad (3.12)$$

Since the complex index of refraction of the substrate N_s (or N_3) is known, the only unknown parameter in Eq. 3.12 is the exact complex index of refraction of the epilayer $N(\omega) = n(\omega) + ik(\omega)$. In order to determine $N(\omega)$, we give a range of possible values for $n(\omega)$ and $k(\omega)$ in the vicinity of $n'(\omega)$ and $k'(\omega)$ (which are obtained by converting the reflectivity from the epilayer surface using Kramers-Kronig integral). Then, we take $n(\omega)$ as a row vector and $k(\omega)$ as a column vector to form a mesh with cells corresponding to all possible combinations of $n(\omega)$ and $k(\omega)$ in the vicinity of the values obtained from Kramers-Kronig integral. We solve Eq. 3.12 for each cell of the mesh. The combination of $n(\omega)$ and $k(\omega)$ that gives the best solution to Eq. 3.12 will serve as the actual value of the epilayer complex refractive index $N(\omega)$. We repeat this procedure at each measured frequency to obtain $n(\omega)$ and $k(\omega)$ spectra. From the knowledge of $n(\omega)$ and $k(\omega)$, the real and imaginary parts of the complex dielectric function

of the epilayer can be readily obtained.

3.2.2 Complex refractive indices of the samples investigated obtained from the corrected Kramers-Kronig technique.

The measured reflectivity spectra and the complex refractive indices of the samples investigated, as obtained from the corrected Kramers-Kronig technique described above, are shown in Figure 3.2. The real and imaginary parts of the complex refractive index of the lowest doped sample obtained from a standard Kramers-Kronig conversion (KK) are also plotted in Figure 3.2 for the sake of comparison. As can be noticed, a significant effect of free carrier concentration on both the real and imaginary part of the complex refractive index is observed at the resonance. Furthermore, the discrepancy between the curves obtained from the corrected Kramers-Kronig technique and those obtained from the standard Kramers-Kronig technique is intensified as the carrier concentration is increased in the sample.

In order to verify the reliability of the corrected Kramers-Kronig technique used in this work to obtain the dielectric properties of the samples investigated, we back calculated the reflectivity spectra using the obtained complex refractive indices of the epilayers and substrates. The back calculated reflectivity spectra of the samples investigated are plotted together with the measured ones. The excellent agreement between the curves demonstrates the reliability of the conversion technique being used.

Finally, it is worth noting that the widely used Lorentz-Drude model offers a simplified description of the complex dielectric function. In that model, random

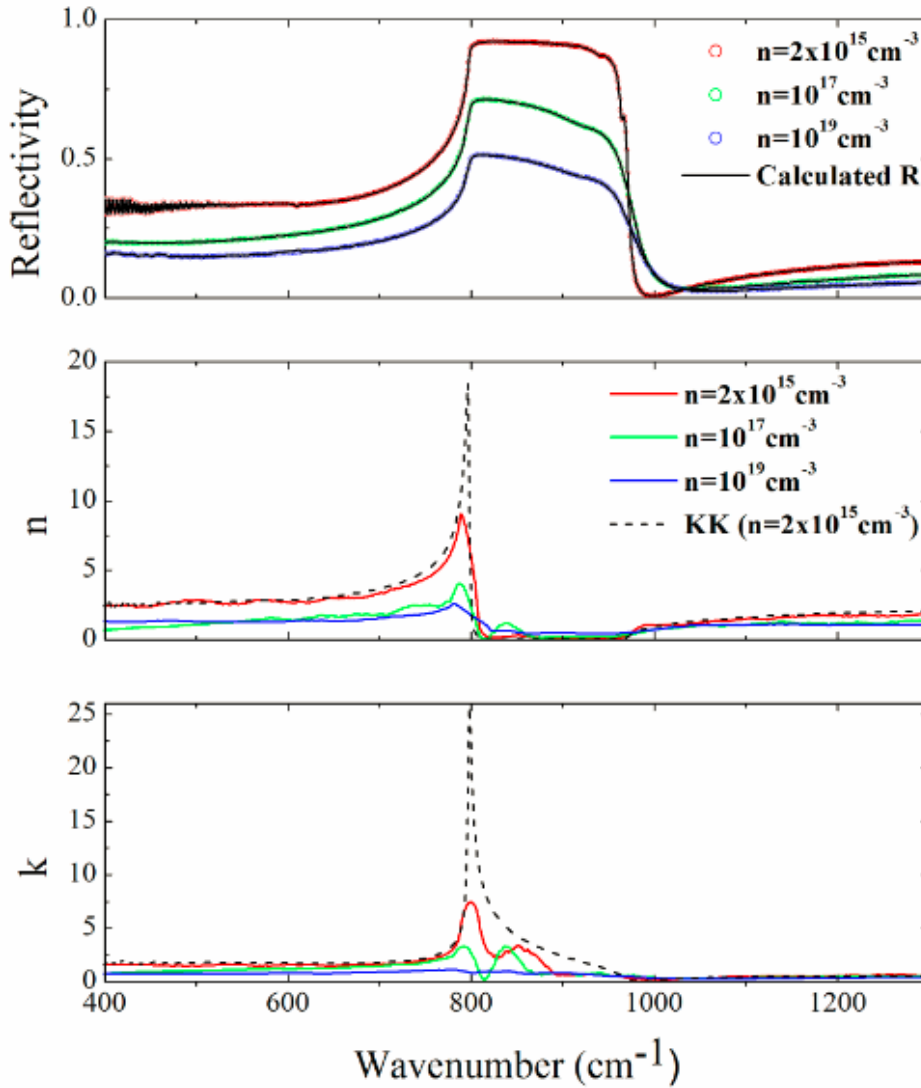


Figure 3.2: Reflectivity spectra and real and imaginary parts of the complex refractive indices of the samples investigated. Solid lines: Real and imaginary parts of the refractive indices obtained by using the Kramers-Kronig technique corrected with reference to Fresnel equations for reflectivity. Dashed lines: Real and imaginary parts of the refractive index of the lowest doped sample obtained by using the conventional Kramers-Kronig conversion technique. The reflectivity spectra are back calculated using the real and imaginary parts of the refractive indices obtained from the corrected Kramers-Kronig technique. The measured reflectivity spectra are plotted with symbols. The back calculated reflectivity spectra are plotted with solid lines.

values are usually taken for the phonon and free carriers damping rates and they assumed to be constant over the entire frequency spectrum. [45] This rather crude simplification is proven to be inaccurate in the literature. [46] Thus, the method used in the present work to deduce the dielectric properties of the samples investigated has the advantage of providing a better description to the material response function, which stands as the primary component in understanding the plasmon-phonon-polariton coupling.

3.3 Results and Discussion

As described earlier, surface and volume PPhP modes result from the interaction and coupling of free carriers collective oscillation modes, zone center optical phonon modes, and incident electromagnetic modes, meaning that their properties depend highly on the characteristics of the zone center optical phonon modes in the material. Therefore, in order to investigate the effect of free carrier concentration on the PPhP modes, it is highly advantageous to understand first their effect on these optical phonon modes.

3.3.1 The effect of plasmon electronic oscillation on the zone center optical phonons

The real (ϵ_1) and imaginary (ϵ_2) parts of the dielectric functions and the energy loss functions $\left(\text{Imag} \left(-1/(\epsilon_1 + i\epsilon_2) \right) \right)$ of the epilayers investigated are shown in Figure 3.3. The frequencies and lifetimes of the zone center transverse optical phonon modes and longitudinal LOPC mixed character modes are the principal determinants of these functions. The peak of the imaginary part of the dielectric function is directly related to the absorption of infrared light by

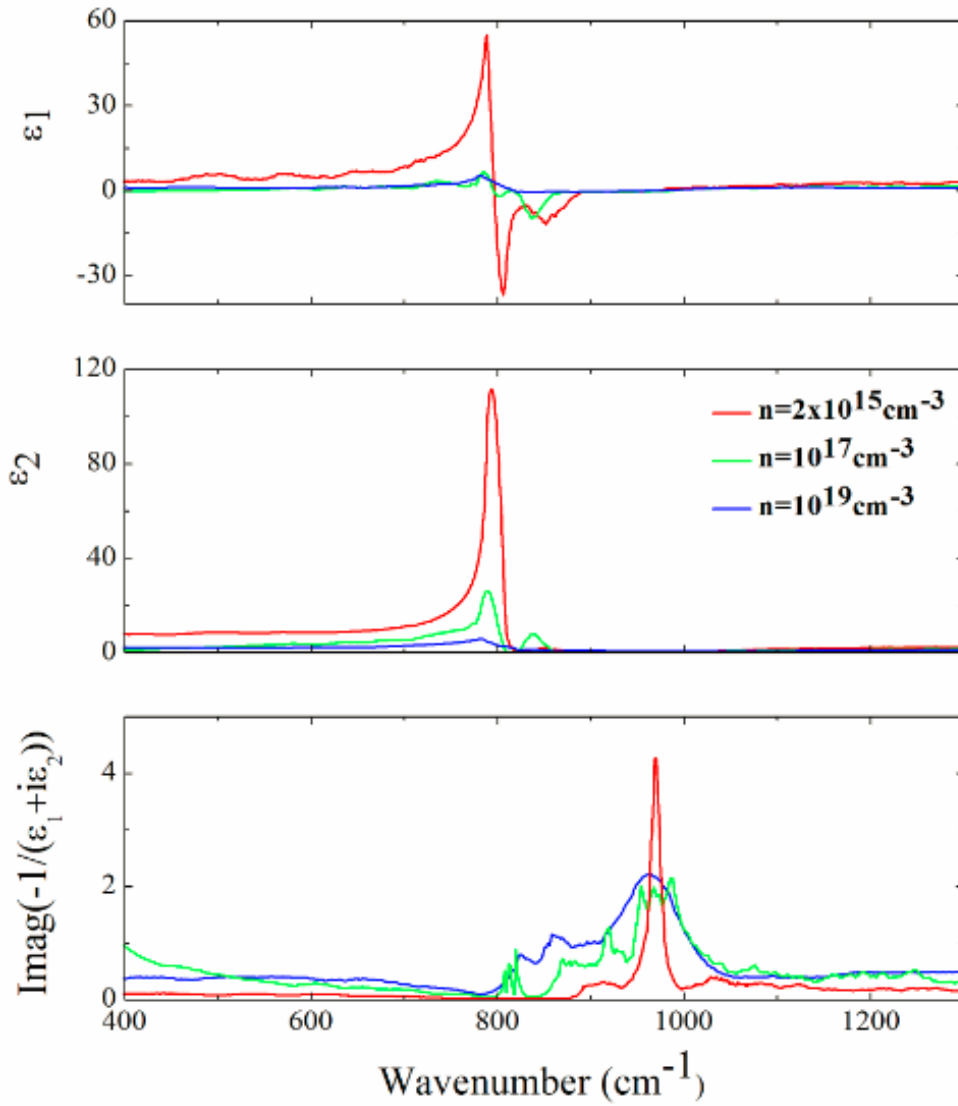


Figure 3.3: The dielectric properties of the samples investigated obtained from the corrected the Kramers-Kronig technique.

transverse optical phonon modes. It occurs at the frequency of the transverse optical phonon and its width is related to the transverse optical phonon lifetime according to Heisenberg uncertainty principle. [47, 48] It can be seen from Figure 3.3 that both the resonance frequency and lifetime of the transverse optical phonon are almost unaffected by the presence of plasmon electronic oscillation

modes in the sample. We found that the lifetime of the zone center transverse optical phonon in the lowest doped sample is 1.40 ps, reduced to 1.23 ps and 1.10 ps as the carrier concentration is increased. The independence of the resonance frequency and lifetime of the transverse optical phonon on free carrier concentration is due to the fact that the transverse optical phonon modes do not couple to plasmon electronic oscillation modes. The small lifetime decay is basically due to optical phonon scattering by point-defects induced by the implantation of the N-ions in the 4H-SiC epilayers.

The peak of the energy loss function of the epilayer is determined by the frequency and lifetime of the LOPC modes in the epilayer. [47, 48] Its position occurs at the resonance frequency of the LOPC mode and its width describes the lifetime of the LOPC mode. Unlike the transverse optical phonon, the lifetime of the LOPC mode is a strong function of carrier concentration. We observe a lifetime of about 2.25 ps in the lowest doped sample, which strongly decays as the carrier concentration is increased. These results are in good agreement with previously observed Raman spectra broadenings in n-type 4H-SiC free standing crystals. [49, 50, 51, 52, 53, 54] The fact that the coupling of the longitudinal optical phonon to the plasmon electronic oscillation is clearly mirrored in the dielectric functions in Figure 3.3 adds a strong support to the reliability of the technique used to deduce the dielectric functions of the samples investigated from reflectivity measurements.

It is worth noting that the LOPC mixed character modes are usually observed in Raman spectra, and their lifetimes are usually estimated from the Raman line shape and position. However, in the case of homoepitaxial multi-layered systems, Raman spectroscopy loses some accuracy as the Raman signal from the substrate superposes to that from the epilayer. In that case, infrared spectroscopy

can be more quantitative than Raman spectroscopy because, the homoepitaxial multi-layered system linear response to an infrared wavelength excitation can be described by a simple theory and the deconvolution of the substrate response and epilayer response can be carried out precisely to yield quantitative results.

3.3.2 Bulk Plasmon–Phonon–Polariton

The observed reduction in the intensity of the reflectivity and dielectric spectra as the free carrier concentration increases is due to the absorptive nature of the plasmon electronic oscillation in the volume of the crystal. Thus, these spectra can be used to see how the plasmon electronic oscillation affects the electromagnetic wave propagating in the volume of an n -doped polar crystal. In other words, these spectra can be used to investigate the PPhP wave in the volume of the crystal as a function of free carrier concentration. The general dispersion relations of such an electromagnetic wave are given by [55]

$$(cq)^2 = \epsilon(\omega)\omega^2, \quad (3.13)$$

where ω and q are the angular frequency and wavevector (oriented parallel to the surface) of the PPhP wave propagating in the crystal, c is the speed of light in vacuum, and $\epsilon(\omega)$ is the complex dielectric function of the crystal under consideration. In order to determine the lifetime of the resultant bulk PPhP, we consider a real wavevector and a complex frequency $\omega = \omega' + i\omega''$ and solve Eq. 3.13 numerically. The function $\omega'(q)$ determines the dispersion of the bulk PPhP, and the inverse of the function $\omega''(q)$ gives the lifetime of each bulk PPhP mode. Thus, the dispersion curves and modes lifetimes have an implicit dependence on the characteristics of the optical phonon modes and plasmon electronic

oscillations modes through $\epsilon(\omega)$.

The computed PPhP dispersion curves and the modes lifetimes in the 4H-SiC epilayers investigated are illustrated in Figure 3.4. We found that the lowest

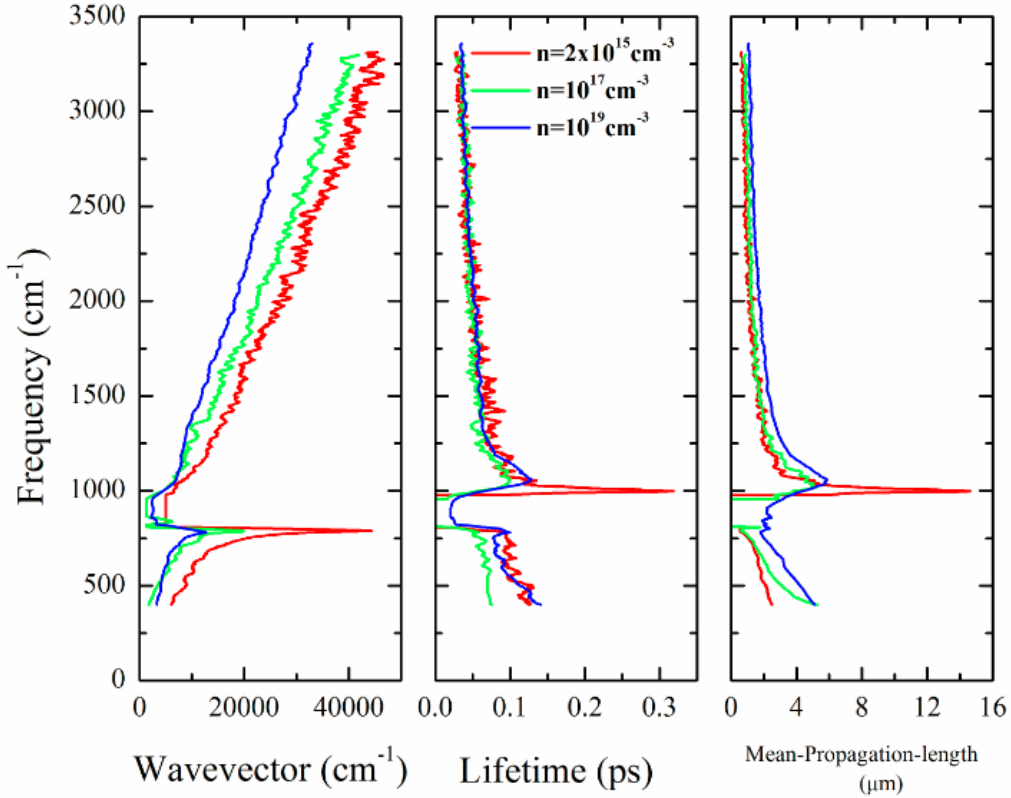


Figure 3.4: Dispersion relations, lifetime, and mean-propagation length of the bulk plasmon-phonon-polariton in the samples investigated.

doped epilayer exhibits a peak lifetime value of 0.3 ps at around 998 cm^{-1} , and the N-implanted samples exhibit a peak lifetime value 70% lower than the lowest doped epilayer at around 1060 cm^{-1} . This demonstrates that the effects of free carrier concentration on the longest living bulk PPhP mode and LOPC mode are similar. In fact, the frequency of the plasmon electronic oscillation mode is directly proportional to the free carrier concentration, and generally exceeds that of the zone center longitudinal optical phonon mode. Hence, when a plasmon

electronic oscillation mode couples with a zone center longitudinal optical phonon mode (due to the macroscopic polarization field associated with both excitations) the resultant LOPC mode frequency broadens (i.e. its lifetime decreases) and shifts towards higher frequencies as the free carrier concentration increases. Thus, these observations clearly demonstrate the strong dependence of the longest living bulk PPhP mode on the free carrier concentration and LOPC mixed character mode frequency.

The mean-propagation-length of the bulk PPhP as a function of free carrier concentration can be determined by considering in Eq. 3.13 a real frequency ω and a complex wavevector $q = q' + iq''$. The inverse of the function $q''(\omega)$ describes the frequency-dependent mean-propagation-length. The curves of the mean-propagation-length in Figure 3.4 show analogous features to those of the lifetime curves. The peak mean-propagation-length value of the PPhP modes in the slightly implanted epilayer is almost 65% smaller than that of the PPhP modes in the un-implanted epilayer. It is worth noting that unlike the lifetime, the mean-propagation-length of the bulk PPhP in the crystal having the highest carrier concentration is slightly larger than that of the bulk PPhP in the two other crystals away from the resonance peak. This is due to the speed at which the bulk PPhP propagates in the crystal. Comparing the slopes of the dispersion curves of the three crystals investigated, we notice that the PPhP modes in the crystal having the highest carrier concentration propagate the fastest, hence having a larger mean-propagation-length. The reason behind this is the fact that the real part of the refractive index decreases as the carrier concentration increases in the sample (see Figure 3.2).

3.3.3 Surface Plasmon–Phonon–Polariton

Let us now use the deduced complex dielectric functions of the three measured crystals to investigate the effect of the carrier concentration on the characteristics of the surface PPhP, which are surface modes created upon coupling between the incident electromagnetic field, the zone center optical phonon modes, and the free carriers collective oscillation modes. After solving Maxwells equations both inside and outside of an isotropic parallelepiped-like crystalline material, and applying proper boundary conditions, one can write the dispersion relations of this surface wave in the form [56]

$$(cq)^2 = \frac{\epsilon(\omega)}{\epsilon(\omega) + 1} \omega^2, \quad (3.14)$$

Likewise to bulk PPhP, solving Eq 3.14 with considering complex ω leads to determining the surface modes lifetimes, and solving Eq. 3.14 with considering complex q leads to determining the mean-propagation-length of the surface modes. The dispersion curves, frequency-dependent lifetime, and frequency-dependent mean-propagation-length of the surface PPhP modes are plotted together in Figure 3.5 for the three measured crystals. The surface modes are excited only in the frequency range where the real part of the complex dielectric function is negative. This range, which is known as the Reststrahlen band, is bounded by the zone center transverse and longitudinal optical modes frequencies. Furthermore, a typical dispersion curve of surface modes presents a frequency gap. This gap is revealed by a discontinuity in the dispersion curve if the damping rates of the LOPC modes are weak, and by a negative slope if the damping rates of the LOPC modes are relatively high.

It can be seen from Figure 3.5 that the free carrier concentration also has a

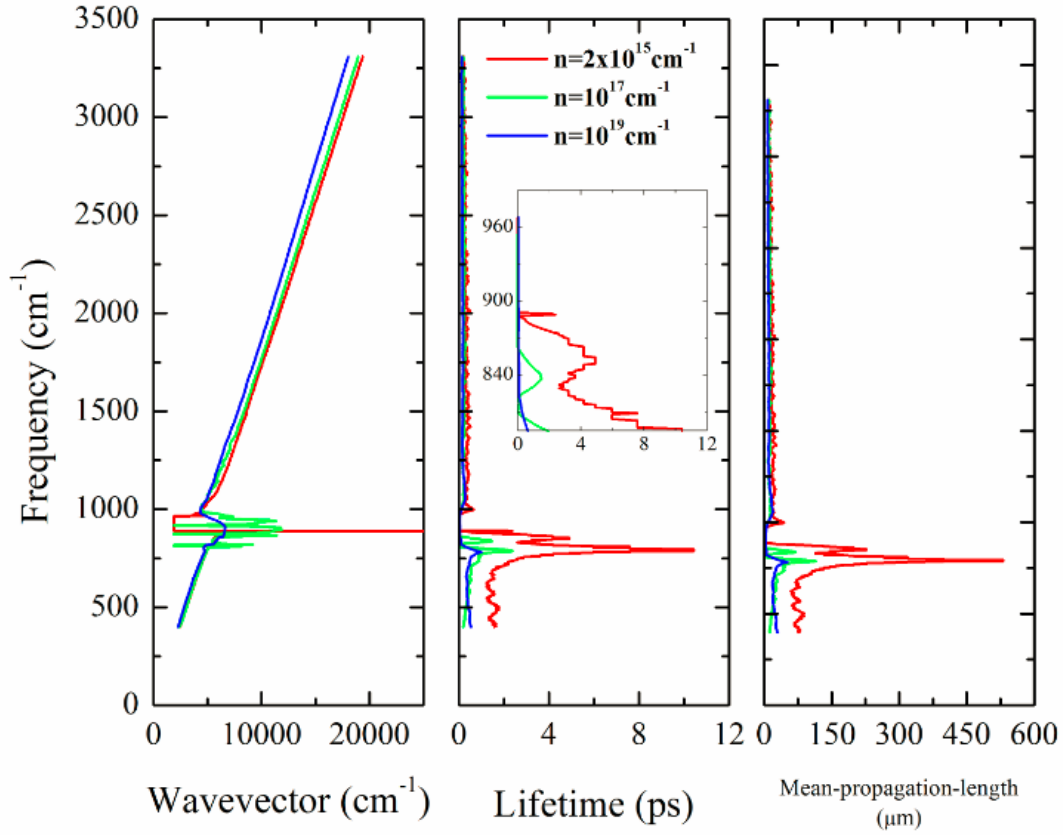


Figure 3.5: Dispersion relations, lifetime, and mean-propagation length of the surface plasmon-phonon-polariton in the samples investigated. Inset: zoom in the region of existence of the surface plasmon-phonon-polariton.

significant effect on the surface PPhP characteristics. However, the effect of free carrier concentration on the surface PPhP is different than that on the bulk PPhP. The lifetime of the longest living surface PPhP mode decreases as the free carrier concentration is increased in the crystal, but the frequency of the longest living surface PPhP mode is independent of the free carrier concentration. Therefore, it appears that the frequency of the longest living surface PPhP depends of the frequency of the zone center transverse optical phonon modes whose frequencies are independent of the free carrier concentration in the volume.

In the lowest doped epilayer, the surface PPhP presents a peak lifetime value

of $4.9ps$ in its range of existence, which is much longer than the lifetime of pure surface plasmon modes, reaching up to 500 fs in their prime conditions, as reported by Woessner et al. [57] The surface PPhP lifetime is dropped by almost 98% as the free carrier concentration is increased, taking a value of $0.1ps$ for the epilayer in which the carrier concentration is about $10^{19}cm^{-1}$. Furthermore, examining the dispersion relation curves, we can notice that these waves propagate on the surface with a speed that is weakly affected by the free carrier concentration. For that reason, the plots of mean-propagation-length show the same dependence on free carrier concentration as those of the lifetime. Accordingly, the surface PPhP waves propagating on the surface of the lowest doped sample show a peak mean-propagation-length value of $227.6\mu m$, which is dropped by almost 98% as the free carrier concentration is increased, taking the value of $4.8\mu m$.

3.3.4 Comparison between bulk and surface plasmon-phonon-polariton modes

Comparing the results obtained for bulk and surface PPhP, we see that the lifetimes and mean-propagation-lengths of the surface PPhP modes are much longer than those of the bulk PPhP modes. Moreover, the surface PPhP waves travel at a faster rate than the bulk PPhP waves. In Figure 3.6 we plot the dispersion curves of both bulk and surface PPhP in the lowest doped sample to illustrate the difference in group velocities of these two waves. The bulk PPhP modes travel about 2.4 times slower than their surface counterparts, which is in agreement with the value of the real part of the refractive index obtained by the corrected Kramers-Kronig technique (see Figure 3.2, $Re(N) \simeq 2.4$ away from resonance). However, the lifetimes of the surface PPhP modes are a stronger

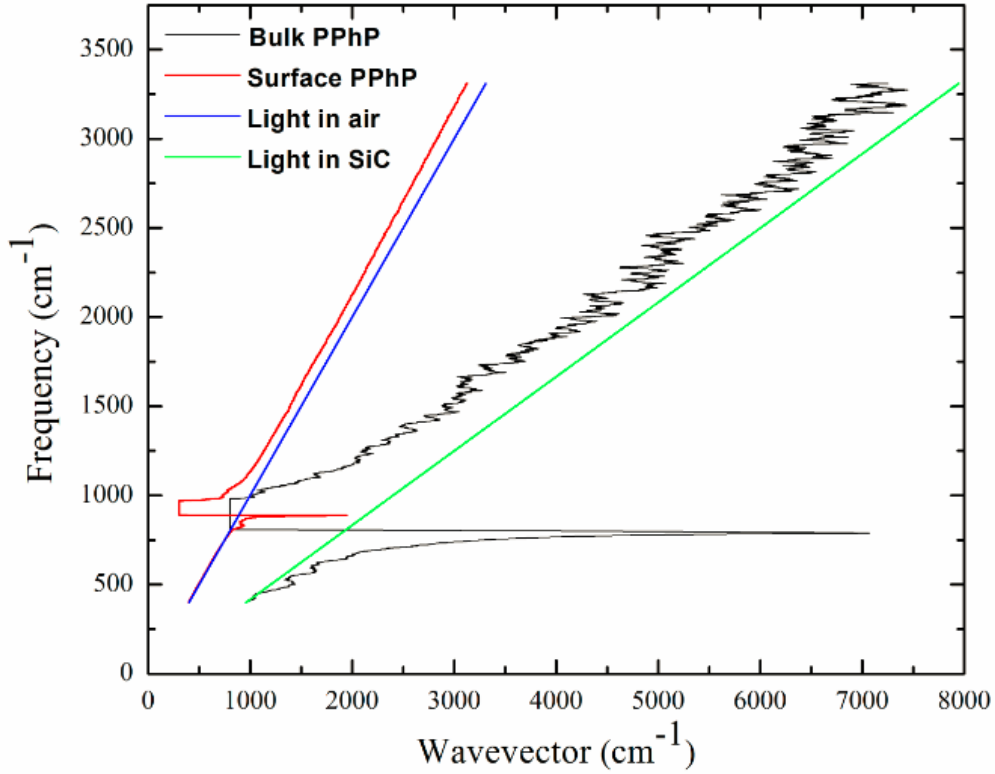


Figure 3.6: Comparison between the surface plasmon-phonon-polariton (blue line) and bulk plasmon-phonon-polariton (red line) in the lowest doped 4H-SiC epilayer. The light lines in air (black) and in 4H-SiC (green) are also plotted.

function of carrier concentration. As mentioned earlier, the surface PPhP modes lifetime exhibit about 98% decay while bulk PPhP exhibit only about 70% decay as the free carrier concentration is increased. This can be understood if we realize that, unlike volume plasmon modes, surface plasmon modes also possess transverse electric field components. This makes the PPhP coupling on the surface stronger than that in the volume, and consequently enhance the damping rate of the surface PPhP over that of the bulk PPhP.

3.3.5 Temporal coherence of the surface plasmon-phonon polariton modes

In the last couple of decades, surface phonon-polariton have captured remarkable interests because they showed unanticipated behavior. [21, 31] It was demonstrated that the energy density of these waves is almost monochromatic. They also appear to have a long coherence time and a special coherence over distances much longer than their wavelengths. Therefore, it would be of particular interest to use the results presented above to draw a conclusion in respect of the effect of the free carrier concentration on the coherence of the surface plasmon-phonon-polariton waves. The width of the light spectrum is a measure of the temporal coherence of the emitting source. However, the width of the light spectrum is directly proportional to the width of the modes lifetimes spectrum. Hence, the width of the surface PPhP lifetime peak that occurs in the Reststrahlen band (the region of existence of the surface phonon modes) is also a measure of temporal coherence of the surface PPhP. In the lowest doped crystal, the coherence time of the longest living mode takes the value of $0.75ps$ (according to Heisenberg uncertainty principle), but the increase in the free carrier concentration leads to unanticipated results. As shown in Figure 3.5, as the carrier concentration is raised to $10^{17}cm^{-3}$, the coherence time is increased by 125% (narrower bandwidth) taking the value of $1.67ps$. Raising the free carrier concentration to $10^{19}cm^{-3}$, however, leads to an extremely high decay rate of surface PPhP modes, so that the surface PPhP modes barely survive in such a highly doped crystal and their coherence becomes undetectable. These results suggest the following. The surface plasmon modes, similarly to the surface phonon-polariton modes, have some degree of temporal coherence. Thus, although the coupling of the free

carrier collective oscillation modes with the longitudinal optical phonon modes has a negative impact on the lifetime of the resultant surface PPhP modes, it can considerably enhance the temporal coherence of these resultant surface wave modes. Consequently, surface PPhP modes can be employed for the development of highly temporal coherent thermal sources, either completely new or through doping of existing ones.

3.4 Conclusion

In summary, we have investigated in this chapter the dependence of the dispersion relations, lifetime, mean-propagation-length, and temporal coherence of the surface plasmon-phonon-polariton modes on the free carrier concentration in 4H-SiC. Fourier transform of p -polarized reflectivity spectra averaged over a wide incidence angle range were collected from 4H-SiC epilayers of different carrier concentrations and used to precisely deduce the complex dielectric properties of the measured samples. The analysis of the measured reflectivity spectra consists in first deducing the complex dielectric functions of the measured samples using Kramers-Kronig conversion method, then correcting the effects of the substrate response and artificial extrapolation of the measured reflectivity to zero and infinity using a numerical technique involving Fresnel equations for reflectivity from a multilayer system. We have found that, when the free carrier concentration is low in the sample, the lifetimes of the surface plasmon-phonon-polariton modes exceed by an order of magnitude the lifetimes of pure surface plasmon modes. However, they decrease rapidly as the free carrier concentration is increased in the sample. We have also shown that the coupling between the free carriers collective oscillation, the zone center longitudinal optical phonon, and an inci-

dent electromagnetic wave leads to a highly temporal coherent surface plasmon-phonon-polariton wave. It is found that the temporal coherence of that resultant surface wave can be further enhanced by increasing the free carrier concentration in the sample. We believe that the outcomes of this work may open horizons in the field of nanophotonics where plasmon-phonon-polariton modes will be used as the main actors for controlling and manipulating light in the nanoscale regime.

Chapter 4

AlN– Based Tunable Near– Field Infrared Sources

The coupling of electromagnetic wave carrying energy with elementary excitations in a material is the primary approach of confining and guiding light in subdiffraction dimensions. A form of light-matter interaction that has attracted a great deal of scientific interest over the last couple of decades is the surface-plasmon-polariton (SPP). It results from the coupling of photons with collective electronic oscillations at the surface of metallic structures. [58, 59, 60, 61] The discovery of the SPP modes laid the foundations for the fields of nanophotonics and metamaterials.[62] Nevertheless, optical losses due to plasmon waves scattering significantly reduce the lifetime of SPP modes, limiting the performance of metals surfaces as carriers of electromagnetic energy in low dimensions.[27, 28, 63, 64, 65] Therefore, the search for alternative methods of light confinement is of crucial importance for the advancement of nanophotonics applications.

In polar materials, the frequency of the transverse (ω_{TO}) and the frequency of the longitudinal (ω_{LO}) zone center optical phonon modes are not equal. [66] The

presence of a macroscopic field in these materials alters the electrostatic restoring forces experienced by the transverse and longitudinal modes, hence raising the frequency of the longitudinal mode over that of the transverse mode. [67] The frequency range bounded by ω_{TO} and ω_{LO} is known as the Reststrahlen band. In this frequency range, the real part of the material response to an electromagnetic excitation is negative, and plane waves acquire an evanescent character giving rise to highly localized electromagnetic modes at the surface of the material known as Surface Phonon Polaritons (SPhP). [26, 68] Relevant research works suggested that the lifetime of SPhP reaching up to time-scales of picoseconds is orders of magnitude larger than that of surface plasmon.[31] This makes SPhP more efficient in confining electromagnetic energy at the surfaces of materials.

Tuning the SPhP modes is indeed of great importance for the development of nanophotonic devices. These surface waves demonstrated to have some degree of temporal and spatial coherence as well as a high energy density in a narrow spectral range, and can be radiated by introducing a grating on the surface of the sample. Hence, controlling the spectral region of existence of SPhP modes can lead to the emission of monochromatic waves of high intensity at desired frequencies. In the previous chapter, we have demonstrated that varying the carrier concentration inside a material plays a significant role in tuning the lifetime and the temporal coherence of SPhP waves. [69] However its ability to tune the frequencies at which SPhP modes are allowed to exist on the sample surface is somewhat limited.

In most cases, phonon-related properties and materials dielectric function, which determines the materials response to electromagnetic infrared excitations, shows strong dependence on the surface orientation.[45, 47, 70, 71] Hence, by varying the crystal surface orientation, the frequencies of the transverse and lon-

gitudinal optical phonons change, modifying the dielectric function and shifting the Reststrahlen band, i.e. shifting the region of existence of the SPhP modes. A mere change in the symmetry direction can be used as a mechanism for tuning the frequencies at which electromagnetic energy can be carried in the form of SPhP modes. In this work, we demonstrate that self-nucleated single crystals can be grown with several differently oriented facets supporting SPhP modes of completely different characteristics. Hence, the SPhP properties can be tuned on these crystals by selecting the crystal facet supporting the SPhP modes having the desired characteristics. In other words, we demonstrate that these crystals can be used to tune the properties of the SPhP modes over a wide spectral range.

The excitation of optical phonons is essential for the existence of SPhP modes in a material, and the relaxation time of the excited optical phonon is essential for the survival of SPhP modes. Therefore, we first examine the effect of surface orientation on the harmonicity and anharmonicity of optical phonons, from which we deduce the dependence of the properties of SPhP waves on the crystal surface orientation. We base our investigation on one-dimensional lattice dynamics models and on the analysis of reflectivity spectra using Kramers-Kronig conversion integrals corrected with reference to Fresnel equations for reflectivity.[43, 69]

The material being used in this work is wurtzite AlN. The choice of wurtzite AlN is beneficial due to the availability of processes for preparing self-nucleated wurtzite AlN single crystals exhibiting well-developed facets of different orientations, and because AlN is known for having high acoustic phonon group velocity, hence low optical phonon decay rates, [72, 73, 2] which may result in SPhP of high group velocity and long lifetime. However, we believe that the fundamental physics outlined in this paper is applicable for all polar semiconductor materials crystallizing in anisotropic structures.

4.1 Experiments

The self-nucleated AlN single crystal investigated in this work was collected on the crucible wall of a sublimation reactor.[74] It was grown with minimal contact with the crucible wall or other crystals. Therefore, it exhibits natural growth habit of AlN with many well-developed facets. It measures $7.5 \times 7.5 \times 5.5 \text{mm}^2$ on the sides. The crystallographic orientations of the observed facets were determined using X-Ray texture measurements. These measurements indicated that the observed facets belong to the $\{10 - 10\}$ $\{10 - 12\}$ $\{10 - 13\}$ $\{10 - 14\}$ and $\{0001\}$ crystallographic classes.

The X-Ray texture measurements were carried out by using an X-Ray diffractometer comprising a cradle having approximately $37 \times 44 \times 34 \text{cm}^3$ ($W \times H \times D$)-like dimensions and five motorized movements: phi rotation (φ), psi tilt (ψ), and x - y - z manipulation. The measurements were therefore taken at a fixed 2-theta value and two movements realized the facet orientation measurement: the phi rotation axis, which is around the surface normal, and the psi rotation axis, which lies in the surface and in the diffraction plane.

Unpolarized infrared reflectivity spectra were taken from well-developed facets of different orientations. The focusing of the incident light and the collection of the reflected light was made by means of a confocal microscope. A DTGS detector and a KBr beamsplitter were used, and spectra were recorded in the $600 - 3500 \text{cm}^{-1}$ frequency range. The reflectivity from each measured facet was compared to the reflectivity from a gold-coated mirror, and the reproducibility of the measurements was checked by measuring each spectrum twice. The two recorded data from each facet were identical within the experimental error, i.e., within 1% reflectivity.

4.2 Results and Discussion

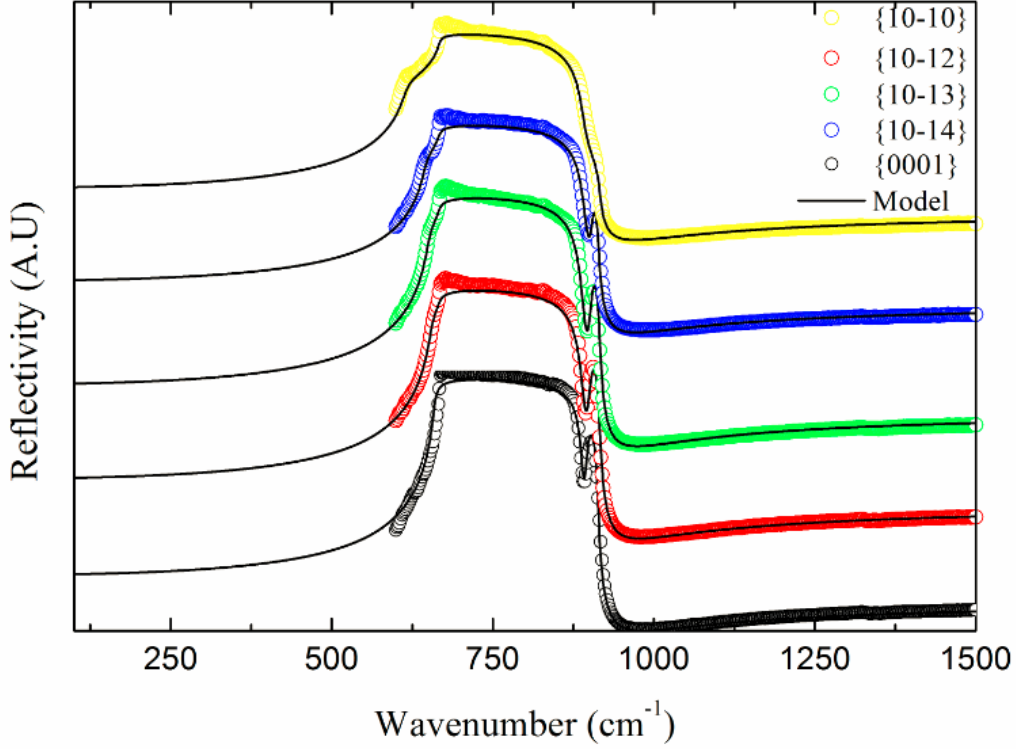


Figure 4.1: Reflectivity spectra from the measured facets. Symbols: Experimental measurements. Solid lines: Model.

Measurements of reflectivity spectra from facets belonging to different crystallographic classes are shown in Figure 4.1 by symbols. A clear variation in the shape of the reflectivity spectrum can be noticed as the surface orientation is changed. A peak around 900 cm^{-1} slowly disappears and a hump around 610 cm^{-1} starts to appear as the normal to the surface deviates from the crystal optical axis (or the c -axis). These observations suggest that the AlN complex dielectric function, which is the principal determinant of the SPhP, is a strong function of surface orientation. In order to determine the dependence of the complex dielectric function on the surface orientation, a model for reflectivity of unpolarized infrared light is vitally important.

4.2.1 A General Model for Infrared Reflectivity

Using the linear diatomic chain model for a binary semiconductor with Maxwell's equations, we can express the complex dielectric function of the lattice as [75]

$$\epsilon_{lat}(\omega) = (n + ik)^2 = \epsilon_{\infty} + \frac{S\omega_{TO}^2}{\omega_{TO}^2 - \omega^2 - i\Gamma\omega} \quad (4.1)$$

where n and k are the refraction index and extinction coefficient, respectively, ω is the frequency of the applied electric field, and Γ is the strength of the frictional term that describes the damping of the excited optical phonon. The constant ϵ_{infy} is the high frequency limit of the lattice dielectric function and S is the oscillator strength having the form $S = \epsilon_0 - \epsilon_{\infty}$, being the low frequency limit of the lattice dielectric function given by the generalized Lydanne-Sachs-Teller equation,

$$\epsilon_0 = \epsilon_{\infty} \frac{\omega_{LO}^2 + \frac{\Gamma^2}{4}}{\omega_{TO}^2 + \frac{\Gamma^2}{4}}. \quad (4.2)$$

However, the AlN wurtzite structure has the C_{6v}^4 symmetry with four atoms per unit cell, leading to two pure infrared active phonon branches. A branch corresponding to phonon polarization along the c-axis (known as the A_1 symmetry branch) and a branch corresponding to phonon polarization in the isotropic basal plane (known as the E_1 symmetry branch).[48, 54, 76, 77, 78] The anisotropy of the force constants in this structure makes the energies of the phonon modes of A_1 symmetry different from the energies of the phonon modes of E_1 symmetry. This has the consequence that the dielectric function parallel to the c-axis is different from the dielectric function perpendicular to the c-axis. It follows that the dielectric function parallel (ϵ_{\parallel}) and perpendicular (ϵ_{\perp}) to the normal of a surface of random orientation are certainly different. We express these dielectric

functions as

$$\epsilon_{\parallel} = \epsilon_{\infty\parallel} + \frac{S_{\parallel}\omega_{TO\parallel}^2}{\omega_{TO\parallel}^2 - \omega^2 - i\Gamma_{\parallel}\omega} \quad (4.3)$$

and

$$\epsilon_{\perp} = \epsilon_{\infty\perp} + \frac{S_{\perp}\omega_{TO\perp}^2}{\omega_{TO\perp}^2 - \omega^2 - i\Gamma_{\perp}\omega} \quad (4.4)$$

where $\omega_{TO\parallel(\perp)}$ is the frequency of the transverse phonon mode parallel (perpendicular) to the surface normal. If the surface is randomly oriented, the excited transverse and longitudinal phonons are of mixed E_1 and A_1 symmetry. Their frequencies can be obtained from the knowledge of the frequencies of the pure symmetry phonons (A_1 and E_1 symmetry phonons) according to the generalized Loudon equations [79]

$$\omega_{TO(LO)\parallel}^2 = \omega_{TO(LO)A}^2 \cos^2(\theta' - \theta) + \omega_{TO(LO)E}^2 \sin^2(\theta' - \theta) \quad (4.5)$$

and

$$\omega_{TO(LO)\perp}^2 = \omega_{TO(LO)A}^2 \sin^2(\theta' - \theta) + \omega_{TO(LO)E}^2 \cos^2(\theta' - \theta) \quad (4.6)$$

where $\omega_{TO(LO)A}$ is the frequency of the transverse (longitudinal) optical phonon in the direction of the c -axis, $\omega_{TO(LO)E}$ is the frequency of the transverse (longitudinal) optical phonon in the isotopic basal plane, and θ' is the angle between the c -axis and the normal to the surface. If the light is incident with a nonzero angle of incidence θ , the dielectric function becomes a combination of ϵ_{\parallel} and ϵ_{\perp} given by[45]

$$\epsilon(\omega, \theta) = \frac{\epsilon_{\perp}(\omega)\epsilon_{\parallel}(\omega)}{\epsilon_{\perp}(\omega)\sin^2(\theta) + \epsilon_{\parallel}(\omega)\cos^2(\theta)} \quad (4.7)$$

On the other hand, the Fresnel coefficient of reflectivity $r = E_r/E_i$ is defined as the ratio of the reflected electric field to incident electric field. Since the applied

electric field is unpolarized, we can consider that it is the sum of a field component parallel to the plane of incidence (E_p) and a field component perpendicular to the plane of incidence (E_s). We define $E_{i,p} = E_i \cos \varphi$ as the projection of the incident electric field parallel to the plane of incidence, and $E_{r,p} = E_r \cos \chi$ as the projection of the reflected electric field parallel to the plane of incidence, where $\varphi(\chi)$ is the angle between the plane of incidence and the incident (reflected) electric field. The projections of the incident and reflected electric fields perpendicular to the plane of incidence will thus be given by $E_{i,s} = E_i \sin \varphi$ and $E_{r,s} = E_r \sin \chi$. Evaluating the complex conjugate of the Fresnel coefficient of reflectivity and making use of all the projections introduced earlier, we end up with the following expression for the total reflectivity

$$R = rr^* = R_p \frac{\cos^2 \varphi}{\cos^2 \chi} = R_s \frac{\sin^2 \varphi}{\sin^2 \chi}. \quad (4.8)$$

Using Eq. 4.8 we can express the angle χ as a function of φ as $\chi = \tan^{-1} (\sqrt{R_s/R_p} \tan \varphi)$. Applying the trigonometric property $\cos(\tan^{-1} x) = 1/\sqrt{1+x^2}$ and substituting the expression for χ in Eq 4.8, we can write the total reflectivity as a function of only φ in the form

$$R = R_p \cos^2 \varphi + R_s \sin^2 \varphi. \quad (4.9)$$

Since a microscope objective was used in the measurements to focus the incident light and collect the reflected light, the recorded spectra represent average reflectivity spectra over the set of all angles less than the objective angular aperture. The measured reflectivity should thus satisfy the equation

$$R = \frac{1}{\alpha_0} \int_0^{\alpha_0} (R_p \cos^2 \varphi + R_s \sin^2 \varphi) d\theta, \quad (4.10)$$

where α_0 is the one-half angular aperture of the microscope objective.

The infrared reflectivity is determined by the infrared dielectric response of the crystal (Eqs. 4.3, 4.4 and 4.7). Because the basal plane of the wurtzite structure is isotropic, we can always consider that the c -axis lies in the plane of incidence. It follows that the component of the electric field parallel to the plane of incidence $E_{i,p}$ interacts with optical phonons of mixed E_1 and A_1 symmetry, and thus the partial reflectivity R_p results from the angle-dependent dielectric function described in Eq. 4.7. The component of the electric field perpendicular to the plane of incidence $E_{i,s}$ is thus always perpendicular to the c -axis and interacts with pure E_1 symmetry optical phonons. Consequently, the partial reflectivity R_s results from the dielectric function ϵ_E whose parameters are determined by the harmonicity and anharmonicity of zone center optical phonon of pure E_1 symmetry. Therefore, the partial reflectivity components R_p and R_s can be written in terms of the dielectric functions expressed in Eqs. 4.3, 4.4 and 4.7 as

$$R_p = \left| \frac{\sqrt{\epsilon(\omega, \theta)} - 1}{\sqrt{\epsilon(\omega, \theta)} + 1} \right|^2, \quad (4.11)$$

and

$$R_s = \left| \frac{\sqrt{\epsilon_E(\omega)} - 1}{\sqrt{\epsilon_E(\omega)} + 1} \right|^2. \quad (4.12)$$

In what follows we determine the parameters of $\epsilon(\omega, \theta)$ and $\epsilon_E(\omega)$ as a function of the crystal surface orientation. Then, we retrieve $\epsilon(\omega, \theta)$ and $\epsilon_E(\omega)$ of the measured facets by fitting the reflectivity model outlined above to the reflectivity measurements. Finally, from the knowledge of $\epsilon(\omega, \theta)$, we compute the characteristics of SPhP on each facet.

4.2.2 Determination of the Harmonicity Parameters in the Expressions of the Dielectric Functions

Assuming that the total potential energy of the crystal is the sum of interatomic potentials, and considering nearest neighbor interactions, the potential energy acquires a minimum at a given equilibrium point x_0 . Then, expanding the potential energy around x_0 in a Taylor series up to the quadratic term and neglecting higher order terms, we obtain an expression for the total potential energy within the harmonic approximation. The second derivative of the harmonic potential evaluated at x_0 represents the harmonic interatomic force constants. However, in polar materials such as AlN, the interatomic forces are accompanied by long-range electrostatic forces due to the presence of a macroscopic electric field in the crystal. Therefore, the expression of the potential energy must include a term describing the long-range Coulomb interaction. The total potential energy takes thus the form

$$U_{ij} = \frac{e_i e_j}{x} + U_{harm}(x). \quad (4.13)$$

On the right hand side of Eq. 4.13, the second term represents the interatomic potential, while the first term represents the Coulomb interaction potential, with e_i and e_j being the charges of different atoms. The indices i and j in Eq. 4.13 run over all the atoms of the crystal. Evaluating the second derivative of the potential energy expressed in Eq. 4.13 at equilibrium provides an additional term representing the force constant due to long-range Coulomb interactions. Since the Coulomb force is long ranged, describing an interaction with all the atoms of the crystal, we can reasonably assume that the additional contribution of the Coulomb interactions to the force constant is a constant value (σ) at all

the points of the crystal.

In order to derive expressions determining the harmonicity parameters in the dielectric functions of AlN, we consider a diatomic linear chain with two different masses and two different spring constants. Let M_1 and M_2 be the masses of the aluminum ion and nitrogen ion, respectively, $K = \alpha + \sigma$ the force constant between two identical ions in adjacent unit cells, and $G = \beta + \sigma$ the force constant between different ions in the same unit cell. Here, α and β are the harmonic short-range interatomic force constants. Considering the expressions of the force constants K and G in a linear diatomic chain model and solving for the eigenfrequency of the longitudinal zone center optical phonon, we find

$$\omega_{LO}^2 = \frac{\alpha + \beta + 2\sigma}{\mu}. \quad (4.14)$$

The macroscopic electric field inside the crystal raises the frequency of the longitudinal phonon mode over that of the transverse phonon mode at the center of the Brillouin zone. The local longitudinal and transverse components of the electric field can be approximated by [67]

$$E_L^{local} = -\frac{8\pi P}{3} \quad (4.15)$$

and

$$E_T^{local} = \frac{4\pi P}{3} \quad (4.16)$$

where P is the polarization density. Since the Coulomb force constant σ is the result of the presence of the long-range electrostatic force, the difference between the local longitudinal and transverse components of the electric field should mirror the difference between the force constant of the transverse mode and that of the

longitudinal mode. Equating the relative difference of the two local electric fields to the relative difference of the transverse and longitudinal zone center optical phonon frequencies, we find

$$\omega_{TO}^2 = \frac{\alpha + \beta - \sigma}{\mu}. \quad (4.17)$$

We thus end up with expressions determining the harmonic parameters in the dielectric functions of AlN in terms of the harmonic force constants.

4.2.3 Determination of the Anharmonicity Parameters in the Expressions of the Dielectric Functions

The harmonic approximation gives the picture of only non-interacting phonon modes in a crystal. In order to describe the anharmonicity of the lattice modes, one should go beyond the quadratic term in the Taylor series expansion of the potential energy.[80] The rate at which optical phonon decays into other phonons of lower energy (which is defined as the inverse of the lifetime of the optical phonon mode) can be calculated by considering the terms higher than the quadratic term in the Taylor series expansion of the potential energy as perturbations to the harmonic Hamiltonian. The decay rate of the excited zone center optical phonon determines the damping parameter (Γ) in the expressions of the dielectric functions.

At the center of the Brillouin zone, optical phonons have a near-zero wavevector ($q \approx 0$). Lets consider that the frequency of the zone center optical phonon under consideration is ω_0 . At moderate temperatures, the zone center optical phonon decays into two acoustic phonons of wavevectors q' and q'' and energies ω' and ω'' due to the anharmonic cubic term of the potential energy. Conser-

variation of energy requires that $\omega_0 = \omega' + \omega''$. Near the center of the Brillouin zone, the Umklapp processes should be unlikely, and thus the momentum should remain conserved. It follows that $q = q' + q''$. Furthermore, due the fact that the dynamical matrix satisfies the symmetry of an even function, the created acoustic phonons will likely have equal momenta with opposite directions $q' = -q''$ and energies of equal magnitudes $\omega' = \omega'' = \omega_0/2$. Using first order perturbation theory, Klemens derived the following expression for the rate at which optical phonon decays into two acoustic phonons[72, 73, 2]

$$\Gamma = \frac{2.5\gamma^2}{\pi} \frac{\hbar\omega_0^2}{\mu v^2} \left(1 + 2n\left(\frac{\omega_0}{2}\right) \right), \quad (4.18)$$

where γ is the Grüneisen parameter, v is the acoustic phonon group velocity near the zone center, and n is the Bose-Einstein equilibrium distribution function. However, in the derivation of the phonon decay rate, one should take into account that the anharmonicity of the lattice imposes a strain field on the acoustic phonon mode q' modifying its energy. This induced strain, being a mechanical effect, should affect the force constants α and β but not σ . Therefore, we write the modified short-range interatomic harmonic force constants as

$$\alpha' = \alpha(1 + 2\gamma\eta) \quad (4.19)$$

and

$$\beta' = \beta(1 + 2\gamma\eta) \quad (4.20)$$

where η denotes the induced strain. The change in energy due to the presence of the strain alters the phonon damping function given by Eq. 4.18. Substituting Eqs. 4.19 and 4.20 in the expression giving the eigenfrequency of the zone center

transverse optical phonon (Eq. 4.17), we obtain the ratio

$$\frac{\delta\omega'^2}{\omega'^2} = \frac{2}{\sqrt{3}} \left(\frac{\alpha - \beta}{\alpha + \beta - \sigma} \right) \gamma\eta. \quad (4.21)$$

The strain reduces the optical phonon decay rate in Eq. 4.18 by the square of the coefficient of the strain in Eq. 4.21. [72, 73, 2]

The possible channels for the decay of a zone center optical phonon can be deduced by looking at the detailed phonon dispersion curves of wurtzite AlN. [80, 81] The acoustic phonons that satisfy the condition $\omega' = \omega_0/2$ are the longitudinal and transverse acoustic phonon branches along the $\Gamma - K$ direction, and the longitudinal branch along the $\Gamma - M$ direction. Each channel has its own decay function given by Eq. 4.18. Therefore, the total rate at which the optical phonon decays can be written as the sum of four equiprobable decay channels as

$$\Gamma = \frac{2.5}{\pi} \frac{\hbar\omega_0^2}{\mu} \left[\begin{aligned} & \times \left[\left(\frac{\gamma_L^K}{v_L^K} \right)^2 + \left(\frac{\gamma_{T_1}^K}{v_{T_1}^K} \right)^2 + \left(\frac{\gamma_{T_2}^K}{v_{T_2}^K} \right)^2 + \left(\frac{\gamma_L^M}{v_L^M} \right)^2 \right] \\ & \times \left[\frac{4}{3} \left(\frac{\alpha - \beta}{\alpha + \beta - \sigma} \right)^2 \right] \\ & \times \left(1 + 2n \left(\frac{\omega_0}{2} \right) \right) \end{aligned} \right], \quad (4.22)$$

where the subscripts indicate the phonon branch polarization and the superscripts K and M indicate the crystallographic directions $\Gamma - K$ and $\Gamma - M$. In order to determine the transverse and longitudinal acoustic phonon group velocities involved in the expression of the rate at which the optical phonon decays, we assume linear dispersion relations for the acoustic branches and solve Green-Christoffel equation $\rho\omega^2 u_\alpha = \sum_\beta \sum_{\gamma,\lambda} C_{\alpha\gamma\beta\lambda} q_\gamma q_\lambda u_\beta$. [82, 83] In Green-Christoffel equation ρ is the material density, $\alpha, \beta, \gamma,$ and λ are Cartesian coordinates, $C_{\alpha\gamma\beta\lambda}$ are the elements of the (6×6) elasticity matrix, u is the displacement vector and

q is a unit vector parallel to the $\Gamma - K$ or $\Gamma - M$ direction. We note here that such linearized dispersion relations give accurate description of the acoustic phonon group velocity near the center of the Brillouin zone.

	$v_L(m/s)$	γ_L	$v_L(m/s)$	γ_{T1}	$v_{T2}(m/s)$	γ_{T2}
$\Gamma - K$	11223	0.8099	6332	0.8306	6197	0.8311
$\Gamma - M$	11223	0.8099	-	-	-	-

Table 4.1: Calculated phonon group velocities and Grüneisen parameters in ΓK and ΓM directions.

In order to determine the acoustic phonon mode Grüneisen parameters involved in the expression of the rate at which the optical phonon decays, we consider the crystal as a continuum medium and adopt the calculation method described in Ref. [83]. In table 4.1, we present the obtained acoustic phonon group velocities and Grüneisen parameters in the crystallographic directions $\Gamma - K$ and $\Gamma - M$. It can be clearly noticed from Eq. 4.22 that the anharmonic parameters of the dielectric functions can be expressed, like the harmonic parameters, in terms of the harmonic force constants.

4.2.4 Determination of the dielectric functions for ' p ' and ' s ' polarizations by fitting the model for reflectivity to the measured reflectivity spectra

After having expressed the harmonic and anharmonic parameters in the expressions of the dielectric functions in terms of the harmonic force constants, we present in this subsection the procedure we followed to retrieve the dielectric functions of the measured facets for ' p ' and ' s ' polarizations.

As mentioned above, the reflectivity measurements were carried out on facets

belonging to the $\{10 - 10\}\{10 - 12\}\{10 - 13\}\{10 - 14\}$ and $\{0001\}$ crystallographic classes developed on of a self-nucleated wurtzite AlN single crystal. First, Kramers-Kronig conversion of reflectivity spectra taken from facets belonging to the $\{0001\}$ and $\{10 - 10\}$ crystallographic classes was carried out (with the appropriate care to account for the error that may arise from integration over a finite frequency range [69]) to retrieve the effective normal incidence dielectric functions determined by the zone center optical phonons of pure E_1 symmetry and pure A_1 symmetry. This allowed us to obtain the frequencies of the zone center optical phonons of pure E_1 and A_1 symmetry as well as the static and high frequency dielectric constants (ϵ_0) and ϵ_∞) along the c-axis and in the basal isotropic basal plane. The maxima of the imaginary parts of the obtained dielectric functions indicated that the frequency of the zone center transverse optical phonon of E_1 symmetry is $\omega_{TE} = 667 \text{ cm}^{-1}$ and that of the zone center transverse optical phonon of A_1 symmetry is $\omega_{TA} = 612 \text{ cm}^{-1}$. The maxima of the energy loss functions ($Im(-1/\epsilon)$) indicated that the frequency of the zone center optical longitudinal phonon of pure E_1 symmetry is $\omega_{LE} = 916 \text{ cm}^{-1}$ and that of the zone center longitudinal optical phonon of A_1 symmetry is $\omega_{LA} = 890 \text{ cm}^{-1}$. The static and high frequency dielectric constants along the c-axis and in the basal isotropic plane are deduced by extrapolating the real parts of the obtained dielectric functions to zero and infinity. Then, upon using the derived expressions for the orientation-dependent harmonic and anharmonicity parameters, the generalized Lydanne-Sachs-Teller equation (Eq. 4.2), Loudon equations (Eqs. 4.5 and 4.6), and the expression of the angle-dependent dielectric function (Eq. 4.7), we find that the harmonic force constants (α), (β), (σ) and the angle between the incident electric field and the plane of incidence (φ) are the only unknowns in the expression of the total reflectivity (Eq. 4.10). Moreover, the number of unknowns

in the expression of the total reflectivity can be reduced further if we realize that the force constants β and σ can be expressed in terms of using Eqs. 4.14 and 4.17. Thus, the only independent adjustable parameters in the reflectivity model are α and φ . It is worth noting that the model adjustable parameters α and φ are not entangled. The angle φ affects the positions of the main features in the reflectivity spectrum (maxima and minima), while the force constant α affects their strengths.

	{0001}	{10 – 14}	{10 – 13}	{10 – 12}	{10 – 10}
$\varphi(^{\circ})$	0.90	28.44	31.68	35.10	39.78
$\alpha(N/m)$	5.193	5.382	5.364	5.337	5.283
$a(A^{\circ})$	3.11	0.68	0.83	1.04	1.39
$\Gamma_E(cm^{-1})$	5.3648	7.3712	7.1838	6.9929	6.3704
$\Gamma_{\perp}(cm^{-1})$	5.8983	7.3773	7.1853	7.0286	14.2439
$\Gamma_{\parallel}(cm^{-1})$	11.9172	16.1211	15.8142	15.1395	6.3704

Table 4.2: Model parameters. Only α and φ were used as independent adjustable parameters to fit the reflectivity model to the measured reflectivity spectra.

The best fitting reflectivity curves to the measured reflectivity spectra are shown in Figure 4.1 using solid lines, and the values of α and φ obtained by fitting the model to the experimental data are given in Table 4.2. We also provide in Table 4.2 the interplanar spacing in each crystallographic direction. It can be clearly noticed that as the planes come closer to one another, the force constant α increases.

From the knowledge of the dependence of the force constants on the crystallographic direction and by using Eq. 4.22, we can evaluate the dependence of the zone center optical phonon damping parameter (or the rate at which the zone center optical phonon decays) on the crystallographic direction. The direction-dependent phonon damping parameters are presented in Table 4.2. Comparing the values of the phonon damping parameters, we notice that mixed symmetry

zone center optical phonons have higher rates of decay (shorter lifetimes) than zone center optical phonons of pure symmetry.

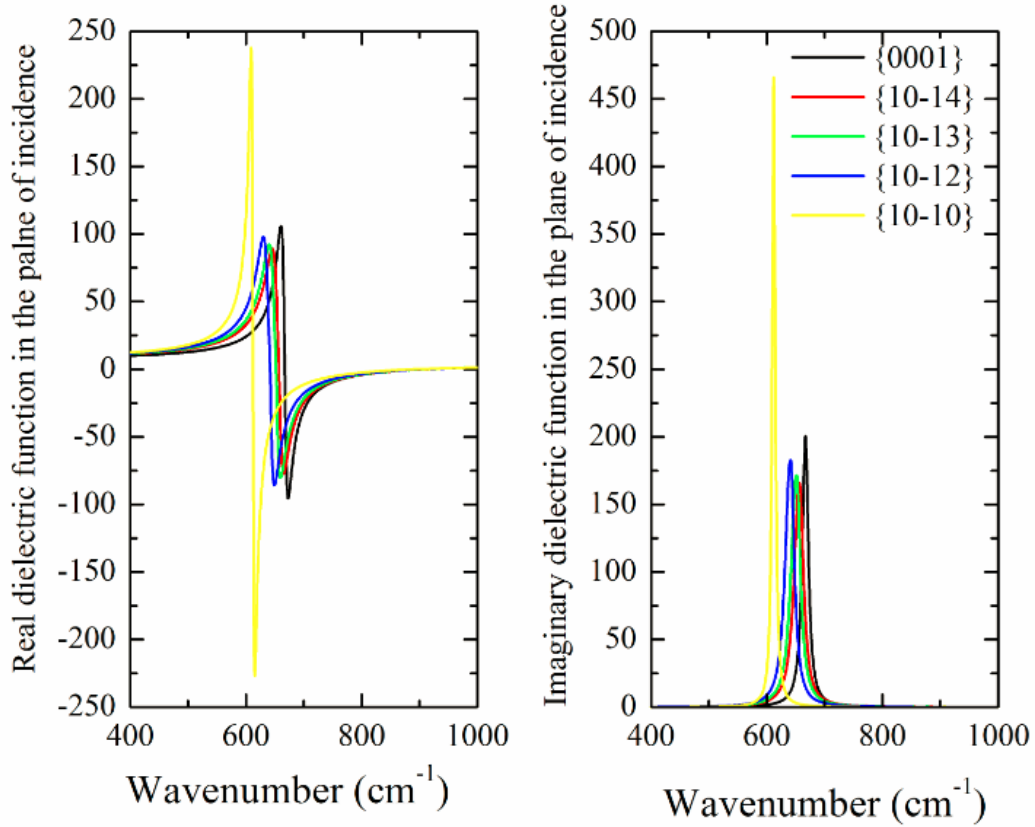


Figure 4.2: The real and imaginary parts of the normal incidence dielectric functions of the measured facets for a p-polarized light.

After having determined the force constants, all the harmonicity and anharmonicity parameters of the dielectric function for s -polarization $\epsilon_E(\omega)$ and the direction-dependent dielectric function for p -polarization $\epsilon(\omega, \theta)$ can be determined. Consequently, the calculation of $\epsilon_E(\omega)$ and $\epsilon(\omega, \theta)$ in every measured facet is made possible. Since the TM nature of SPhP forces it to be coupled to the p -polarized component of the electric field, the properties of SPhP modes are determined by only the dielectric function for TM polarization $\epsilon(\omega, \theta)$. In Figure 4.2, we show the normal incidence dielectric function of each of the measured

facets for TM polarization.

4.2.5 Dependence of SPhP on Surface Orientation

After solving Maxwells equations both inside and outside a semi-infinite crystalline material, and applying proper boundary conditions, one can write the dispersion relations of SPhP wave in the form [56]

$$(ck_{\parallel})^2 = \frac{\epsilon(\omega, \theta)}{1 + \epsilon(\omega, \theta)}\omega^2, \quad (4.23)$$

where ω and k_{\parallel} are the angular frequency and wavevector (oriented parallel to the surface) of SPhP wave and c is the speed of light in vacuum. The component of the wavevector of the incident radiation parallel to the surface of the sample is the one that interacts with surface modes and is given by [5]

$$k_{\parallel} = \frac{\omega}{c} \sin \theta. \quad (4.24)$$

On the other hand, the response of the material $\epsilon(\omega, \theta)$ is a function of the angle of incidence (θ), which makes the excitation of SPhP modes angle dependent. Equating the wavevectors in Eqs. 4.23 and 4.24, we can find the angle of incidence required to excite a SPhP mode of angular frequency ω . Thus, for each frequency ω , a specific angle θ should be invoked in the expression of $\epsilon(\omega, \theta)$ (Eq. 4.7). In order to evaluate the dispersion curves and lifetimes of SPhP on the measured facets, we consider a real wavevector k and a complex frequency $\omega(k) = \omega'(k) + i\omega''(k)$ and solve Eq. 4.23 numerically. The functions $\omega'(k)$ determine the dispersions of the SPhP modes, while the inverse of the function $\omega''(k)$

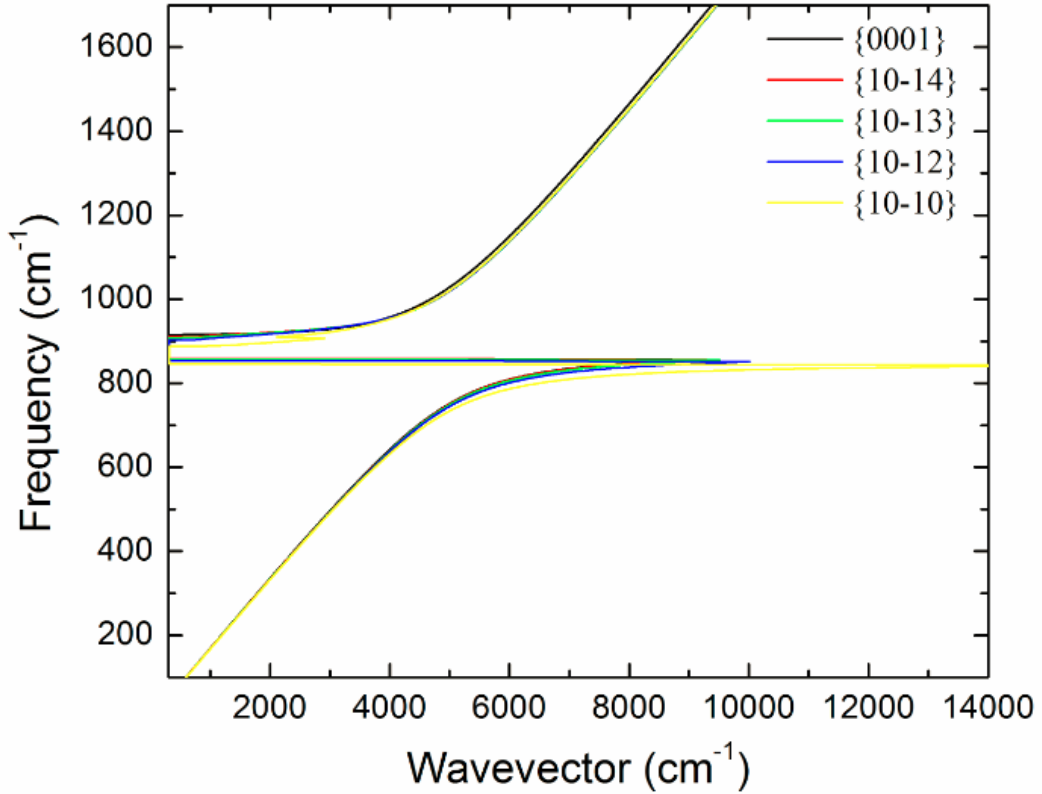


Figure 4.3: The dispersions of the SPhP waves on the measured facets.

determine their lifetimes. The numerically derived SPhP dispersions are plotted in Figure 4.3. It is clear that the facet orientation has a weak effect on the dispersion of SPhP. The slopes of the dispersion curves are almost unaffected by the facet orientation, which demonstrates that the SPhP modes travel with the same group velocity on all the measured facets. Nevertheless, since ω_T and ω_L bound the spectral region where the SPhP modes exist (the Reststrahlen band), and since both ω_T and ω_L depend on the facet orientation, AlN facets of different orientations support SPhP modes of different energies. Hence, the differently oriented facets of the self-nucleated AlN single crystal investigated in the work allow tuning the frequencies of SPhP modes.

The numerically derived SPhP lifetimes are plotted in Figure 4.4. As can be

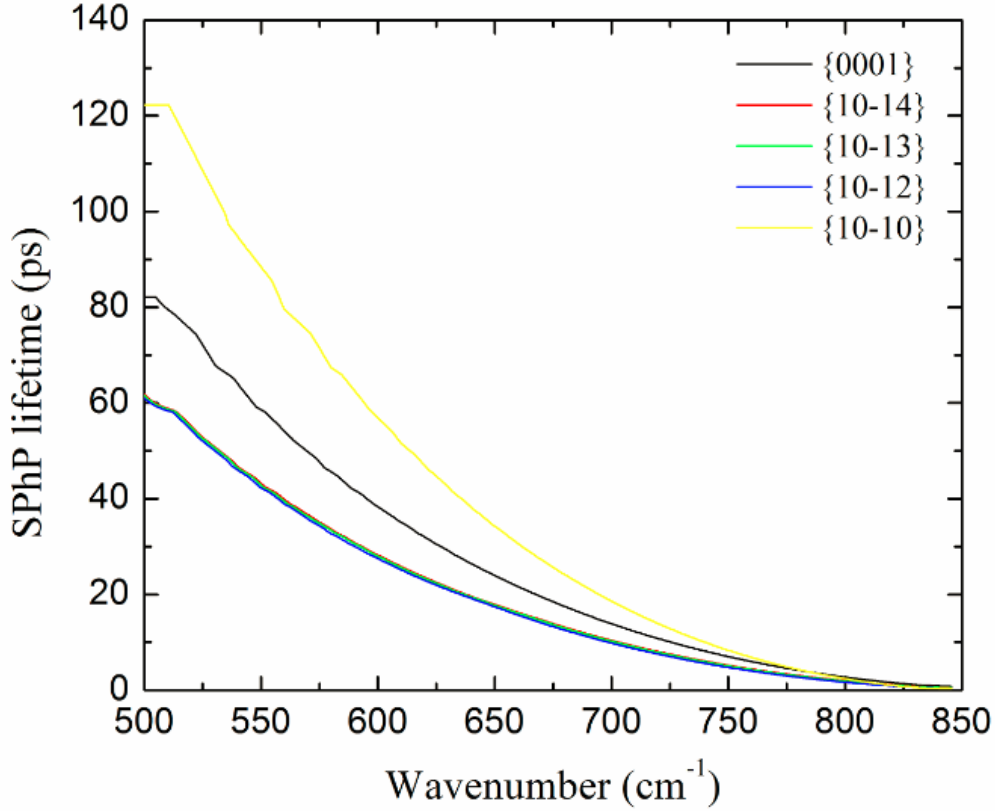


Figure 4.4: The lifetimes of the SPhP modes on the measured facets

noticed, the facet orientation plays a major role in determining the lifetime of the SPhP modes. It is shown above that zone center optical phonons of pure A_1 character have the highest lifetimes, whereas phonons of mixed symmetry experience shorter lifetimes (see Table 4.2). The SPhP modes follow the same trend of the zone center optical phonons. The SPhP modes propagating on the facets belonging to the $\{10-10\}$ crystallographic class exhibit the longest lifetime. Comparing the lifetimes of SPhP modes in Figure 4.4, we can see that SPhP modes resulting from coupling of incident electric field with pure A_1 symmetry phonons experience the longest lifetimes (50 ps in the region of existence), whereas a 50 % drop in lifetime is observed for SPhP modes resulting from coupling of incident electric field with mixed symmetry phonons. Thus, changing the facet

orientation leads to a change in the symmetry of optical phonon (pure E_1 , pure A_1 , or mixed) that couples to the incident electromagnetic field, which in turn affects the lifetime of the SPhP mode. In Figure 4.5, we sketch the frequencies

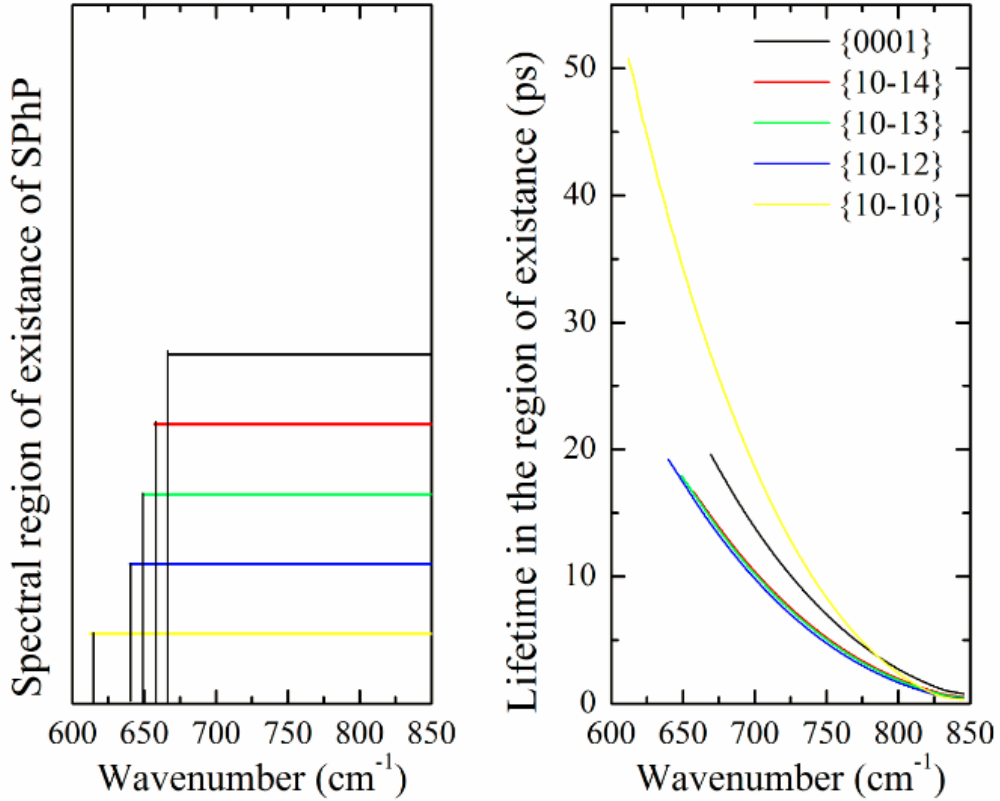


Figure 4.5: On the left: The spectral regions of existence of the SPhP modes on the measured facets. On the right: the lifetimes of the SPhP modes in their spectral regions of existence.

and lifetimes of the SPhP on each of the measured facets. It can be clearly seen that by changing the facet exposed to the incident electric field, one can tune the frequencies of the SPhP modes and modify their lifetimes. Consequently, the self-nucleated single crystal investigated in this work offers the opportunity of developing tunable near-field infrared sources.

4.3 Conclusion

A self-nucleated wurtzite AlN single crystal was grown with minimal contact with the crucible wall or other crystals. It was found that the grown crystal exhibits natural growth habit of AlN with many well-developed facets. X-ray texture measurements demonstrated that the developed facets belong to the $\{10-10\}$ $\{10-12\}$ $\{10-13\}$ $\{10-14\}$ and $\{0001\}$ crystallographic classes. Unpolarized reflectivity measurements were carried out on the developed facets. The measured spectra were analyzed using a general model for unpolarized reflectivity involving the dependence of the surface orientation on the harmonicity and anharmonicity of the excited zone center optical phonon. The harmonicity and anharmonicity parameters of the model obtained by fitting the model to the measured spectra were used to determine the dielectric function for s -polarization and the angle-dependent dielectric function for p -polarization of the measured facets. The dispersions of SPhP and their lifetimes on the measured facets were computed using the derived dielectric functions. It was found that both the lifetime of the SPhP modes and the spectral region in which the SPhP modes exist markedly depend on the facet orientation. This makes self-nucleated AlN crystals suitable for the development of near-field infrared sources tunable over a wide spectral range.

Chapter 5

Surface Phonon Polaritons on cylindrical structures

We have seen thus far two different methods for tuning the SPhP modes. Changing the surface symmetry of a given sample had its effect on the lifetime of optical phonons. It was also used as a mechanism to shift the resonance frequencies at which transverse and longitudinal optical phonons were excited. Consequently, the lifetime and the region of existence of SPhP modes were shown to be tunable. Another method was to change the carrier concentration inside a sample, and study its effect on the SPhP modes. It was found that this was a proper technique for tuning the lifetime and the temporal coherence of the SPhP waves. Both of these methods were investigated on flat surfaces. In order to have a full understanding about the behavior of SPhP waves and the tools required for manipulating them, we now proceed to study the effect of the shape of the sample on the properties of the surface waves.

Let us consider SPhP waves propagating along a circular cylindrical structure as shown in Figure 5.1. There are three distinct regions, each described by a

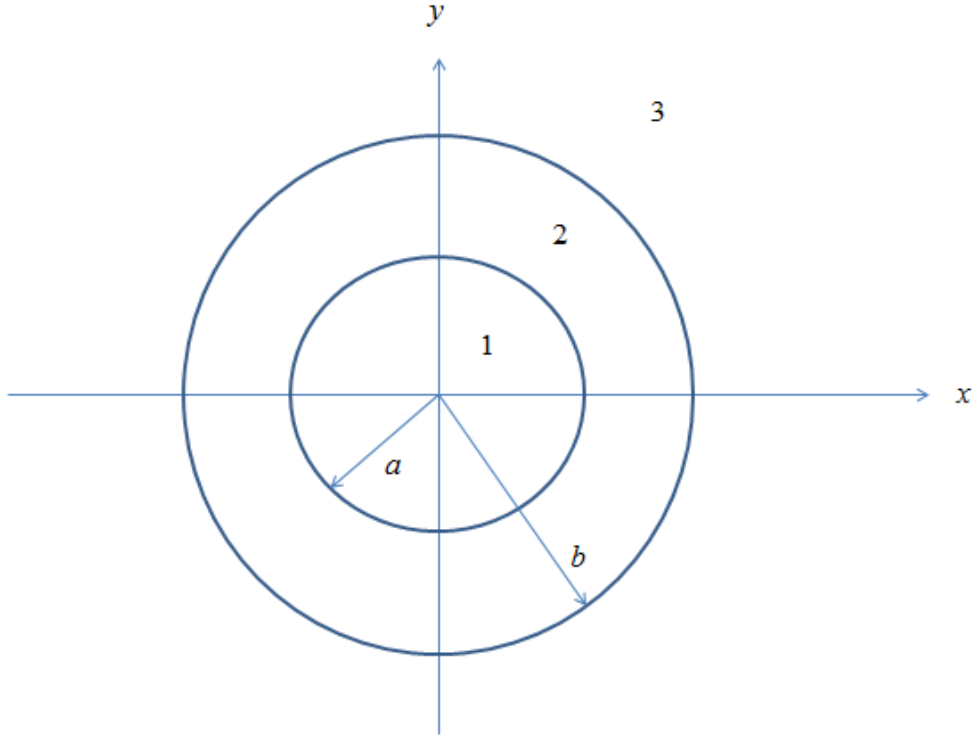


Figure 5.1: Geometry of the cylindrical structure.

certain dielectric function. The propagation direction is taken along z (out of the page), with $r = a$ and $r = b$ being the radii of the inner and outer circles respectively. Since the symmetry of the problem is different than that of the flat surface, the solutions to Maxwells equations will be modified. The field components of the TM SPhP waves tangential to the cylindrical surfaces are the following: [4]

Region 1:

$$E_z^{(1)} = A_1 I_0(p_1 r), \quad (5.1)$$

$$H_\theta^{(1)} = \frac{i\omega\epsilon_1}{p_1} A_1 I_0'(p_1 r), \quad (5.2)$$

where

$$p_1^2 = q^2 - k_1^2, \quad (5.3)$$

$$k_1^2 = \omega^2 \mu_0 \epsilon_1. \quad (5.4)$$

Similar equations are found in regions 2 and 3.

Region 2:

$$E_z^{(2)} = [A_2 I_0(p_2 r) + A_3 K_0(p_3 r)], \quad (5.5)$$

$$H_\theta^{(2)} = \frac{i\omega\epsilon_2}{p_2} [A_2 I_0'(p_2 r) + A_3 K_0'(p_3 r)], \quad (5.6)$$

$$p_2^2 = q^2 - k_2^2, \quad (5.7)$$

$$k_2^2 = \omega^2 \mu_0 \epsilon_2. \quad (5.8)$$

Region 3:

$$E_z^{(3)} = A_4 K_0(p_3 r), \quad (5.9)$$

$$H_\theta^{(2)} = \frac{i\omega\epsilon_2}{p_2} A_4 K_0'(p_3 r), \quad (5.10)$$

$$p_3^2 = q^2 - k_3^2, \quad (5.11)$$

$$k_3^2 = \omega^2 \mu_0 \epsilon_3. \quad (5.12)$$

Here A_1 , A_2 , A_3 and A_4 are the amplitudes of the propagating waves in different regions. I_0 and K_0 are the modified Bessel functions of order zero, and the prime on these functions represent the derivative of the functions with respect to their arguments.

Matching the tangential electric and magnetic fields at the boundaries $r = a$

and $r = b$ we find

$$A_1 I_0(p_1 a) = A_2 I_0(p_2 a) + A_3 K_0(p_2 a), \quad (5.13)$$

$$\frac{i\omega\epsilon_1}{p_1} A_1 I'_0(p_1 a) = \frac{i\omega\epsilon_2}{p_2} [A_2 I'_0(p_2 a) + A_3 K'_0(p_2 a)], \quad (5.14)$$

$$A_2 I_0(p_2 b) + A_3 K_0(p_2 b) = A_4 K_0(p_3 b), \quad (5.15)$$

$$\frac{i\omega\epsilon_2}{p_2} [A_2 I'_0(p_2 b) + A_3 K'_0(p_2 b)] = \frac{i\omega\epsilon_3}{p_3} A_4 K'_0(p_3 b), \quad (5.16)$$

We are interested in investigating the properties of SPhP modes on a polar material in the form of a nanowire surrounded by air. Therefore we take the limit of $b \rightarrow \infty$ that will describe the region containing air. Region 1 on the other hand will represent the nanowire of radius a with a complex dielectric function ϵ_1 . Solving equations (5.13) to (5.16) by taking the limits of the Bessel functions as $b \rightarrow \infty$ we can find the dispersion relation of the SPhP modes propagating at the surface of a cylindrical polar material.

$$\frac{K_0(p_2 a)}{I_0(p_1 a)} - \frac{\epsilon_2 p_1}{\epsilon_1 p_2} \frac{K'_0(p_2 a)}{I'_0(p_1 a)} = 0 \quad (5.17)$$

We notice that in the limit of very large a , the problem reduces to the flat surface situation. Taking the limit $a \rightarrow \infty$ in equation (5.17) the dispersion relation of SPhP waves traveling on a flat surface can be obtained

$$1 + \frac{\epsilon_2 p_1}{\epsilon_1 p_2} = 0. \quad (5.18)$$

This is the same dispersion relation found in chapter 1.

In order to determine the dispersion relation of the nanowire, we consider a real frequency ω and a complex wavevector $q = q' + iq''$ and solve equation (5.17) numerically. As explained earlier $\omega(q')$ will describe the dispersion relation

and the inverse of the function $\omega(q'')$ will give the frequency dependent mean-propagation-length of the SPhP modes. The complex dielectric function of the nanowire can be described by Drudes model introduced in chapter 4. The material is considered to be SiC with a radius of $50nm$. At radii smaller than $50nm$, the volume of the nanowire becomes so small, that surface effects become significant. Consequently, the Drude model describing the behavior of phonons in the bulk of the material loses its accuracy. A larger value for the radius was not considered simply because the objective is to observe a significant change in the properties of surface waves when assuming a cylindrical structure. As we have seen earlier the nanowire problem reduces to the basic flat surface situation for large radii.

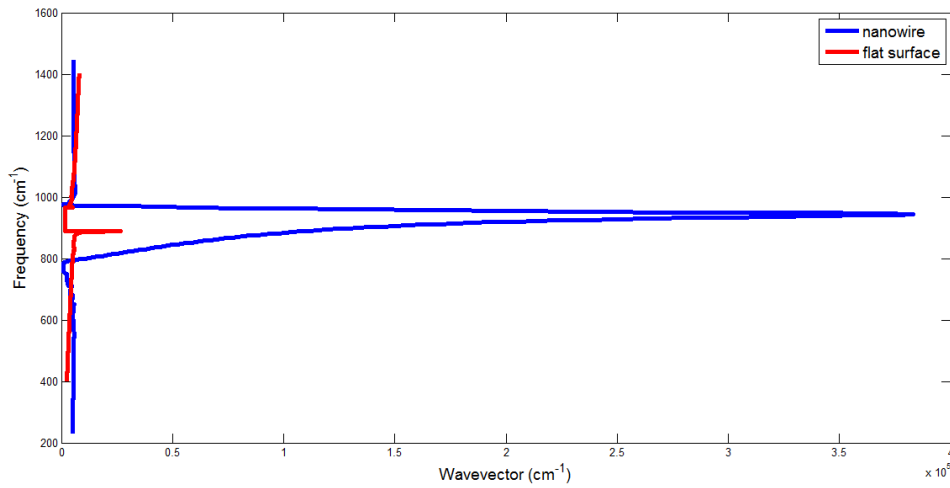


Figure 5.2: Comparing the dispersion relation of SPhP modes supported by SiC samples of different shapes. Blue color is used to represent the nanowire and red curve is used to represent the flat surface

Comparing the dispersion relation of the SiC nanowire (Figure 5.2) to that of the lowest doped SiC sample found in chapter 3, we notice that the nanowire curve extends to much larger values of wavevector q . In other words, changing the shape of a sample results in increasing the number of SPhP modes supported by the material. Consequently, when coupled to a periodic structure such as a

grating, cylindrical structures will emit more SPhP modes in more directions as compared to that emitted by parallelepiped- like structures.

Chapter 6

Conclusion

In the present thesis work, different methods for tuning the surface phonon polariton modes are investigated. These waves are the primary contributors to energy transport in sub-diffraction limits known as the near field. As is the case for many systems, unanticipated behaviors emerge in low dimensions. Unlike the conventional description of radiation presented by Planck, the near-field radiation maintains a very high energy density, concentrated in a narrow range of frequencies. In other words, SPhP modes show a monochromatic and a coherent behavior to some extent. This has attracted wide scientific interest in the past couple of decades and initiated a new area of active research in nanophotonics. Many SPhP-based applications have been suggested over the years ranging from the development of coherent infrared light-emitting thermal nano-sources to the treatment of various chronic diseases. Thus the ability to tune and manipulate the properties of SPhP modes has proven itself to be crucial for the advancement of useful technologies.

In chapter 1 a general introduction to the principles of SPhP modes is provided. Surface phonon polaritons result from the coupling between electromag-

netic modes (photons) and lattice vibrational modes (optical phonons) at the surface of polar materials. In most materials, a photon-phonon interaction is observed in the THz regime. Thus, SPhP modes are infrared electromagnetic modes localized at the surface of dielectric materials. The experimental detection of these waves is not a trivial task, since they acquire an evanescent character as they move away from the surface. But fortunately, practical techniques such as ATR and SNOM have been developed over the years, enabling the experimental detection of the SPhP modes.

The measurement and analysis techniques used for investigating the properties of SPhP modes are covered in chapter 2. SPhP modes are a form of light-matter interaction. Thus an accurate knowledge of the complex dielectric function describing the response of the material to an incident radiation is a key factor in understanding the behavior of SPhP waves. It is shown in this chapter that the response function of a given material can be obtained from a rigorous analysis of reflectivity measurements using the Kramers- Kronig (KK) conversion technique. The experimental setup used is a Fourier Transform Infrared (FTIR) spectroscopy whose main component is an interferometer based on the original design by Michelson.

In chapter 3 the properties of surface polariton modes are investigated as a function of carrier concentration in 4H- SiC crystals. P- polarized FTIR reflectivity measurements are performed on three different 4H- SiC samples having different carrier concentrations. The response function of each sample is determined by using the KK conversion technique. The KK conversion technique is a mathematical tool involving some assumptions that cannot be fully satisfied experimentally. Thus the results obtained from the KK conversion are prone to minor inaccuracies which are corrected on the basis of Fresnel equations of reflectivity.

The lifetime and mean-propagation-length of the coupled plasmon-phonon-polariton (PPhP) modes are deduced. A strong decay in lifetime and mean-propagation-length is observed as the carrier concentration is increased. However it is shown that the temporal coherence of the coupled plasmon-phonon-polariton mode is enhanced as a function of carrier concentration. Thus varying the carrier concentration can be used as a mechanism for developing coherent infrared light-emitting thermal nanosources.

The dependence of SPhP properties as a function of surface symmetry direction is studied in chapter 4. The sample under consideration is a self-nucleated wurtzite AlN crystal. Unpolarized FTIR reflectivity measurements are performed on the $\{10-10\}$ $\{10-12\}$ $\{10-13\}$ $\{10-14\}$ and $\{0001\}$ facets. Due to the anisotropy of the wurtzite structure, the response function of each high symmetry direction is different, consequently different reflectivity spectra are observed for each facet. Taking into account the angular dependence of the complex dielectric function, a reflectivity model is developed, explaining the different spectra observed experimentally. Upon fitting the experimental data with the theoretical model, the response function for each high symmetry direction is deduced and the SPhP properties are calculated. It is demonstrated that both the lifetime and region of existence of SPhP waves are a function of surface symmetry direction. Therefore changing the surface symmetry of a material can be used as an efficient technique to control the frequencies at which SPhP waves are excited. This provides the means to accurately tune the emission of thermal nanosources.

Finally, the behavior of SPhP modes is investigated in chapter 5 as a function of the shape of the material. The previous two mechanisms were studied on flat surfaces. In this chapter we derive the dispersion relation of SPhP waves for cylindrical structures. Since the symmetry of the problem is different than

that of flat surfaces, the SPhP characteristics change significantly. It has been shown that cylindrical structures have the capacity to support a much higher number of SPhP modes as compared to flat surfaces. In fact, in a given material SPhP modes can be added or eliminated by simply changing the geometry of the sample.

Thus, we investigated three different methods for tuning the properties of SPhP modes. Each method is proven to be efficient for a particular task. Varying the carrier concentration is used as a tool for enhancing the temporal coherence of SPhP waves. Changing the surface symmetry of a sample provides the means for tuning the frequencies at which SPhP waves are excited. While changing the shape of the sample is used to control the number of SPhP modes supported by the sample. We believe that the outcomes of this work may open new horizons in the field of nanophotonics where the tuning of SPhP modes will stand as the basis for the development of useful technologies.

Appendix A

Fresnel Equations for Reflectivity

The Fresnel equations derived by Augustin Jean- Fresnel describe the behavior of light propagating between media of different refractive indices. When an incident electromagnetic field strikes the interface between two different media, both reflection and transmission occur (Figure A.1). As can be seen in Figure A.1, more than one transmitted or reflected wave is present in each medium. To simplify the problem, a technique known as the transfer matrix method is used to combine all the waves in each medium (both forward and backward) into a single wave.[44] . In this approach the electric and magnetic fields at different points can be related by an interference matrix M (Figure A.2).

Considering a TM wave, the x - component of the electric field and the y - component of the magnetic field can be written as a function of the distance z :

$$E_x(z) = \cos(\theta_2)E^+ e^{i\varphi(z)} + \cos(\theta_2)E^- e^{-i\varphi(z)} \quad (\text{A.1})$$

and

$$H_y(z) = \frac{n_2}{\mu c} \left[E^+ e^{i\varphi(z)} - E^- e^{-i\varphi(z)} \right] \quad (\text{A.2})$$

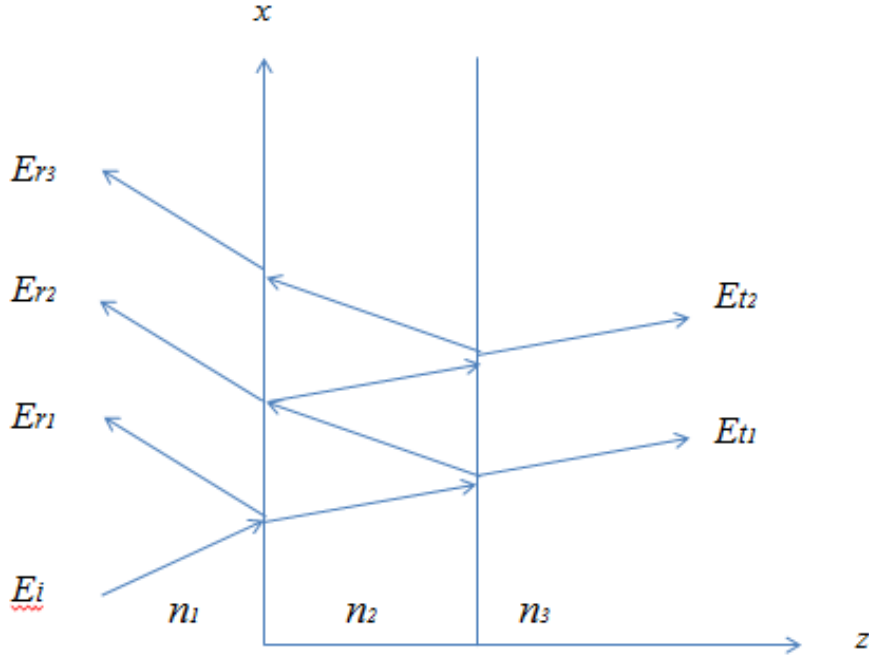


Figure A.1: Reflection and transmission occur when light moves from a medium of a given refractive index to another.

where E^+ and E^- are the amplitudes of the forward and backward propagating electric fields, θ_2 is the angle between the wavevector and the z - direction and

$$\varphi(z) = \frac{\omega n_2 z \cos \theta_2}{c}. \quad (\text{A.3})$$

In the above equations the terms $e^{-i\omega t}$ and $e^{-q_x x}$ are dropped since they will eventually get cancelled when boundary conditions are applied.

The objective is to relate the electric and magnetic fields at a random location z to the fields at the origin $z = 0$. Substituting $z = 0$ in equations (A.1) and (A.2) eliminating the amplitudes E^+ and E^- , the fields at a location z are found

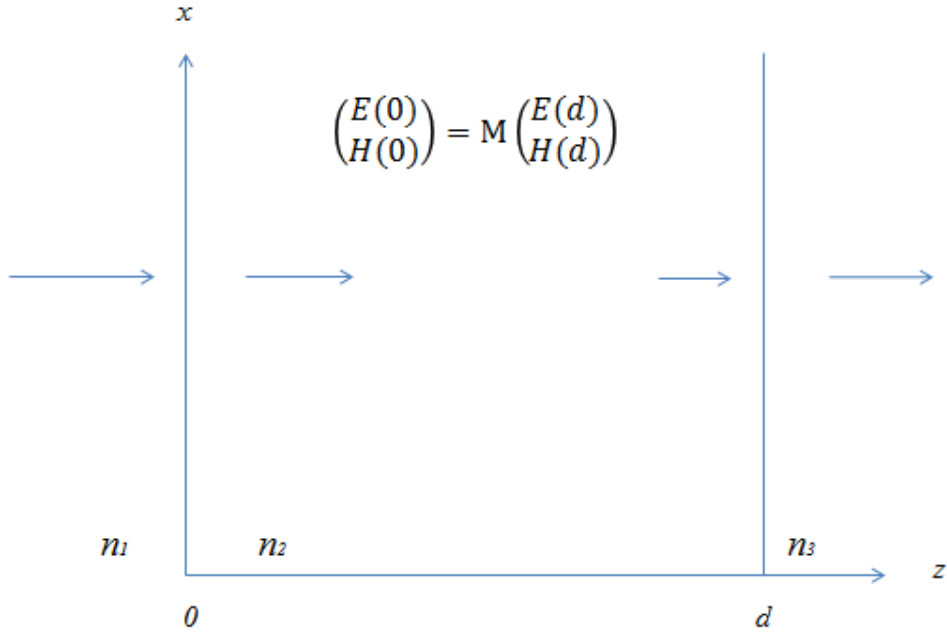


Figure A.2: The transfer matrix method: All reflected and transmitted waves in each medium are presented by a single wave. The amplitudes of the electric and magnetic fields at different points are related by an interference matrix M .

to be

$$E_x(z) = E_x(0) \cos \varphi(z) + ip_2 H_y(0) \sin \varphi(z) \quad (\text{A.4})$$

and

$$E_y(z) = \frac{i}{p_2} E_x(0) \sin \varphi(z) + H_y(0) \cos \varphi(z) \quad (\text{A.5})$$

where $p_2 = [\cos \theta_2 / n_2 / \mu c]$ is the surface impedance for a TM wave. The above equations can be represented in a matrix form

$$\begin{bmatrix} E_x(z) \\ H_y(z) \end{bmatrix} = \begin{bmatrix} \cos \varphi(z) & ip_2 \sin \varphi(z) \\ \frac{i}{p_2} \sin \varphi(z) & \cos \varphi(z) \end{bmatrix} \begin{bmatrix} E_x(0) \\ H_y(0) \end{bmatrix}. \quad (\text{A.6})$$

Taking $z = d$ the fields at the two interfaces can be related

$$\begin{bmatrix} E_x(0) \\ H_y(0) \end{bmatrix} = \begin{bmatrix} \cos \varphi_2 & -ip_2 \sin \varphi_2 \\ -\frac{i}{p_2} \sin \varphi_2 & \cos \varphi_2 \end{bmatrix} \begin{bmatrix} E_x(d) \\ H_y(d) \end{bmatrix} = M \begin{bmatrix} E_x(d) \\ H_y(d) \end{bmatrix} \quad (\text{A.7})$$

where $\varphi_2 = \varphi(d)$ and M is the interference matrix introduced earlier.

Equation (A.7) relates the electric and magnetic fields at the two boundaries of the film. To find the reflectivity, the fields inside the sample described by the refractive index n_2 , should be related to the fields outside the sample (in regions described by n_1 and n_3). The continuity of the tangential fields at a given boundary implies that the electric and magnetic fields at the origin will be related to the incident and reflected waves in the region described by n_1 (Figure A.1). Combining all the reflected fields into a single reflected field E_r , the boundary condition can be written in the following way

$$E_x(0) = E_i \cos \theta_i + E_r \cos \theta_r = E_{ix} + E_{rx} \quad (\text{A.8})$$

and

$$H_y(0) = \frac{n_1}{\mu c} (E_i - E_r) = \frac{1}{p_1} (E_{ix} - E_{rx}) \quad (\text{A.9})$$

where $p_1 = [\cos \theta_i / n_1 / \mu c]$. Combining all the transmitted waves into a single wave E_t the boundary condition at $z = d$ can be written as

$$E_x(d) = E_t \cos \theta_t = E_{tx} \quad (\text{A.10})$$

and

$$H_y(d) = \frac{n_3}{\mu c} E_t = \frac{1}{p_3} E_{tx} \quad (\text{A.11})$$

where $p_3 = [\cos \theta_t / n_3 / \mu c]$. Expressing equations (A.8) to (A.11) in a matrix form and substituting them in equation (A.7), the incident, reflected and transmitted waves can be related by

$$\begin{bmatrix} 1 & 1 \\ \frac{1}{p_1} & -\frac{1}{p_1} \end{bmatrix} \begin{bmatrix} E_{ix} \\ E_{rx} \end{bmatrix} = \begin{bmatrix} m_{11} & m_{12} \\ m_{21} & m_{22} \end{bmatrix} \begin{bmatrix} 1 \\ \frac{1}{p_3} \end{bmatrix} E_{tx} \quad (\text{A.12})$$

where m_{ij} are the elements of the interference matrix M . Inverting the matrix of the left hand side in equation (A.12) and multiplying it with the two matrices on the right hand side gives

$$\begin{bmatrix} E_{ix} \\ E_{rx} \end{bmatrix} = \frac{1}{2} \begin{bmatrix} (m_{11} + \frac{1}{p_3} m_{12}) + (m_{21} + \frac{1}{p_3} m_{22}) p_1 \\ (m_{11} + \frac{1}{p_3} m_{12}) - (m_{21} + \frac{1}{p_3} m_{22}) p_1 \end{bmatrix} E_{tx} \quad (\text{A.13})$$

From equation (A.13) the Fresnel coefficient for reflectivity can be deduced

$$r = \frac{E_r}{E_i} = \frac{E_{rx}}{E_{ix}} = \frac{(m_{11} + \frac{1}{p_3} m_{12}) + (m_{21} + \frac{1}{p_3} m_{22}) p_1}{(m_{11} + \frac{1}{p_3} m_{12}) - (m_{21} + \frac{1}{p_3} m_{22}) p_1}. \quad (\text{A.14})$$

Having an expression for the Fresnel coefficient of reflection, the reflectivity spectrum can be calculated.

Bibliography

- [1] S. Volz, *Microscale and nanoscale heat transfer*. Springer, 2007.
- [2] G. P. Srivastava, *The physics of phonons*. CRC press, 1990.
- [3] S. Perkowitz, *Optical characterization of semiconductors: infrared, Raman, and photoluminescence spectroscopy*, vol. 14. Elsevier, 2012.
- [4] C. Yeh and F. I. Shimabukuro, *The essence of dielectric waveguides*. Springer, 2008.
- [5] J. Le Gall, M. Olivier, and J.-J. Greffet, “Experimental and theoretical study of reflection and coherent thermal emission by a sic grating supporting a surface-phonon polariton,” *Physical Review B*, vol. 55, no. 15, p. 10105, 1997.
- [6] S. Mornet, S. Vasseur, F. Grasset, and E. Duguet, “Magnetic nanoparticle design for medical diagnosis and therapy,” *Journal of Materials Chemistry*, vol. 14, no. 14, pp. 2161–2175, 2004.
- [7] R. Hergt, S. Dutz, R. Müller, and M. Zeisberger, “Magnetic particle hyperthermia: nanoparticle magnetism and materials development for cancer therapy,” *Journal of Physics: Condensed Matter*, vol. 18, no. 38, p. S2919, 2006.

- [8] D. Pissuwan, S. M. Valenzuela, and M. B. Cortie, “Therapeutic possibilities of plasmonically heated gold nanoparticles,” *TRENDS in Biotechnology*, vol. 24, no. 2, pp. 62–67, 2006.
- [9] X. Huang, P. K. Jain, I. H. El-Sayed, and M. A. El-Sayed, “Plasmonic photothermal therapy (pptt) using gold nanoparticles,” *Lasers in medical science*, vol. 23, no. 3, p. 217, 2008.
- [10] P. N. Prasad, *Nanophotonics*. John Wiley & Sons, 2004.
- [11] U. Schellenberger, M. Abraham, and U. Trutschel, “Free surface plasmon propagation: A method for metal-electrolyte interface studies in the infrared spectral region,” *Surface science*, vol. 192, no. 2-3, pp. 555–562, 1987.
- [12] K. Kliewer and R. Fuchs, “Theory of dynamical properties of dielectric surfaces,” *Adv. Chem. Phys*, vol. 27, no. 355-541, p. 109, 1974.
- [13] Y. De Wilde, F. Formanek, R. Carminati, B. Gralak, P.-A. Lemoine, K. Joulain, J.-P. Mulet, Y. Chen, and J.-J. Greffet, “Thermal radiation scanning tunnelling microscopy,” *Nature*, vol. 444, no. 7120, pp. 740–743, 2006.
- [14] A. Huber, N. Ocelic, D. Kazantsev, and R. Hillenbrand, “Near-field imaging of mid-infrared surface phonon polariton propagation,” *Applied physics letters*, vol. 87, no. 8, p. 081103, 2005.
- [15] A. Huber, B. Deutsch, L. Novotny, and R. Hillenbrand, “Focusing of surface phonon polaritons,” *Applied Physics Letters*, vol. 92, no. 20, p. 203104, 2008.
- [16] F. Keilmann, R. Hillenbrand, A. Zayats, and D. Richard, *Near-field nanoscopy by elastic light scattering from a tip*. Artech House, 2009.

- [17] J. M. Hollas, *Modern spectroscopy*. John Wiley & Sons, 2004.
- [18] S. Slussarenko, A. Alberucci, C. P. Jisha, B. Piccirillo, E. Santamato, G. As-santo, and L. Marrucci, “Guiding light via geometric phases,” *Nature Photonics*, 2016.
- [19] J. M. Merlo, N. T. Nesbitt, Y. M. Calm, A. H. Rose, L. DiImperio, C. Yang, J. R. Naughton, M. J. Burns, K. Kempa, and M. J. Naughton, “Wireless communication system via nanoscale plasmonic antennas,” *Scientific reports*, vol. 6, 2016.
- [20] J. Fan, Z. Li, Z. Chen, and W. Wu, “Standing-wave resonances in plasmonic nanoumbrella cavities for color generation and colorimetric refractive index sensor,” *Applied Surface Science*, vol. 384, pp. 534–538, 2016.
- [21] J. D. Caldwell, A. Kretinin, Y. Chen, V. Giannini, M. M. Fogler, Y. Francescato, C. T. Ellis, J. G. Tischler, C. R. Woods, A. J. Giles, *et al.*, “Sub-diffractive, volume-confined polaritons in a natural hyperbolic material: hexagonal boron nitride,” *arXiv preprint arXiv:1404.0494*, 2014.
- [22] J. D. Caldwell, I. Vurgaftman, J. G. Tischler, O. J. Glembocki, J. C. Owrutsky, and T. L. Reinecke, “Atomic-scale photonic hybrids for mid-infrared and terahertz nanophotonics,” *Nature nanotechnology*, vol. 11, no. 1, pp. 9–15, 2016.
- [23] A. de Hoogh, A. Opheij, M. Wulf, N. Rotenberg, and L. Kuipers, “Harmonics generation by surface plasmon polaritons on single nanowires,” *ACS photonics*, vol. 3, no. 8, p. 1446, 2016.
- [24] F. Chiadini, V. Fiumara, A. Scaglione, and A. Lakhtakia, “Compound guided waves that mix characteristics of surface-plasmon-polariton, tamm,

- dyakonov–tamm, and uller–zenneck waves,” *JOSA B*, vol. 33, no. 6, pp. 1197–1206, 2016.
- [25] J. Dong, J. Wang, F. Ma, Y. Cheng, H. Zhang, and Z. Zhang, “Recent progresses in integrated nanoplasmonic devices based on propagating surface plasmon polaritons,” *Plasmonics*, vol. 10, no. 6, pp. 1841–1852, 2015.
- [26] J. D. Caldwell, L. Lindsay, V. Giannini, I. Vurgaftman, T. L. Reinecke, S. A. Maier, and O. J. Glembocki, “Low-loss, infrared and terahertz nanophotonics using surface phonon polaritons,” *Nanophotonics*, vol. 4, no. 1, pp. 44–68, 2015.
- [27] J. B. Khurgin and A. Boltasseva, “Reflecting upon the losses in plasmonics and metamaterials,” *MRS bulletin*, vol. 37, no. 08, pp. 768–779, 2012.
- [28] A. Boltasseva and H. A. Atwater, “Low-loss plasmonic metamaterials,” *Science*, vol. 331, no. 6015, pp. 290–291, 2011.
- [29] C. F. Bohren and D. R. Huffman, *Absorption and scattering of light by small particles*. John Wiley & Sons, 2008.
- [30] T. Shibata, T. Mori, and S. Kojima, “Low-frequency vibrational properties of crystalline and glassy indomethacin probed by terahertz time-domain spectroscopy and low-frequency raman scattering,” *Spectrochimica Acta Part A: Molecular and Biomolecular Spectroscopy*, vol. 150, pp. 207–211, 2015.
- [31] J. D. Caldwell, O. J. Glembocki, Y. Francescato, N. Sharac, V. Giannini, F. J. Bezares, J. P. Long, J. C. Owrutsky, I. Vurgaftman, J. G. Tischler, *et al.*, “Low-loss, extreme subdiffraction photon confinement via silicon carbide localized surface phonon polariton resonators,” *Nano letters*, vol. 13, no. 8, pp. 3690–3697, 2013.

- [32] J.-J. Greffet, R. Carminati, K. Joulain, J.-P. Mulet, S. Mainguy, and Y. Chen, “Coherent emission of light by thermal sources,” *Nature*, vol. 416, no. 6876, pp. 61–64, 2002.
- [33] F. Marquier, K. Joulain, J.-P. Mulet, R. Carminati, J.-J. Greffet, and Y. Chen, “Coherent spontaneous emission of light by thermal sources,” *Physical Review B*, vol. 69, no. 15, p. 155412, 2004.
- [34] R. Carminati and J.-J. Greffet, “Near-field effects in spatial coherence of thermal sources,” *Physical Review Letters*, vol. 82, no. 8, p. 1660, 1999.
- [35] A. V. Shchegrov, K. Joulain, R. Carminati, and J.-J. Greffet, “Near-field spectral effects due to electromagnetic surface excitations,” *Physical Review Letters*, vol. 85, no. 7, p. 1548, 2000.
- [36] J. A. Schuller, T. Taubner, and M. L. Brongersma, “Optical antenna thermal emitters,” *Nature Photonics*, vol. 3, no. 11, pp. 658–661, 2009.
- [37] H. Harima, S.-i. Nakashima, and T. Uemura, “Raman scattering from anisotropic lo-phonon–plasmon–coupled mode in n-type 4h– and 6h–sic,” *Journal of applied physics*, vol. 78, no. 3, pp. 1996–2005, 1995.
- [38] J. D. Caldwell, O. J. Glembocki, S. M. Prokes, E. R. Glaser, K. D. Hobart, D. M. Hansen, G. Chung, A. V. Bolotnikov, and T. S. Sudarshan, “Free carrier distribution profiling of 4h-sic substrates using a commercial optical scanner,” *Journal of applied physics*, vol. 101, no. 9, p. 093506, 2007.
- [39] M. Schubert, T. Hofmann, and J. Šik, “Long-wavelength interface modes in semiconductor layer structures,” *Physical Review B*, vol. 71, no. 3, p. 035324, 2005.

- [40] Y. Ishitani, “Theoretical and experimental study of the optical absorption at longitudinal phonon or phonon-plasmon coupling mode energy: An example of gan,” *Journal of Applied Physics*, vol. 112, no. 6, p. 063531, 2012.
- [41] D. Piliposyan, K. Ghazaryan, and G. Piliposian, “Magneto-electro-elastic polariton coupling in a periodic structure,” *Journal of Physics D: Applied Physics*, vol. 48, no. 17, p. 175501, 2015.
- [42] L. Ottaviani, M. Kazan, S. Biondo, F. Tuomisto, F. Milesi, J. Duchaine, F. Torregrosa, and O. Palais, “Study of defects generated by standard-and plasma-implantation of nitrogen atoms in 4h-sic epitaxial layers,” in *Materials Science Forum*, vol. 725, pp. 41–44, Trans Tech Publ, 2012.
- [43] N. Rahbany, M. Kazan, M. Tabbal, R. Tauk, J. Jabbour, J. Brault, B. Damilano, and J. Massies, “Measurement of the effect of plasmon gas oscillation on the dielectric properties of p-and n-doped alxga1-xn films using infrared spectroscopy,” *Journal of Applied Physics*, vol. 114, no. 5, p. 053505, 2013.
- [44] G. Chen, *Nanoscale energy transport and conversion: a parallel treatment of electrons, molecules, phonons, and photons*. Oxford University Press, 2005.
- [45] M. Kazan, “Crystal orientation by unpolarized infrared reflectivity application to aluminum nitride,” *Journal of Applied Physics*, vol. 102, no. 7, p. 073532, 2007.
- [46] S. Ushioda and J. McMullen, “Measurement of the frequency dependence of the phonon damping function by raman scattering from polaritons in gap,” *Solid State Communications*, vol. 11, no. 1, pp. 299–304, 1972.
- [47] M. Kazan, S. Pereira, M. Correia, and P. Masri, “Directional dependence of aln intrinsic complex dielectric function, optical phonon lifetimes, and de-

- cay channels measured by polarized infrared reflectivity,” *Journal of applied physics*, vol. 106, no. 2, p. 023523, 2009.
- [48] M. Kazan, C. Zgheib, E. Moussaed, and P. Masri, “Temperature dependence of raman-active modes in aln,” *Diamond and related materials*, vol. 15, no. 4, pp. 1169–1174, 2006.
- [49] V. Zemski, E. Ivchenko, D. Mirlin, and I. Reshina, “Dispersion of plasmon-phonon modes in semiconductors: Raman scattering and infrared spectra,” *Solid State Communications*, vol. 16, no. 2, pp. 221–225, 1975.
- [50] H. Yugami, S. Nakashima, A. Mitsuishi, A. Uemoto, M. Shigeta, K. Furukawa, A. Suzuki, and S. Nakajima, “Characterization of the free-carrier concentrations in doped β -sic crystals by raman scattering,” *Journal of applied physics*, vol. 61, no. 1, pp. 354–358, 1987.
- [51] T. Nakamura and T. Katoda, “Effects of optically excited carriers on raman spectra from inp,” *Journal of applied physics*, vol. 55, no. 8, pp. 3064–3067, 1984.
- [52] M. V. Klein, B. Ganguly, and P. J. Colwell, “Theoretical and experimental study of raman scattering from coupled lo-phonon-plasmon modes in silicon carbide,” *Physical Review B*, vol. 6, no. 6, p. 2380, 1972.
- [53] G. Irmer, V. Toporov, B. Bairamov, and J. Monecke, “Determination of the charge carrier concentration and mobility in n-gap by raman spectroscopy,” *physica status solidi (b)*, vol. 119, no. 2, pp. 595–603, 1983.
- [54] M. Kazan, B. Rufflé, C. Zgheib, and P. Masri, “Phonon dynamics in aln lattice contaminated by oxygen,” *Diamond and related materials*, vol. 15, no. 10, pp. 1525–1534, 2006.

- [55] R. Gammon and E. Palik, “Attenuated-total-reflection spectral linewidth: Analysis of surface-polariton dispersion relations and damping rates,” *JOSA*, vol. 64, no. 3, pp. 350–356, 1974.
- [56] N. Marschall and B. Fischer, “Dispersion of surface polaritons in gap,” *Physical Review Letters*, vol. 28, no. 13, p. 811, 1972.
- [57] A. Woessner, M. B. Lundeborg, Y. Gao, A. Principi, P. Alonso-González, M. Carrega, K. Watanabe, T. Taniguchi, G. Vignale, M. Polini, *et al.*, “Highly confined low-loss plasmons in graphene–boron nitride heterostructures,” *Nature materials*, vol. 14, no. 4, pp. 421–425, 2015.
- [58] R. Ritchie, “Plasma losses by fast electrons in thin films,” *Physical Review*, vol. 106, no. 5, p. 874, 1957.
- [59] M. Fleischmann, P. J. Hendra, and A. J. McQuillan, “Raman spectra of pyridine adsorbed at a silver electrode,” *Chemical Physics Letters*, vol. 26, no. 2, pp. 163–166, 1974.
- [60] D. L. Jeanmaire and R. P. Van Duyne, “Surface raman spectroelectrochemistry: Part i. heterocyclic, aromatic, and aliphatic amines adsorbed on the anodized silver electrode,” *Journal of Electroanalytical Chemistry and Interfacial Electrochemistry*, vol. 84, no. 1, pp. 1–20, 1977.
- [61] T. W. Ebbesen, H. J. Lezec, H. Ghaemi, T. Thio, and P. Wolff, “Extraordinary optical transmission through sub-wavelength hole arrays,” *Nature*, vol. 391, no. 6668, pp. 667–669, 1998.
- [62] N. Engheta and R. W. Ziolkowski, *Metamaterials: physics and engineering explorations*. John Wiley & Sons, 2006.

- [63] J. B. Khurgin and G. Sun, “In search of the elusive lossless metal,” *Applied Physics Letters*, vol. 96, no. 18, p. 181102, 2010.
- [64] J. B. Khurgin and G. Sun, “Scaling of losses with size and wavelength in nanoplasmonics and metamaterials,” *Applied Physics Letters*, vol. 99, no. 21, p. 211106, 2011.
- [65] P. R. West, S. Ishii, G. V. Naik, N. K. Emani, V. M. Shalaev, and A. Boltasheva, “Searching for better plasmonic materials,” *Laser & Photonics Reviews*, vol. 4, no. 6, pp. 795–808, 2010.
- [66] I. Chang, S. Mitra, J. Plendl, and L. Mansur, “Long-wavelength longitudinal phonons of multi-mode crystals,” *physica status solidi (b)*, vol. 28, no. 2, pp. 663–673, 1968.
- [67] N. W. Ashcroft, N. D. Mermin, and S. Rodriguez, “Solid state physics,” 1978.
- [68] C. F. Bohren and D. R. Huffman, “Angular dependence of scattering,” *Absorption and Scattering of Light by Small Particles*, pp. 381–428, 1998.
- [69] H. Karakachian and M. Kazan, “Dependence of surface plasmon-phonon-polariton in 4 h-sic on free carrier concentration,” *Journal of Applied Physics*, vol. 121, no. 9, p. 093103, 2017.
- [70] M. Kazan, S. Pereira, M. Correia, and P. Masri, “Contribution of the decay of optical phonons into acoustic phonons to the thermal conductivity of aln,” *Physical Review B*, vol. 77, no. 18, p. 180302, 2008.

- [71] M. Bickermann, B. Epelbaum, P. Heimann, Z. Herro, and A. Winnacker, “Orientation-dependent phonon observation in single-crystalline aluminum nitride,” *Applied Physics Letters*, vol. 86, no. 13, p. 131904, 2005.
- [72] P. Klemens, “Anharmonic decay of optical phonons,” *Physical Review*, vol. 148, no. 2, p. 845, 1966.
- [73] G. Weinreich, *Solids: elementary theory for advanced students*. J. Wiley, 1965.
- [74] B. Epelbaum, C. Seitz, A. Magerl, M. Bickermann, and A. Winnacker, “Natural growth habit of bulk aln crystals,” *Journal of Crystal Growth*, vol. 265, no. 3, pp. 577–581, 2004.
- [75] F. Wooten, *Optical properties of solids*. Academic press, 2013.
- [76] H. Grille, C. Schnittler, and F. Bechstedt, “Phonons in ternary group-iii nitride alloys,” *Physical Review B*, vol. 61, no. 9, p. 6091, 2000.
- [77] J. M. Hayes, M. Kuball, Y. Shi, and J. H. Edgar, “Temperature dependence of the phonons of bulk aln,” *Japanese Journal of Applied Physics*, vol. 39, no. 7B, p. L710, 2000.
- [78] P. Perlin, A. Polian, and T. Suski, “Raman-scattering studies of aluminum nitride at high pressure,” *Physical Review B*, vol. 47, no. 5, p. 2874, 1993.
- [79] R. Loudon, “The raman effect in crystals,” *Advances in Physics*, vol. 13, no. 52, pp. 423–482, 1964.
- [80] M. Kazan, G. Guisbiers, S. Pereira, M. Correia, P. Masri, A. Bruyant, S. Volz, and P. Royer, “Thermal conductivity of silicon bulk and nanowires:

Effects of isotopic composition, phonon confinement, and surface roughness,” *Journal of Applied Physics*, vol. 107, no. 8, p. 083503, 2010.

- [81] V. Y. Davydov, Y. E. Kitaev, I. Goncharuk, A. Smirnov, J. Graul, O. Semchinova, D. Uffmann, M. Smirnov, A. Mirgorodsky, and R. Evarestov, “Phonon dispersion and raman scattering in hexagonal gan and aln,” *Physical Review B*, vol. 58, no. 19, p. 12899, 1998.
- [82] Z. Alameh and M. Kazan, “Predictive calculation of the lattice thermal conductivity with temperature-dependent vibrational parameters,” *Journal of Applied Physics*, vol. 112, no. 12, p. 123506, 2012.
- [83] M. Kazan and S. Volz, “Calculation of the lattice thermal conductivity in granular crystals,” *Journal of Applied Physics*, vol. 115, no. 7, p. 073509, 2014.